TERRESTRIAL ARCHIVES OF METEORIC ^{10}BE

by

Adrian Singleton

A Thesis

Submitted to the Faculty of Purdue University

In Partial Fulfillment of the Requirements for the degree of

Master of Science

Department of Earth, Atmospheric, and Planetary Sciences

West Lafayette, Indiana

December 2021

THE PURDUE UNIVERSITY GRADUATE SCHOOL
STATEMENT OF COMMITTEE APPROVAL

Dr. Darryl Granger, Co-Chair

Department of Earth, Atmospheric, and Planetary Sciences, Purdue University

Dr. Nathaniel Lifton, Co-Chair

Department of Earth, Atmospheric, and Planetary Sciences, Purdue University

Dr. Joseph Graly

Department of Geography and Environmental Sciences, Northumbria University

Approved by:

Dr. Daniel Cziczo

Dedicated to Mom, Dad, Levy, family, and friends.

No work is ever done alone.

ACKNOWLEDGMENTS

This work would not have been possible without the knowledge, support, wisdom, and patience of Dr. Darryl Granger. We started this project uncertain of what we might find. We sought to measure Be isotopes in speleothems as a metric of chemical weathering in the landscape above caves. However, at that point, Be isotopes in speleothems had mostly been unexplored. We had to experiment and troubleshoot in nearly all phases of the research. I am appreciative of Darryl for his mentorship and guidance throughout the course of this work.

Dr. Nathaniel Lifton took me in as a student without a project. I appreciate the opportunity that he gave me. His wealth of knowledge about cosmogenic nuclide production was invaluable. This thesis was also shaped by Dr. Joseph Graly. Early in the course of my degree, I attended his semester-long seminar about meteoric ^{10}Be. My understanding of global ^{10}Be transport and deposition, as well as my knowledge of the many applications of meteoric ^{10}Be, were molded by these weekly discussions with Joseph, Dr. Kathy Licht, and fellow graduate student Eiríka Ösp Arnardóttir.

My exploration of cosmogenic nuclides began during my undergraduate under the mentorship of Dr. Amanda Schmidt at Oberlin College. She encouraged me to apply to graduate programs and was a key mentor during the early stages of my academic path. I also have appreciated the encouragement and support of fellow cosmogenic nuclide geochemists Allie Jo Koester Higginbotham, Sarah Sams, Lan Luo, Xianmei Huang, Jane Lund Andersen, and others.

The work on Be isotopes in terrestrial Mn-oxides that I present in the Appendix builds off the work of Dr. William Odom. I have benefitted from his guidance, support, and humor, especially on Wednesdays. Finally, I am appreciative of Angus Moore, whose intellectual input helped to shape this project. He has been an invaluable source of knowledge about Be isotopes and chemical weathering. Angus played a pivotal role in the derivation of the weathering rate equations that I present here.

TABLE OF CONTENTS

LIST OF TABLES

LIST OF FIGURES

ABSTRACT

The radionuclide ^{10}Be is produced in the atmosphere and is delivered to Earth's surface in meteoric rain and aerosols. The stable nuclide ^{9}Be is present in trace concentrations within rocks in Earth's crust and is released via chemical weathering. Together, these two isotopes have been employed to study a wide range of Earth processes. Here I explore new terrestrial archives of Be isotopes: cave speleothems and terrestrial Mn-oxides. Until this point, these archives have barely been studied. Only one published dataset of Be isotopes in cave speleothems exists (Lundblad, 2006), and to my knowledge, terrestrial manganese oxides are yet to be explored. However, since speleothems and Mn-oxides precipitate from groundwater, they have the potential to encode temporal variations in the $^{10}Be/^{9}Be$ ratio of water and colloids in the vadose zone.

I develop a framework for using the $^{10}Be/^{9}Be$ ratio in the dissolved phase and/or secondary weathering products as a metric of chemical weathering rate. I am motivated by several over-arching questions:

1) Which factor, or factors, is/are dominant in controlling Be isotopes in speleothems and terrestrial Mn-oxides?
2) Can Be isotopes in speleothems be used as a metric of weathering rate over time, particularly across glacial/interglacial cycles?
3) Can Be isotopes be used to date the formation of terrestrial Mn-oxides?

I measure Be-isotope concentrations in speleothems from Soreq Cave, Israel. By applying an equation that I derive in this thesis, I use the temporal variation in the speleothem $^{10}Be/^{9}Be$ ratio to calculate chemical weathering rates over the last 168 ka. Chemical weathering varies with independent proxies for temperature. The weathering-temperature relationship can be fit to an Arrhenius relationship, and the calculated activation energy (E_a) matches other field-based estimates for feldspar, an abundant mineral in the soil above the cave. In the Appendices I present additional results of Be-isotope measurements in a flowstone from Buffalo Cave in South Africa, as well as Mn-oxides from the Appalachians.

CHAPTER 1: INTRODUCTION

Beryllium isotopes have been explored in numerous archives, including ice cores, snow pits, marine cores, lake cores, marine ferro-manganese nodules, loess, travertine, and in reservoirs such as soils and river sediment. The concentrations of Be isotopes in these archives are impacted by numerous factors. These include changes in the fallout rate of ^{10}Be (impacted by changes in its production rate in the atmosphere, precipitation, and atmospheric circulation), and changes in environmental factors such as erosion, weathering, dust flux, and environmental biogeochemistry. I discuss these factors here in chapter 1.

In previously examined depositional settings, the dominant factor that controls Be concentrations and Be isotope ratios varies from archive to archive based on the length of time recorded, the temporal resolution, and the geologic and geographic settings. Long-term, low-resolution archives such as marine cores can reflect changes in meteoric ^{10}Be production in the atmosphere due to modulation of geomagnetic field strength, while loess profiles from China record changes in rainfall over millennia. Archives with annual resolution can record yearly and decadal changes in meteoric ^{10}Be production due to solar modulation of the cosmic ray flux. This can be seen in some ice cores and travertine. Sub-annual archives such as snow pits can record seasonal variations in the deposition of aerosols, which transport beryllium in the atmosphere.

Some archives such as ice cores and snow pits are direct records of ^{10}Be deposition in precipitation, with some additional modulation by dust flux. In contrast, the meteoric ^{10}Be (and ^{9}Be) concentrations in other archives such as marine/lacustrine cores, loess, soils, and travertine are further impacted by biogeochemical and sedimentary processes.

In this chapter I explore various archives and the factors that impact their Be isotopes, to help frame the various factors that may be important in archives precipitated from groundwater. In chapter 2 I present measurements of ^{10}Be/^{9}Be in speleothems from Soreq Cave in Israel.

Section 1: Beryllium isotope geochemistry

The element beryllium has three isotopes that have utility for Earth scientists. The only stable isotope is ^{9}Be, which accounts for nearly all beryllium on Earth. Additionally, two cosmogenic radionuclides of beryllium are produced by interactions between cosmic rays and terrestrial atoms and are present in detectable quantities. ^{10}Be has a half-life of 1.387×10^{6} years (Chmeleff et al., 2010; Korschinek et al., 2010), and ^{7}Be has a half-life of approximately 53.1 days (Norman et al., 2001). Both of these radionuclides are produced primarily in the atmosphere, but also *in situ* within mineral grains at Earth's surface. Although the applications of beryllium isotopes produced *in situ* within rocks are numerous, this thesis is concerned with the geochemistry and applications of meteoric ^{10}Be ($^{10}Be_{met}$), produced in the atmosphere and deposited on Earth's surface, and so I will limit discussion to that fraction. As a tracer of nuclear reactions occurring in the atmosphere, $^{10}Be_{met}$ has been employed for a wide variety of applications, including the quantification of erosion and chemical weathering rates, as a chronometer of pedogenesis, reconstructing past solar activity, benchmarking geomagnetic field strength in sedimentary archives, tracing the contribution of surface sediments to basaltic magmas, and tracing the origins of atmospheric dust.

Section 1a: Production and deposition of ^{10}Be

Because $^{10}Be_{met}$ is produced by cosmic rays, it is important first to understand the systematics of cosmic rays impinging on Earth and interacting with the atmosphere. The majority of cosmic rays that reach Earth originate from outside of the solar system, but within our galaxy. This "galactic flux" is composed primarily of protons and smaller amounts of alpha particles, heavier nuclei, and electrons (Gosse & Phillips, 2001). The galactic cosmic rays reach energies of up to 10^{10} eV, accelerated in space by supernova explosions. A small fraction that originate from outside the Milky Way reach even higher energies up to 10^{20} eV (Gosse & Phillips, 2001). A lesser component of cosmic radiation is emitted from the sun, but these solar cosmic rays are of lower energies, and their contribution is generally negligible to $^{10}Be_{met}$ production (Lal & Peters, 1967).

Other than nearby brief supernova events, which produce intense bursts of cosmic rays, the flux of galactic cosmic rays is believed to be relatively constant and isotropic (Gosse & Phillips, 2001). Because incoming cosmic rays are charged particles they are steered by both the solar magnetic and geomagnetic fields. The cosmic ray flux reaching Earth, therefore, depends on the strength of the solar and geomagnetic fields, which vary over time. Once the cosmic rays reach the vicinity of Earth, they are deflected by the geomagnetic field lines. Lower-energy particles are sufficiently slow that they are easily deflected and cannot cross magnetic field lines, while higher-energy particles have enough momentum to carry them across magnetic field lines. Because the geomagnetic field is to first order a dipole, with magnetic field lines converging at the poles, the lower-energy cosmic rays are funneled towards the poles, and only particles with a sufficiently high rigidity (momentum/charge) are able to penetrate at lower latitudes (Masarik & Beer,1999; 2009). The result is that ^{10}Be production in the atmosphere is highest near the poles, and lowest near the equator (Lal & Peters, 1967). 10Be production rate also varies with atmospheric depth, which I discuss below.

Two main factors contribute to variability in the cosmic ray flux and ^{10}Be production rates in the atmosphere: (1) geomagnetic field strength and (2) solar modulation. I discuss each of these in turn.

Geomagnetic field strength

The production rate of ^{10}Be (as well as other meteoric cosmogenic nuclides such as ^{14}C and ^{36}Cl) scales temporally depending on the strength of the geomagnetic field. Models predict higher production rates during periods of low field strength (Heikkilä et al., 2008; Masarik & Beer, 2009; Field et al., 2006). Heikkilä et al. (2009) model ^{10}Be flux across latitudes in current magnetic field strength and at a geomagnetic minimum in an attempt to examine how ^{10}Be flux might have changed during periods such as the Laschamp event. While they find that atmospheric production rate and ^{10}Be flux increase globally during geomagnetic minima, they also find that each latitude receives the same fraction of total ^{10}Be flux regardless of field strength. Nevertheless, actual modulation of ^{10}Be flux during a geomagnetic low such as the Laschamp event may happen to occur at the same time as changes in climate that affect

atmospheric circulation and precipitation rates and patterns, which can confound experimental verification of production rate variations. I discuss these implications in the following section.

Solar modulation

The flux of galactic cosmic rays is also modulated by changes in solar activity. Plasma clouds with internal charge and magnetic fields attenuate the galactic flux before they reach Earth (Lal & Peters, 1967). Evidence of solar modulation can be seen in ice cores with sufficiently short temporal resolution, where the ^{10}Be concentration follows the eleven-year cycle of sunspot activity. Cosmogenic nuclide production rates appear to be highest during minima of sunspot activity when the sun's magnetic field and solar wind are at their weakest point (Morris, 1991). In computational models of cosmogenic nuclide production, solar modulation is accounted for in a parameter known as the "modulation potential," (ϕ). This value is determined at different points in time based on reconstructions of solar activity and comparison to a reference local interstellar spectrum of galactic cosmic rays (Poluianov et al., 2016).

Atmospheric production of ^{10}Be

After entering the atmosphere, energetic cosmic rays may produce cosmogenic nuclides in a number of ways. Spallation is by far the dominant pathway of ^{10}Be production within the atmosphere (Lal & Peters, 1967). Spallation reactions occur when cosmic rays disintegrate the target nucleus resulting in the production of lighter cosmogenic nuclides, and "secondary" particles including protons, neutrons and mesons (Gosse & Phillips, 2001). In the atmosphere, $^{10}Be_{met}$ is produced from a variety of heavier targets, primarily ^{14}N, ^{16}O, and to a lesser degree ^{12}C. If energetic enough, the secondary particles continue to induce further nuclear disintegrations. The resulting cascade of particles and cosmogenic nuclides increases in magnitude with atmospheric depth to a point known as the Pfotzer Maximum. Below this point the intensity of cosmic rays, secondary particles, and resulting cosmogenic nuclide production attenuate such that only a small fraction of cosmic secondary radiation reaches Earth's surface (Gosse & Phillips, 2001).

As a result of this depth-dependent attenuation, the majority of ^{10}Be is produced within the stratosphere, and a small amount is produced within the troposphere (Lal & Peters, 1967; Heikkilä et al., 2009). An even smaller portion, referred to as "in situ ^{10}Be" is produced within solids in the upper crust. The production rate of in situ ^{10}Be is several orders of magnitude lower than the production rate of meteoric ^{10}Be. In totality, nucleons (protons and neutrons) are responsible for the vast majority of cosmogenic nuclide production within the atmosphere (Lal & Peters, 1967). Mesons, muons, electrons, and γ-rays contribute a very small fraction of production, and are more important for in situ ^{10}Be production (Gosse & Phillips, 2001).

Deposition of ^{10}Be

Even though atmospheric ^{10}Be production varies with latitude, stratospheric concentrations of $^{10}Be_{met}$ are relatively homogenous in each hemisphere. This is due to its long residence time of one-to-two years within the stratosphere (Heikkilä et al., 2009). As a result, the deposition of $^{10}Be_{met}$ at Earth's surface is greatest at mid latitudes because stratosphere-troposphere exchange is high at the tropopause breaks in the sub tropics, which occur at the boundaries between the Hadley and Ferrel cells (Heikkilä et al., 2009).

After ^{10}Be is produced in the atmosphere it associates with aerosols, the majority of which are deposited via wet deposition in rain. Even within a single precipitation event, the concentration of ^{10}Be (and other meteoric cosmogenic nuclides such as ^{7}Be and ^{36}Cl) within the precipitation declines as aerosols are flushed from the atmosphere (Knies et al., 1994). This phenomenon is referred to as the "rain-out" effect. Dry deposition of aerosols and associated ^{10}Be is minor except in arid regions where precipitation is infrequent.

Graly et al. (2011) find that on a global scale, the flux of meteoric ^{10}Be is a function of latitude and precipitation rate (Eq. 1.1.1). Their empirically derived equation is widely used to calculate ^{10}Be deposition rates at a given field site using only the precipitation rate, P, and the latitude, L. Their equation does not take into account the site-specific aeolian flux of ^{10}Be, delivered in association with recycled dust. However, this equation assumes a linear relationship between ^{10}Be flux and rainfall, and does not account for any rain-out effects.

$$^{10}Be_{flux} = P\left(\frac{1.44}{1+e^{\frac{30.7-L}{4.36}}} + 0.63\right) \times 10^4$$

Eq. 1.1.1

(Eq. 2 from Graly et al. 2011)

P = Precipitation in cm/yr

L = Latitude (0-90º)

$^{10}Be_{flux}$ = Flux of ^{10}Be from rainfall (atoms/cm^2/yr)

The role of climate in modulating the ^{10}Be flux to a given site is difficult to constrain. Field et al. (2006) assess the effects of increased atmospheric CO_2 concentration and volcanic aerosols in order to examine climate-related changes in ^{10}Be deposition on ice sheets and glaciers. Their model predicts that CO_2-induced atmospheric warming may result in lower residence times of ^{10}Be and ^{7}Be within the stratosphere. They also predict higher precipitation rates at high latitudes. Nevertheless, they conclude that atmospheric warming may only minimally affect ^{10}Be flux, but may create a "dilution effect" in ice cores where heightened precipitation rates yield lower ^{10}Be concentrations.

Numerous other factors that impact climate and atmospheric aerosols can influence the spatial distribution of ^{10}Be flux. Large volcanic eruptions may be followed by a 1-2 year period of global cooling due to the emissions of volcanic aerosols. Field et al. (2006) find that this may briefly impact ^{10}Be records. They predict minimal effects on Greenland and more varied impacts on ice cores from Antarctica. Field et al. (2006) also model the effects of sea surface temperature on ^{10}Be flux in order to examine the effects of the Younger Dryas and 8.2 ka cold events, which are believed to correspond with reduced North Atlantic deep water circulation. They find that changes in sea surface temperatures may result in spatial changes in ^{10}Be flux.

Once deposited, ^{10}Be may be "recycled" in aeolian dust. Lal (2007) finds varying contributions of dust-derived ^{10}Be in ice cores from Antarctica and Greenland. The magnitude of dust

movement is highly related to climate. As aeolian dust is fine-grained, and ^{10}Be concentration is higher in finer grained sediment, dust deposition may increase the flux of ^{10}Be to a site.

Section 1b: Environmental geochemistry of beryllium

In this section I discuss factors that affect the retention and mobility of beryllium. Beryllium is retained by adsorption to environmental surfaces, incorporation into secondary pedogenic phases, complexation by inorganic and organic and species, and uptake by biota. While each of these processes may vary in importance in different settings, in a meta-analysis of ^{10}Be in soil profiles, Graly et al. (2010) conclude that, globally, no single factor controls the concentration of beryllium.

pH

The speciation of beryllium in water is dependent on pH. Below pH ~5 beryllium is primarily dissolved as a divalent cation, and is hydrated by four water molecules in tetrahedral formation (Boschi & Willenbring, 2016b). Between pH ~5 and pH ~12, beryllium forms an insoluble hydroxide via hydrolysis. Above pH ~12, beryllium forms $Be(OH)_3^-$ and once again becomes soluble (Brown et al., 1992).

Adsorption is the accumulation of a species at an external surface of an adsorbent (Maurice, 2009). For beryllium, adsorption is likely a two-stage process involving an initially rapid association with easily accessible sites, and a long-term, gradual migration to more difficultly accessed adsorption sites (You et al., 1989). Outer-sphere adsorption occurs when a hydrated species electrostatically associates with a surface. Species that are adsorbed in this manner are affected by ionic strength. Inner-sphere adsorption is more stable and involves bonding of the species directly to the surface (Boschi & Willenbring, 2016b).

The distribution of beryllium between solution and environmental surfaces can be expressed by the distribution coefficient, K_d. The value of K_d for beryllium depends on the behavior of the surfaces and environmental conditions.

$$K_d = \frac{[Be]_{adsorbed}}{[Be]_{dissolved}}$$

Eq. 1.1.2

At neutral to alkaline conditions, You et al. (1989) report K_d values ranging from 10^5 for clay minerals to $>10^6$ for manganese oxides and weathering products of andesite. Nevertheless, they find that K_d decreases by four orders of magnitude when pH is lowered to 2.

Because beryllium forms insoluble hydrolysate as pH becomes basic, Aldahan et al. (1999) argue that K_d is only valid as a descriptor of beryllium mobility at pH $\leq$6. However, in the presence of humic acid, beryllium may exist primarily as a humate complex in the pH range of ~2 to 11 (Takahashi et al., 1999), thus complicating the simple view of K_d in equation 1.1.2. The adsorption of organo-beryllium complexes to various surfaces has been unexplored, but could be a mechanism of beryllium retention.

Testing the utility of equation 1.1.2, Boschi & Willenbring (2016b) find that a reduction in pH results in high percentages of desorption of beryllium from clay minerals as expected. In contrast, they found that acidification can also lead to heightened retention of beryllium in the presence of certain organic ligands. They ultimately conclude that organic matter, specifically organo-beryllium complexation, may play a large role in controlling the mobility of beryllium in soil. Similarly, in a global meta-analysis of ^{10}Be measurements from soils, Graly et al. (2010) find that pH is not a determinant of ^{10}Be concentration. They therefore postulate that, at low pH conditions in which beryllium tends to desorb from mineral surfaces, organic matter may provide retention mechanisms for beryllium that prevent it from leaching from the soil.

Regardless of whether K_d is controlled by inorganic adsorption reactions or complexation with various organic molecules, we should expect that with sufficiently high water throughput, beryllium will still be lost or translocated within the soil. This was observed in a transect of soil profiles across a precipitation gradient by Dixon et al. (2018), who measured low ^{10}Be inventories after a certain threshold of precipitation was met. They conclude that high rates of

precipitation and a high flux of water through the soil have caused the soil base saturation to decline, leading to acidification and leaching of ^{10}Be. They also note that beryllium may be mobilized in association with organic colloids. Chen et al. (2020) find similar results in soils from China. They find that the soil ^{10}Be concentration has a negative correlation with rainfall in regions with high precipitation (>1200 mm/yr), and a positive correlation in regions with low precipitation (<1200 mm/yr). Likewise, in an Ultisol from the Piedmont region of the eastern U.S., Bacon et al. (2012) estimate that over half of the beryllium ^{9}Be weathered from primary minerals has leached from the soil. Using the loss of ^{9}Be, they quantify a requisite amount of ^{10}Be that was likely lost to leaching as well.

Organic matter complexation

Only a few studies have examined the role of organic matter in retaining beryllium (Boschi & Willenbring, 2016b). Graly et al. (2010) find that ^{10}Be concentration in soil does not correlate with organic carbon content. Bulk organic carbon content includes both particulate organic matter (i.e. tissue from leaves) as well as molecular organic matter such as organic acids that could play a larger role in the retention of beryllium. Very little work has examined the roles of specific organic geochemical fractions (i.e., specific organic acids, functional groups, or the concentration of organic matter associated with oxides) in the retention or loss of Be in the environment.

Boschi & Willenbring (2016 a, b) have started to address this large gap in the literature. Among five common organic functional groups (alcohol, carboxylic acid, amine, sulfonate, and phosphonate) and four minerals (illite, montmorillonite, kaolinite, and goethite) they find that phosphonate retains the most beryllium.

Beyond organic complexation in the soil, beryllium can also be incorporated into biomass. Moore et al. (2021) measure beryllium isotope concentrations in the roots and leaves of deciduous trees, as well as the soils below. In a hickory forest in Indiana they find that the ^{10}Be flux to the soil surface is dominated by biocycling through leaves rather than ^{10}Be flux from

fallout. Beryllium is sourced from the soil and is taken up into the biomass of the hickory tree through its roots.

Incorporation/coprecipitation into secondary phases

Our knowledge of beryllium distribution between different geochemical pools in soils and sediments comes from sequential extractions of operationally defined components. In river sediment from the tropical Amazon basin, Wittmann et al. (2012) find that the fraction of total beryllium that is associated with crystalline and amorphous oxides is orders of magnitude higher than the fractions that are reactive (weakly adsorbed), associated with organics, or contained within primary minerals. In contrast, in river sediment from the Czech Republic, Dannhaus et al. (2018) find similar concentrations of beryllium in the oxides and the reactive pools.

Barg et al. (1997) examine the geochemical distribution of beryllium in soils using a slightly different extraction procedure. While they also find substantial fractions of oxide-associated beryllium, they report that in some soils a substantial fraction of beryllium may be associated with organic matter. Singleton et al. (2017) find that the concentration of ^{10}Be in river sediment from southwest China strongly correlates with the concentration of acid-extractable pedogenic grain coatings, as well as acid-extractable Fe and Mn. Nevertheless, while monitoring fallout radionuclide accumulation in sediments and various phyllosilicates, they find that the retention of ^{7}Be ($t_{1/2}$ = 53 days) does not depend on the concentration of acid extractable Fe or Mn. Singleton et al. (2017) conclude that the widely observed association of ^{10}Be with secondary Fe/Mn (hydr)oxides is the result of time-dependent pedogenic and sedimentary processes. They also postulate that organic matter may play an important role in the initial retention of fallout beryllium.

The extractions discussed above imply that beryllium may be incorporated into, or co-precipitate with secondary amorphous and crystalline (hydr)oxides over the timescales of pedogenesis. Unfortunately, beryllium is transparent to X-rays, making it difficult to examine the specific mechanisms of retention (Boschi & Willenbring, 2016b). Trace elements can be incorporated

into minerals in specific crystallographic sites, or via occlusion. Occluded trace elements are enveloped by the growing mineral and do not have to occupy a specific crystallographic site.

In theory, the complexation of beryllium by organic matter and the incorporation of beryllium into inorganic secondary phases do not have to be separate processes. In many soils, the most stable pool of organic carbon is associated with Fe and Al (hydr)oxides. In acidic soils, the concentrations of organically complexed Fe and Al predict soil organic carbon concentrations, while concentrations of poorly crystalline Fe and Al phases predict the turnover times of organic carbon (Porras et al., 2017).

Section 2: A review of the applications of beryllium isotopes

Section 2a: Glacial environments

Ice cores and snow pits

As is the case with other archives, the concentration of $^{10}Be_{met}$ in glacial ice is controlled by production rate, atmospheric transport, and deposition. The temporal resolution of the archive often determines which variable exerts primary control on ^{10}Be concentration.

Archives with high temporal resolution can capture changes in production rate due to solar modulation. The portions of the Greenland NGRIP and Dye-3 ice cores from 1389-1994 C.E. have annual resolution. ^{10}Be concentrations in this portion of the cores follows the solar magnetic Schwabe cycle, which currently has a period of 11 years, but which has varied in the past (Berggren et al., 2009). In these cores, Berggren et al. observe high ^{10}Be concentrations during prolonged periods of low solar activity, including the Maunder (~1645-1715 C.E.), Dalton (~1790-1830 C.E.), and Spörer (~1415-1535 C.E.) grand solar minima. During the examined interval they also find a correlation between ^{10}Be and neutron flux measured from neutron monitors, which records the impact of solar modulation on cosmic ray flux.

There are several motives for employing $^{10}Be_{met}$ as a record of solar activity. Ice cores are especially attractive archives for exploring the relationships between climate and solar activity. Secondly, the record of solar activity can be used to tune models of cosmogenic nuclide production rates. For example, Vonmoos et al. (2006) use $^{10}Be_{met}$ from the Greenland Ice Core Project to reconstruct Holocene solar variability and its impact on the local galactic cosmic ray flux.

Some ^{10}Be archives that achieve event-scale resolution can record seasonal changes in atmospheric transport processes. Pedro et al. (2006) examine ^{10}Be concentrations in snow pits from Law Dome, Antarctica. They find heightened ^{10}Be concentrations during the late summer and early autumn, corresponding with measured increases in stratospheric aerosols, and marked by a rise in $^{10}Be/^{7}Be$. Archives that have <1 yr resolution are particularly useful for examining atmospheric transport because ^{10}Be has a ~1-2 yr residence time in the stratosphere, long enough to filter out changes in production rate. Nevertheless, other methods have been employed to examine the influence of atmospheric transport on ^{10}Be flux in archives with lower temporal resolution. For example, Wagner et al. (2000) use decay-corrected $^{10}Be/^{36}Cl$ in the summit GRIP (Greenland Ice Core Project) ice core as an index for changes in atmospheric transport. Like meteoric ^{10}Be, meteoric cosmogenic ^{36}Cl ($^{36}Cl_{met}$) flux is also modulated by changes in production rate, however their different chemical behaviors result in varying responses to changes in atmospheric transport.

Over longer timescales changes in geomagnetic field intensity are also recorded by $^{10}Be_{met}$ in glacial ice. Wagner et al. (2000) use meteoric ^{10}Be and ^{36}Cl in the GRIP ice core to reconstruct the paleo-intensity from 20-60 ka. The pairing of ^{10}Be with other cosmogenic radionuclides is common in this application because all of the cosmogenic nuclides should scale with magnetic field strength, but they have different mechanisms for deposition. Muscheler et al. (2005) use ^{10}Be from the Summit ice core in Central Greenland, $^{36}Cl_{met}$ from the GRIP ice core, and ^{14}C in tree rings to reconstruct geomagnetic field intensity over the last 60 ka. In conjunction, these data demonstrate how changes in the carbon cycle modulate atmospheric ^{14}C concentration before 10 ka.

^{10}Be has also been used to examine geomagnetic field dynamics during reversals. For example, Raisbeck et al. (2006) observe a heightened ^{10}Be flux during the Matuyama-Brunhes geomagnetic reversal (776 ± 12 ka) in the EPICA Dome C ice core in Antarctica, corresponding with low geomagnetic field strength.

Although ^{10}Be is sensitive to geomagnetic field strength, it does not directly measure the field, and it is complicated by solar modulation, atmospheric delivery, and scavenging. Modern models of cosmogenic nuclide production, such as LSDn (Lifton et al., 2014) do not to calibrate against ^{10}Be records directly, but instead employ well developed geomagnetic field paleointensity models including CALS3K.3 (the last 3 ka; Korte et al., 2009), CALS7K.2 (3-7 ka), GLOPIS-75 (7-18 ka; Laj et al., 2004), and PADM2M (beyond 18 ka; Ziegler et al., 2011). These geomagnetic models are calibrated to paleointensity measurements from sedimentary records, volcanic rocks, and archaeomagnetic records rather than cosmogenic nuclide proxies of field strength.

Examining pre-glacial conditions and reworking of soil & saprolite

In glacial environments with minimal erosion, pre-glacial features such as soil and saprolite may be preserved beneath or within the ice. ^{10}Be can be used as an indicator of paleo-exposure as well as a tracer of soil and saprolite material as it is removed and re-worked by the ice.

Ebert et al. (2012) examined concentrations of ^{10}Be in saprolite and overlying till in two pits from northern Sweden. They find that the amount of ^{10}Be in the till is higher than the amount that could have accumulated after de-glaciation. Thus, they argue that only minimal erosion has occurred, and that soil (containing high concentrations of ^{10}Be) is the primary component of the till. They also propose that, in some circumstances, ^{10}Be inventory could be used to more precisely date saprolites in previously glaciated areas. They indicate that this would be possible at a site containing some residual soil material, indicating that minimal erosion has occurred. Additionally, the presence of a thick glacial deposit over the site would ensure that no extra ^{10}Be was added post glaciation.

In the Greenland Ice Sheet Project 2 (GISP2) ice core from Summit Greenland, Bierman et al. (2014) find that ^{10}Be concentration and percent organic carbon increase with depth down to the base of the ice. They find a maximum ^{10}Be concentration of 3.8×10^8 atoms/g, which is comparable to modern concentrations within Alaskan permafrost soil, which they suggest could be a modern analog to the pre-glacial precursor at the core site. Bierman et al. therefore postulate that the ice sheet has been essentially non-erosive for the Pleistocene, and that high concentrations of ^{10}Be and organic carbon are from locally derived pre-glacial soil.

Graly et al. (2018) measure ^{10}Be in grain coatings from sediment at the margins of the Greenland Ice Sheet. They find concentrations of ^{10}Be ranging from below 10^6 atoms/g up to 2.1×10^8 atoms/g, with the highest concentrations in the ice-bound sediment, and the lowest concentrations in glaciofluvial sediment. They also measure δ^{18}O and δ^2H in order to constrain the processes by which ice-bound sediment is entrained into the ice. Their data from the Upernavik area show high δ^{18}O values relative to the meteoric water line, indicating that regelation is the primary mechanism of sediment incorporation. In contrast to Bierman et al. (2014), Graly et al. (2018) find that the maximum ^{10}Be and organic carbon concentrations occur higher up in the ice column. Graly et al. propose that the parts of the core with lower and higher ^{10}Be and organic carbon concentrations are from different sources, and were potentially entrained in the ice via different mechanisms.

Using a compilation of ^{10}Be concentrations from soil profiles globally, Graly et al. (2010) find a strong correlation (R^2=0.92) between the maximum soil ^{10}Be concentration and the total soil-profile inventory of ^{10}Be. They use this relationship to calculate expected ^{10}Be inventories of the source soils. Given the assumption that the flux of ^{10}Be was the same in previous interglacial periods as it was in the mid-Holocene, Graly et al. (2018) calculate that the soil was exposed for 90-197 ka before glaciation at Upernavik.

In specific circumstances, ^{10}Be may be used as an indicator of paleo-environmental conditions. Schiller et al. (2009) examine the distribution of ^{10}Be in a soil profile in the lower Wright Valley in Antarctica containing a paleosol buried by volcanic ash and gravel lag. They find high concentrations of ^{10}Be at the top of the profile, low concentrations in the ash, and high

concentrations in the paleosol below. The distribution of ^{10}Be with depth in the paleosol displays a classic "bulge profile," signifying that physical and chemical illuviation was occurring in the paleosol before burial by the relatively impermeable ash at 3.9 Ma. They therefore conclude that the paleosol formed in much wetter conditions than are present today.

Reconstructing the boundaries of glaciated margins

Measurements of ^{10}Be from marine and subglacial sediment cores are increasingly employed to examine the dynamics of glaciated margins. In a study of sediment cores off the coast of West Antarctica and beneath the ice sheet, Scherer et al. (1998) find that high concentrations of ^{10}Be in diamicton are concurrent with high concentrations of Quaternary diatoms. Their findings support the existence of open marine conditions in the Ross Sea on the margin of the West Antarctic Ice Sheet during the late Pleistocene. Sjunneskog et al. (2007) also examine cores from the Ross Sea and find spatial variability in ^{10}Be concentration and the ^{10}Be/^{9}Be ratio. They conclude that areas depleted in ^{10}Be record sub-ice and sub-ice-shelf conditions, while areas with high ^{10}Be concentration record open marine conditions. Using ^{14}C dates in conjunction with ^{10}Be and diatom concentrations, Yokoyama et al. (2016) constrain the timing of the melting of the Ross Ice Shelf to roughly 1.5-5 ka.

Valletta et al. (2018) examine the authigenic ^{10}Be/^{9}Be ratio in sediments from off the coast of the Wilkes Land Region in order to examine the Pliocene dynamics of the East Antarctic Ice Sheet. They find that the authigenic ^{10}Be/^{9}Be ratio and weight percent opal increase during periods of warming, once again suggesting the presence of open marine conditions. Their measurements of ^{87}Sr/^{86}Sr and εNd in the core indicate that sediment is sourced from a further inland provenance when the ice sheet contracts during warming.

While meteoric input is the primary mechanism of ^{10}Be delivery to the marine environment, Valletta et al. (2018) find concentrations of ^{10}Be that are higher than expected. They propose that extra ^{10}Be may be added to the marine environment by freshwater discharge from the ice sheet. In these polar marine and subglacial environments, the ^{10}Be/^{9}Be ratio seems to be controlled mainly by the supply of ^{10}Be, rather than processes controlling ^{9}Be delivery (Valletta et al., 2018).

Valletta et al. (2018) also examine opaline biomineralization as a potential geochemical mechanism of ^{10}Be concentration. Concentrations of ^{9}Be in the opal range from 2.17 to 61.28 ng/g, with at most 18% of the reactive (non-primary mineral) ^{9}Be residing in the opal within a given sediment layer, suggesting that beryllium may have a greater preference for clay minerals. While they did not have enough opaline material to measure ^{10}Be, they suggest that depth profiles of ^{10}Be/^{9}Be in seawater could be reconstructed by measuring ^{10}Be and ^{9}Be in opal and authigenic materials, with the opal representing the upper water column, and the authigenic materials representing an average across depth.

^{10}Be in glacial water

^{10}Be has also been employed as a tracer of the movement of water masses. Frank et al. (2002) find that ^{10}Be concentrations in seawater trace the rising core of the North Atlantic Deep Water mass as it rises from the polar frontal zone into the Antarctic zone and up into the Weddell Sea. They compare the distribution of ^{10}Be with that of ^{230}Th, which is produced in the water column from U-series decay. The scavenging time of ^{230}Th (~30 yrs) complicates its use as a tracer. Frank et al. conclude that ^{10}Be can be used as a "quasi-conservative" tracer of particle motion in southern polar waters.

^{10}Be dynamics in glacial environments

Taken as a whole, the literature discussed above sheds light on the dynamics of ^{10}Be in glacial environments. Two large variables appear to govern ^{10}Be inventory beneath the ice. First, the magnitude of subglacial erosion dictates the degree to which inherited ^{10}Be and any added ^{10}Be are removed. Second, melting of the ice can deliver ^{10}Be to the base, thus controlling the flux during glaciation.

Section 2b: Marine and lacustrine records

In contrast to ice cores, which record the direct deposition of ^{10}Be from precipitation, the concentration of ^{10}Be in marine and lacustrine records is also impacted by geochemical and sedimentary processes. The ^{10}Be concentration is often difficult to interpret, and so beryllium is normally measured as an isotopic ratio of meteoric ^{10}Be to native ^{9}Be (^{10}Be/^{9}Be). While marine and lacustrine archives of ^{10}Be have been examined for many of the same motives as ice cores, including the reconstruction of geomagnetic field strength and solar modulation, they have more unique applications.

The ^{10}Be in oceanic archives is mainly derived from direct precipitation over the water body, with a minor terrigenous contribution from rivers. In contrast, ^{9}Be is primarily delivered to the oceans by fluvial transport, and is ultimately derived from chemical weathering on the continents (Bourles et al., 1989). Given the low solubility and high particle reactivity of beryllium in the moderate pH range, beryllium is almost exclusively bound to sediment in marine settings, and therefore the ^{10}Be/^{9}Be ratio does not easily homogenize across a basin. Thus, the ^{10}Be/^{9}Be ratio recorded in a marine sedimentary archive represents a local record that depends in-large-part on the geochemistry of nearby rivers. (von Blanckenburg et al., 1996) For example, Brown (1985) finds a negative relationship between pH-corrected K_d for beryllium and Si/(K+Na-Cl). He infers that this relationship is the result of changes in particle surface properties, ultimately indicating that K_d is higher in waters that drain from regions with greater secondary mineral formation.

McHargue et al. (2000) find up to a 1000 year lag between the measured geomagnetic paleointensity signal (natural remanent magnetization normalized by anhysteretic remanent magnetization) and ^{10}Be in a late Pleistocene core from the Guaymas basin in the Gulf of California. This highlights the impact of long transit times from sediment source at the sea surface to the marine floor.

Chemical weathering from the long-term (9 Ma) beryllium record in sediment cores

For decades the $^{10}Be/^{9}Be$ ratio in marine sediments has been explored as a metric of chemical weathering. The concentration of ^{9}Be in the felsic continental crust is an order of magnitude higher than ^{9}Be concentrations in carbonate and mafic rocks. Thus, compared to other proxies of chemical weathering such as Os and Sr isotopes, the $^{10}Be/^{9}Be$ ratio in marine sediments is less impacted by carbonate weathering and hydrothermal processes. Therefore Be isotopes have been viewed as a potentially more reliable metric of the weathering of silicates on the continents.

Originally, Bourles et al. (1989) found that the $^{10}Be/^{9}Be$ ratio changed systematically over the last 9 million years, which they attributed to changes in the ^{9}Be flux (i.e. changes in chemical weathering rate). However, Bourles et al. used a ^{10}Be half-life of 1.5 My to correct for radioactive decay. Experiments reported in 2007 (Nishiizumi et al.) and 2010 (Chmeleff et al.; Korschinek et al.) revised the ^{10}Be half-life to 1.36 (± 0.07 MY). The most recent experiments to constrain the ^{10}Be decay constant report a half-life of 1.387×10^{6} years (Chmeleff et al., 2010; Korschinek et al., 2010).

When the new half-life was used to correct the marine records, Willenbring and von Blanckenburg (2010) reported that the marine $^{10}Be/^{9}Be$ record shows no long-term trend, suggesting that the global chemical weathering flux has remained stable across Neogene cooling. I discuss the implications of this finding in more detail in chapter 2. Li et al. (2021) question the efficacy of the marine $^{10}Be/^{9}Be$ ratio as a metric of weathering flux. Instead they suggest that the ratio is impacted by coastal scavenging processes.

As a record of cosmogenic nuclide production rate and geomagnetic field strength

Beryllium isotopes in individual sedimentary records are difficult to interpret, as the isotope concentrations are influenced by a multitude of temporally varying factors (Aldahan, 2003). Using $^{10}Be_{met}$ data from a global stack of deep sea sediments, Frank et al. (1997) normalize ^{10}Be to excess ^{230}Th in order to control for the effects of post-depositional sediment redistribution.

Their work successfully elucidates relationships between the marine records, geomagnetic field intensity, and production rate.

Using multiple archives of ^{0}Be from varying geographic settings can help to distinguish between local and global phenomena. In a Mediterranean sediment core from the Tyrrhenian Sea, Castagnoli et al. (1995) observe a ^{10}Be peak at 34 ka, matching similar peaks from the same time in the Antarctic Vostok and Dome C ice cores. They therefore conclude that this peak was the result of heightened ^{10}Be production rate, and not local shifts in flux.

Much like ice cores, the temporal resolution of marine and lacustrine archives determines what variables can be observed by measuring ^{10}Be concentration. Czymzik et al. (2015) measure ^{10}Be/^{9}Be in annual-resolution varves made of calcite and diatoms with organic sub-layers from Lakes Tiefer See and Czechowskie in the central European Lowlands. They find that the ^{10}Be/^{9}Be ratio tracks changes in ^{10}Be production rate due to solar modulation, correlating with counts from neutron monitors from 1983-2009 (Czymzik et al., 2015).

Marine Ferromanganese Crusts and Nodules

Marine ferromanganese crusts and nodules (herein referred to as "crusts" and "nodules") are Fe and Mn (hydr)oxides that precipitate from sea water. Unlike clastic sediments, there is very little redistribution of beryllium after precipitation in crusts and nodules. Mangini and Segl (1986) find very low diffusion rates of $\leq 1.0 \times 10^{-8}$ cm^2/yr for beryllium within manganese crusts, making them accurate temporal records of beryllium isotopes with minimal disturbance.

There are two main uses for Be isotopes in Mn nodules. The first is as a dating method. In order to use the ^{10}Be/^{9}Be ratio as a chronometer for crust or nodule growth, the initial ^{10}Be/^{9}Be ratio is assumed to be the value of the seawater from which it precipitated. After forming, the ratio declines with time as ^{10}Be decays. Many botryoidal nodules contain laminated growth bands. In these cases, the ^{10}Be/^{9}Be ratio is often measured in a transect from core to rim in order to examine changes in the nodule growth-rate over time. The ages calculated in this way agree with nannofossil biostratigraphy in crusts from the western and central Pacific extending back to 12.8

Ma (Cheng et al., 2006), as well as ultrafine-scale magnetostratigraphy in a crust from the northwest Pacific (Oda et al., 2011).

An example of this approach is Grahm et al. (2004), who measure growth rates in nodules from a sediment core from the Campbell Plateau in the Southwest Pacific. They find that growth rates decrease towards the top of the sediment core, which they hypothesize is caused by the strengthening of the Deep Western Boundary Current since 10 Ma.

Alternatively, if an independent chronometer of Mn-nodule growth is available, then the nodule can be used as an archive of changing sea water $^{10}Be/^{9}Be$. The dating method that is employed most frequently is argon-argon dating of cryptomelane, $K(Mn^{4+},Mn^{2+})_8O_{16}$. This is a difficult and time-consuming approach, since cryptomelane must be physically separated from potassium-bearing impurities. However, once the manganese nodule is dated, the $^{10}Be/^{9}Be$ can be used to learn about changes in global weathering rate over time (e.g., Willenbring and von Blanckenburg, 2010).

Section 2c: Terrestrial records

Soils & fluvial sediment

Soils are reservoirs of ^{10}Be , with fluxes of ^{10}Be into and out of the soil column. In this respect they are different from other archives of $^{10}Be_{met}$ such as ice and sediment cores, loess, and speleothems which accumulate ^{10}Be over time. The main use of ^{10}Be in soils and fluvial sediment is a direct tracer of pedogenesis and erosion.

The inventory of ^{10}Be in a soil pit is often used to determine a minimum soil age, (minimum since there will likely be ^{10}Be loss from erosion or leaching), or an erosion rate, assuming steady state weathering, soil formation, and erosion. In these techniques, the whole-profile inventory is calculated by adding inventories of different horizons and multiplying by their different horizon thicknesses and densities (Willenbring and von Blanckenburg, 2010):

$$\boldsymbol{I = \sum_i N_i \times \rho \times \Delta Z_i}$$

Eq. 1.2.1

(Eq. from Willenbring and von Blanckenburg, 2010)

I = Inventory of ^{10}Be (atoms/cm^2)

N_i = Atoms of ^{10}Be in layer i

ρ = Density of layer i (g/cm^3)

ΔZ_i = Thickness of layer i (cm)

Assuming a steady flux of ^{10}Be and no loss from erosion or leaching, the minimum soil age can be calculated using the measured whole-profile inventory (Brown et al., 1988).

$$\boldsymbol{I = \frac{Q(1-e^{-\lambda t})}{\lambda}}$$

Eq. 1.2.2

(Eq. from Brown et al. 1988)

I = Inventory of ^{10}Be (atoms/cm^2)

Q = Atmospheric flux of ^{10}Be (atoms cm^{-2} yr^{-1})

λ = Decay constant of ^{10}Be

t = time (yr)

Alternatively, given a steady state of weathering and erosion, an erosion rate can be measured, assuming that all eroded material is sourced from the surface layer (Eq. 2 from Brown et al., 1988):

$$N = (q - \varepsilon\eta)/\lambda$$

Eq. 1.2.3

(Eq. 2 from Brown et al. 1988)

N = Inventory of ^{10}Be (atoms/cm^2)

q = Atmospheric flux of ^{10}Be (atoms cm^{-2} yr^{-1})

ε = Erosion rate (g cm^{-2} yr^{-1})

η = The concentration of ^{10}Be at the soil surface (atoms/g)

λ = Decay constant of ^{10}Be

Examinations of erosion that employ ^{10}Be in fluvial sediment often assume that the ^{10}Be concentration in the sediment is a representative average from the hillslopes of the watershed. Brown et al. (1988) calculate a watershed erosion index based on sediment gauging data and ^{10}Be measurements. This index allows for the comparison of long-term and modern erosion rates.

$$\varepsilon = M\eta'/Aq$$

Eq. 1.2.4

(Eq. 3 from Brown et al. 1988)

ε = erosion index

M = annual sediment load (g)

η'= ^{10}Be concentration in sediment (atoms/g)

A = Basin area (cm^2)

q = Atmospheric flux of ^{10}Be (atoms cm^{-2} yr^{-1})

Using this technique, Brown et al. (1988) find that many watersheds in the Piedmont region of Appalachia have erosion indices greater than 1, indicating that the modern erosion, as measured by sediment gauging, outpaces long-term erosion, measured by ^{10}Be. They infer that erosion rate has increased as a result of approximately 200 years of intensive colonial and post-colonial agricultural land use.

The use of ^{10}Be alone to determine erosion rates and soil ages requires multiple assumptions, including irreversible retention by soils and sediment, and uniform distribution of ^{10}Be. This means that there can be no loss of ^{10}Be in the dissolved phase, and the analyzed sample must represent an average ^{10}Be concentration for the landscape. Singleton et al. (2017) demonstrate that these conditions are almost never met, as beryllium retention and distribution depends on

numerous factors including grain size, mineralogy, and the development of secondary phases and grain coatings, as well as geochemical conditions such as pH.

Barg et al. (1997) measure $^{10}Be/^{9}Be$ ratios in authigenic minerals to quantify rates of soil formation, with the incorporation of ^{9}Be released from primary minerals during chemical weathering. They employ a simple model of soil production in which all secondary clays and (hydr)oxides are produced at the weathering front near the soil-rock interface. Thus, in this model, the authigenic minerals lock-in a $^{10}Be/^{9}Be$ ratio when they crystalize at the base of the soil profile, and the ratio declines with mineral-age as the ^{10}Be decays. This approach assumes that these phases are "closed-systems" with no post-crystallization exchange of Be isotopes, and that authigenic minerals are not produced elsewhere in the soil profile (a condition which they recognize is not met).

$$R(t) = R_{\circ}e^{-\lambda t}$$

Eq. 1.2.5

(Eq. 6 from Barg et al. 1997)

R(t) = $^{10}Be/^{9}Be$ in authigenic minerals at time t

R_o = $^{10}Be/^{9}Be$ in authigenic minerals at the weathering front, where they are assumed to form

λ = Decay constant of ^{10}Be

t = age (yr)

In order to isolate the $^{10}Be/^{9}Be$ ratio from the authigenic soil fractions, Barg et al. (1997) use a sequential chemical extraction procedure. They divide the soil into different geochemical pools, including the adsorbed phase, organic phase, Fe-hydroxide phase, clay phase, Al-hydroxide phase, and quartz with other detrital minerals.

Barg et al. (1997) show that the $^{10}Be/^{9}Be$ ratio in soils can change rather dramatically with depth, but also between phases within a single soil horizon. While these differences may contain some information about the age of authigenic phases, the complicated process of pedogenesis makes simple interpretation difficult.

Loess

So far, ^{10}Be measurements in loess come exclusively from the loess plateau in China. Similar to other archives, loess records reflect multiple climate signals and changes in ^{10}Be production rate. If examined over short timescales, $^{10}Be_{met}$ tracks solar modulation. Over longer timescales, the Chinese ^{10}Be loess record is particularly sensitive to changes in rainfall and dust flux, and is influenced by geomagnetic modulation of ^{10}Be production.

Zhou et al. (2014) use ^{10}Be as a proxy for geomagnetic field intensity in order to study a previously observed ~25 kyr offset in the timing of the Brunhes-Matuyama geomagnetic reversal in loess. A disagreement between the ^{10}Be and the detrital remanent magnetization in the loess indicate that post-depositional overprinting has occurred in the magnetic signal, causing the geomagnetic reversal to appear to have occurred earlier. Their findings confirm the validity of the Chinese loess timescale.

The most prominent use of the loess ^{10}Be record is as a paleo-precipitation record. Zhou et al. (2007) use $^{10}Be_{met}$ from the Luochuan loess section to calculate quantitative values for paleo-precipitation and geomagnetic field intensity over the last 80kyr. They use magnetic susceptibility and coercivity measurements in order to deconvolve the geomagnetic, original dust, and precipitation signals. Dry dust approaches an end-member susceptibility of ~25 ($x10^{-8}$ m^3/kg), while pedogenic phases formed during wet times have much higher susceptibility values. They find a strong linear relationship between magnetic susceptibility and the loess $^{10}Be_{met}$ concentration, Be(M) ($R^2 = 0.88$). Plugging in the value of the dust susceptibility end-member, Zhou et al. (2007) calculate the $^{10}Be_{met}$ concentration in dust, Be(D), to be 1.36 ($x\ 10^8$ atoms/g), comparable to 10^8 atoms/g measured directly in loess in China (Shen et al., 2010).

By subtracting the dust concentration from the total concentration, they calculate a $^{10}Be_{met}$ concentration that has been influenced only by precipitation and modulation of geomagnetic field intensity, subsequent to loess (i.e., dust) deposition Be(P,GM):

$$Be(M) - Be(D) = Be(P, GM)$$

Eq. 1.2.6

(Eq. from Shen et al., 2010)

A closer analysis reveals that the susceptibility and $^{10}Be_{met}$ concentrations are very similar, but do not match perfectly. Using the average relationship between susceptibility of pedogenic phases and $^{10}Be_{met}$ (P,GM) determined by linear regression, they predict the expected value of $^{10}Be_{met}$ for a time series of magnetic susceptibility, as a proxy for precipitation. Deviations between the prediction and the actual measurements are taken as an indication of variation in $^{10}Be_{met}$ flux due to geomagnetic field modulation. Regression shows that about 65% of the variation in dust-corrected $^{10}Be_{met}$ concentration can be explained by precipitation (i.e., susceptibility of pedogenic phases).

In conjunction with speleothem $\delta^{18}O$, the loess $^{10}Be_{met}$ paleo-precipitation record has helped to elucidate climatic dynamics of the East Asian monsoon. Zhou et al. (2007) find that the paleo-precipitation record they calculate from the $^{10}Be_{met}$ loess record is similar to the $\delta^{18}O$ records in speleothems from Dongge and Hulu caves. Previous work suggests that these $\delta^{18}O$ records track the strength of the East Asian summer monsoon.

Beck et al. (2018) extend the rainfall proxy back to 550ka in order to explore the differences and relationships between speleothem $\delta^{18}O$ and the loess $^{10}Be_{met}$ paleo-precipitation record. While the speleothem $\delta^{18}O$ closely tracks high-northern-latitude summer insolation, the paleorainfall from loess $^{10}Be_{met}$ only correlates weakly. Based on this finding, Beck et al. (2018) propose that, instead of reflecting monsoon intensity, the speleothem $\delta^{18}O$ may record moisture mixing of two end-members: low $\delta^{18}O$ moisture from the Indian summer monsoon, and higher $\delta^{18}O$ moisture from the Western North Pacific summer monsoon. They therefore argue that East Asian summer monsoon strength is controlled by low-latitude, rather than high-latitude insolation.

Travertine, tufa, and speleothems

The use of travertine and speleothems as archives of $^{10}Be_{met}$ is understudied, although several recent papers examine travertine. Xu et al. (2019) find that $^{10}Be/^{9}Be$ in travertine from Baishuitai, China tracks changes in solar modulation and ^{10}Be production from 2001-2016 CE, with a lag of 1.5-2.5 years. They note that normalizing by ^{9}Be corrects for seasonal variations in growth rate, and normalization by potassium concentration (an indicator of surface water) corrects for the inclusion of detrital material within the travertine, which may add noise to the ^{10}Be fallout signal. Miyahara et al. (2020) measure ^{10}Be in tufa from Mao Lan National Park in Yunnan Provence, and tufa from Baishuitai National Park in Guizhou Provence, China. They find higher ^{10}Be concentrations during rainy seasons, but steady $^{10}Be/^{9}Be$ across seasons, indicating a constant source of beryllium.

Lundblad (2006) contains the only published measurements of ^{10}Be and ^{9}Be in cave speleothems. She examined the $^{10}Be/^{9}Be$ ratio in stalagmites from South Africa and Tanzania. Her original motive for this work was to explore the since-debunked hypothesis (Lanci et al., 2020) that cosmic ray flux influences climate. The South African speleothem is from Cold Air Cave in Makapansgat valley, and spans both glacial (~24.4 – 13.0 ka) and Holocene (~10.1 - 0.1 ka) intervals. The Holocene speleothem growth rate (~11 mm/100 yr) is much higher than the glacial interval (~2 mm/100 yr), reflecting a wetter Holocene. The Tanzanian stalagmite comes from Mafuriko Quarry Cave in the Tanga Region and formed entirely during a glacial period (~39.1 – 31.9 ka).

In total, Lundlad's work does not reveal connections between Be isotopes and climate. Three peaks in speleothem ^{10}Be concentration in Lundblad's data at approximately 38, 35, and 21 (±2 ka) possibly correspond to ^{10}Be production spikes including the Laschamp and Mono Lake events. However, Lundblad notes that their duration is much shorter than previously observed.

Summary

High fidelity terrestrial records of $^{10}Be_{met}$ flux such as loess appear to faithfully record patterns in long-term precipitation, modulated by the geomagnetic field strength. Short-term records, such as travertine, record rapid fluctuations in meteoric flux due to changing solar modulation. Soils, on the other hand, act as a reservoir, accumulating an inventory of $^{10}Be_{met}$ that is lost over time due to physical erosion and chemical losses to groundwater.

Section 2d: Denudation and weathering intensity from $^{10}Be/^{9}Be$

As discussed above, the single-isotope method of using $^{10}Be_{met}$ to calculate erosion rates requires several assumptions that are mostly unsatisfied. One must assume that the collected sediment sample is representative of the catchment-average $^{10}Be_{met}$ concentration. Riverine sorting of sediment violates this assumption, as $^{10}Be_{met}$ concentration in sediment varies by grain size, mineralogy, and the abundance and composition of pedogenic grain coatings. One way that this has been dealt with is by normalizing $^{10}Be_{met}$ to other associated elements such as iron that scale similarly (Helz & Valette-Silver, 1991). A better way, however, is to normalize against stable ^{9}Be (von Blanckenburg et al., 2012). As ^{9}Be has the same geochemical behavior as ^{10}Be, normalizing by ^{9}Be can help correct for the mobility and non-homogenous distribution of $^{10}Be_{met}$ within soils and sediments. Since the introduction of this method, the $^{10}Be/^{9}Be$ ratio has been increasingly employed in numerous settings to examine geomorphic processes.

Using $^{10}Be/^{9}Be$ to calculate a denudation rate requires several assumptions. Firstly, the long-term flux of $^{10}Be_{met}$ or ^{9}Be into the weathering zone must be equivalent to its flux out (i.e., steady state). This must be true on a timescale described by von Blanckenburg et al. (2012) as approximately 4 to 5 times the residence time of the isotope, approximately 10^3 to 10^5 years. Secondly, the denudation rate must be high enough such that the decay of ^{10}Be within the system is negligible. Thirdly, there must be open-system behavior between pedogenic materials (reactive phase) and the dissolved phase, meaning that the $^{10}Be/^{9}Be$ is free to equilibrate between these pools.

$$^{10}Be_{met}\ Residence\ Time = \frac{I}{F_{met}^{^{10}Be}}$$

$$^{9}Be \quad Residence\ Time \approx \frac{Depth\ of\ Weathering\ Zone}{D} = Denudation\ Timescale$$

Eq. 1.2.7 & 1.2.8

(Eq. from von Blanckenburg et al. 2012)

D = The denudation rate (g cm^{-2} yr^{-1})

$F_{met}^{^{10}Be}$ = The flux of $^{10}Be_{met}$ to the site (atoms cm^{-2} yr^{-1})

I = The integrated inventory of $^{10}Be_{met}$ in the soil profile (atoms/cm^2)

Given these assumptions, a denudation rate can be calculated from measurements of ^{10}Be and ^{9}Be in the reactive or dissolved phase, as well as ^{9}Be measurements in the parent material, remaining primary minerals, and reactive phase. Additionally, a $^{10}Be_{met}$ flux must be measured or calculated from a model, both of which carry their own assumptions. Although von Blanckenburg et al. (2012) derive an equation that permits the calculation of denudation with a known K_d value ($[Be]_{reac}/[Be]_{diss}$) and discharge (Q), if a high K_d value is assumed (meaning that the loss of Be in the dissolved phase is negligible), then the equation can be simplified:

$$\left(\frac{^{10}Be}{^{9}Be}\right)_{reac} = \left(\frac{^{10}Be}{^{9}Be}\right)_{diss} = \frac{F_{met}^{^{10}Be}}{D \times [\,^{9}Be]_{parent}} \left(\frac{[\,^{9}Be]_{min}}{[\,^{9}Be]_{reac}} + 1\right)$$

Eq. 1.2.9

(Eq. 12 from von Blanckenburg et al., 2012)

D = Denudation rate (g/cm^2/yr)

$[\,^{9}Be]_{min}$ = The concentration of ^{9}Be in primary minerals remaining after incongruent weathering (atoms/g)

$[\,^{9}Be]_{reac}$ = The concentration of ^{9}Be in the reactive fraction (adsorbed or incorporated into secondary materials) (atoms/g)

$[\,^{9}Be]_{parent}$ = The concentration of ^{9}Be in the parent material (atoms/g)

$\left(\frac{^{10}Be}{^{9}Be}\right)_{reac}$ = The $^{10}Be/^{9}Be$ in the reactive fraction

$\left(\frac{^{10}Be}{^{9}Be}\right)_{diss}$ = The $^{10}Be/^{9}Be$ in the dissolved fraction

Alternatively, if a total measurement of $^{10}Be/^{9}Be$ is made, the calculation of denudation may be further simplified:

$$\left(\frac{^{10}Be}{^{9}Be}\right)_{total} = \frac{F_{met}^{^{10}Be}}{D \times [\,^{9}Be]_{parent}}$$

Eq. 1.2.10

(Equation 13 from von Blanckenburg et al., 2012)

$[^{10}Be_{total}] = [^{10}Be]_{reac}$

$[^{9}Be_{total}] = [^{9}Be]_{reac} + [^{9}Be]_{min}$

The validity of the assumptions associated with this method have been subject to much investigation (Maher & von Blanckenburg, 2016; Dannhaus et al., 2018).

<u>Weathering rate or intensity</u>

Landscape denudation includes both the physical erosion and chemical weathering components. Therefore, since ^{9}Be is released from primary minerals during chemical weathering, the $^{10}Be/^{9}Be$ ratio in the dissolved and reactive phases also theoretically records information about landscape chemical weathering rate. Nevertheless, previous work with beryllium isotopes does not explicitly solve for a chemical weathering rate using $^{10}Be/^{9}Be$.

$$D = E + W$$

Eq. 1.2.11

D = Denudation rate (i.e. $g/cm^2/yr$)

E = Erosion rate (i.e. $g/cm^2/yr$)

W = Weathering rate (i.e. $g/cm^2/yr$)

^{9}Be has been used on its own to examine chemical weathering. In this approach, the ^{9}Be exported from a watershed is broken down into the mineral, reactive, and dissolved fractional fluxes:

$$1 = f_{min}^{^{9}Be} + f_{reac}^{^{9}Be} + f_{diss}^{^{9}Be}$$

Eq. 1.2.12

(Eq. 6 from von Blanckenburg et al., 2012)

Therefore, the fraction of ^{9}Be that is released during chemical weathering ($f_{reac}^{^{9}Be} + f_{diss}^{^{9}Be}$) is a metric of weathering intensity, or the fraction of denudation accomplished in the dissolved phase (von Blanckenburg et al., 2012; Wittmann et al., 2015; Rahaman et al. 2017).

Calculating the values of $f_{reac}^{^{9}Be}$ and $f_{diss}^{^{9}Be}$ requires a lot of information about the watershed, including data such as discharge and erosion rate that can only be acquired via independent metrics such as long-term stream gauging, *in situ* cosmogenic nuclides, or other means.

$$f_{reac}^{^{9}Be} + f_{diss}^{^{9}Be} = \frac{J_{riv\_reac}^{^{9}Be} + J_{riv\_diss}^{^{9}Be}}{J_{riv}^{^{9}Be}} = \frac{A_{riv} \times E \times [\,^{9}Be]_{reac} + Q \times [\,^{9}Be]_{diss}}{A_{riv} \times E \times \left([\,^{9}Be]_{reac} + [\,^{9}Be]_{min}\right) + Q \times [\,^{9}Be]_{diss}}$$

Eq. 1.2.13

(Eq. 8 from Wittmann et al. 2015)

$J_{riv\_reac}^{^{9}Be}$ = Total flux of ^{9}Be out of the watershed in the reactive phase (g/yr)

$J_{riv\_diss}^{^{9}Be}$ = Total flux of ^{9}Be out of the watershed in the dissolved phase (g/yr)

$J_{riv}^{^{9}Be}$ = Total flux of ^{9}Be out of the watershed (g/yr)

A_{riv} = Surface area of the basin (m^2)

E = Erosion rate

Q = Discharge of river (L/yr)

$[\,^{9}Be]_{diss}$ = Dissolved concentration of ^{9}Be (atoms/L)

However, if the dissolved flux of ^{9}Be ($f_{diss}^{^{9}Be}$) is assumed to be negligible due to high beryllium K_d values, then the $f_{reac}^{^{9}Be}$ metric of weathering intensity can be calculated simply from the ^{9}Be concentration in the reactive and mineral fractions:

$$f_{reac}^{^{9}Be} + f_{diss}^{^{9}Be} = \frac{[^{9}Be]_{reac}}{([^{9}Be]_{reac} + [^{9}Be]_{min})}$$

Eq. 1.2.14

(Eq. 3 from Rahaman et al. 2017)

Despite its utility as a metric of weathering intensity, this single-isotope ^{9}Be system is prone to similar problems as $^{10}Be_{met}$ when it is used alone to calculate weathering rates. Regardless of which of the two equations are used, Wittmann et al. (2015) find consistently higher $f_{reac}^{^{9}Be} + f_{diss}^{^{9}Be}$ when calculated via ^{9}Be concentrations in depth-integrated suspended sediment, compared ^{9}Be from the bed load. This indicates that riverine sorting of sediment introduces more variability to the measured $f_{reac}^{^{9}Be} + f_{diss}^{^{9}Be}$ weathering metric than the assumption of negligible $f_{diss}^{^{9}Be}$.

Section 3: Motivation and hypotheses

In the work I present in the following pages, I evaluate speleothems as new archives of Be isotopes. As groundwater archives, they can potentially provide a time-resolved record of soil ^{10}Be/^{9}Be. This signal may incorporate changes in ^{10}Be flux due to changes in precipitation, geomagnetic field strength, and changes in ^{10}Be and ^{9}Be flux due to changes in dust flux/source, and geomorphic parameters such as erosion and weathering. Deconvolving this signal could lead to a new proxy for weathering rate over time.

Using these groundwater archives as records of the soil $^{10}Be/^{9}Be$ ratio requires a common assumption presented in von Blanckenburg et al. (2012) that, over long time-scales, the $^{10}Be/^{9}Be$ ratio in the dissolved phase is equilibrated and equivalent to the $^{10}Be/^{9}Be$ in the soil reactive phase (incorporated into and/or adsorbed to secondary pedogenic materials). My work offers the opportunity to consider that assumption from a new perspective.

As presented at the beginning of this chapter, my work is motivated by two over-arching questions:

1) What factor(s) is/are dominant in controlling Be isotopes in speleothems?
2) Can Be isotopes in speleothems be used as a metric of weathering rate over time, particularly across glacial/interglacial cycles?

In chapter 2 I discuss measurements I made of $^{10}Be/^{9}Be$ in speleothems from Soreq Cave in Eretz Israel. I discuss similar measurements I conducted on a flowstone from Buffalo Cave in South Africa in Appendix 1. I discuss measurements of $^{10}Be/^{9}Be$ in manganese oxides from the Appalachians in the US in Appendix 2.

I hypothesized that changes in chemical weathering rate would be dominant in controlling the $^{10}Be/^{9}Be$ ratio in the Soreq and Buffalo cave speleothems over glacial/interglacial cycles, but that changes in dust flux and precipitation could influence Be isotopes as well. From a geochemical perspective, I expected that Be isotopes would be delivered to the speleothems via organic and Fe/Mn/Al (hydr)oxide colloids, and therefore, the Be concentrations in the speleothems would co-vary with Fe, Mn, and Al concentrations.

I also hypothesized that the $^{10}Be/^{9}Be$ ratio could be used to date the formation of terrestrial Mn-oxides, but that small differences in the Ar/Ar age and the $^{10}Be/^{9}Be$ age could reflect later, secondary formation of Fe-(hydr)oxides.

Chapter 1 references

Aldahan, A., Haiping, Y., and Possnert, G., 1999, Distribution of beryllium between solution and minerals žbiotite and albite/ under atmospheric conditions and variable pH: , p. 21.

Aldahan, A., and Possnert, G., 2003, Geomagnetic and climatic variability reflected by ^{10}Be during the Quaternary and late Pliocene: GEOMAGNETIC AND CLIMATIC VARIABILITY: Geophysical Research Letters, v. 30, doi:10.1029/2002GL016077.

Bacon, A.R., Richter, D. deB., Bierman, P.R., and Rood, D.H., 2012, Coupling meteoric 10Be with pedogenic losses of 9Be to improve soil residence time estimates on an ancient North American interfluve: Geology, v. 40, p. 847–850, doi:10.1130/G33449.1.

Barg, E., Lal, D., Pavich, M.J., Caffee, M.W., and Southon, J.R., 1997, Beryllium geochemistry in soils: evaluation of 10Be/9Be ratios in authigenic minerals as a basis for age models: Chemical Geology, v. 140, p. 237–258.

Beck, J.W., Zhou, W., Li, C., Wu, Z., White, L., Xian, F., Kong, X., and An, Z., 2018, A 550,000-year record of East Asian monsoon rainfall from ^{10}Be in loess: Science, v. 360, p. 877–881, doi:10.1126/science.aam5825.

Berggren, A.-M., Beer, J., Possnert, G., Aldahan, A., Kubik, P., Christl, M., Johnsen, S.J., Abreu, J., and Vinther, B.M., 2009, A 600-year annual ^{10}Be record from the NGRIP ice core, Greenland: Geophysical Research Letters, v. 36, p. L11801, doi:10.1029/2009GL038004.

Bierman, P.R., Corbett, L.B., Graly, J.A., Neumann, T.A., Lini, A., Crosby, B.T., and Rood, D.H., 2014, Preservation of a Preglacial Landscape Under the Center of the Greenland Ice Sheet: Science, v. 344, p. 402–405, doi:10.1126/science.1249047.

von Blanckenburg, F., Bouchez, J., and Wittmann, H., 2012, Earth surface erosion and weathering from the 10Be (meteoric)/9Be ratio: Earth and Planetary Science Letters, v. 351–352, p. 295–305, doi:10.1016/j.epsl.2012.07.022.

von Blanckenburg, F., O'Nions, R.K., Belshaw, N.S., Gibb, A., and Hein, J.R., 1996, Global distribution of beryllium isotopes in deep ocean water as derived from Fe□Mn crusts: Earth and Planetary Science Letters, v. 141, p. 213–226, doi:10.1016/0012-821X(96)00059-3.

Boschi, V., and Willenbring, J.K., 2016a, Beryllium desorption from minerals and organic ligands over time: Chemical Geology, v. 439, p. 52–58, doi:10.1016/j.chemgeo.2016.06.009.

Boschi, V., and Willenbring, J.K., 2016b, The effect of pH, organic ligand chemistry and mineralogy on the sorption of beryllium over time: Environmental Chemistry, v. 13, p. 711, doi:10.1071/EN15107.

Bourles, D., Raisbeck, G.M., and Yiou, F., 1989, 10Be and 9Be in marine sediments and their potential for dating: Geochimica et Cosmochimica Acta, v. 53, p. 443–452, doi:10.1016/0016-7037(89)90395-5.

Brown, E.T., 1985, The Geochemistry of Beryllium Isotopes: Applications in Geochronometry: Massachusetts Institute of Technology.

Brown, E.T., Edmond, J.M., Raisbeck, G.M., Bourlès, D.L., Yiou, F., and Measures, C.I., 1992, Beryllium isotope geochemistry in tropical river basins: Geochimica et Cosmochimica Acta, v. 56, p. 1607–1624, doi:10.1016/0016-7037(92)90228-B.

Brown, L., Pavich, M.J., Hickman, R.E., Klein, J., and Middleton, R., 1988, Erosion of the eastern United States observed with10Be: Earth Surface Processes and Landforms, v. 13, p. 441–457, doi:10.1002/esp.3290130509.

Carcaillet, J.T., Bourlès, D.L., and Thouveny, N., 2004a, Geomagnetic dipole moment and ^{10} Be production rate intercalibration from authigenic ^{10} Be/ ^{9} Be for the last 1.3 Ma: GEOMAGNETIC DIPOLE MOMENT: Geochemistry, Geophysics, Geosystems, v. 5, p. n/a-n/a, doi:10.1029/2003GC000641.

Carcaillet, J., Bourlès, D.L., Thouveny, N., and Arnold, M., 2004b, A high resolution authigenic 10Be/9Be record of geomagnetic moment variations over the last 300 ka from sedimentary cores of the Portuguese margin: Earth and Planetary Science Letters, v. 219, p. 397–412, doi:10.1016/S0012-821X(03)00702-7.

Castagnoli, G.C. et al., 1995, Evidence for enhanced ^{10} Be deposition in Mediterranean sediments 35 kyr BP: Geophysical Research Letters, v. 22, p. 707–710, doi:10.1029/95GL00298.

Chen, P., Yi, P., Czymzik, M., Aldahan, A., Ljung, K., Yu, Z., Hou, X., Zheng, M., Chen, X., and Possnert, G., 2020, Relationship between precipitation and 10Be and impacts on soil dynamics: CATENA, v. 195, p. 104748, doi:10.1016/j.catena.2020.104748.

Cheng, Z. et al., 2006, Growth ages of ferromanganese crusts from the western and central pacific: Comparison between nannofossil analysis and 10Be dating: Chinese Science Bulletin, v. 51, p. 3035–3040, doi:10.1007/s11434-006-2193-y.

Chmeleff, J., von Blanckenburg, F., Kossert, K., and Jakob, D., 2010a, Determination of the 10Be half-life by multicollector ICP-MS and liquid scintillation counting: Nuclear Instruments and Methods in Physics Research Section B: Beam Interactions with Materials and Atoms, v. 268, p. 192–199, doi:10.1016/j.nimb.2009.09.012.

Chmeleff, J., von Blanckenburg, F., Kossert, K., and Jakob, D., 2010b, Determination of the 10Be half-life by multicollector ICP-MS and liquid scintillation counting: Nuclear Instruments and Methods in Physics Research Section B: Beam Interactions with Materials and Atoms, v. 268, p. 192–199, doi:10.1016/j.nimb.2009.09.012.

Czymzik, M., Muscheler, R., Brauer, A., Adolphi, F., Ott, F., Kienel, U., Dräger, N., Słowiński, M., Aldahan, A., and Possnert, G., 2015, Solar cycles and depositional processes in annual 10 Be from two varved lake sediment records: Earth and Planetary Science Letters, v. 428, p. 44–51, doi:10.1016/j.epsl.2015.07.037.

Dannhaus, N., Wittmann, H., Krám, P., Christl, M., and von Blanckenburg, F., 2018, Catchment-wide weathering and erosion rates of mafic, ultramafic, and granitic rock from cosmogenic meteoric 10Be/9Be ratios: Geochimica et Cosmochimica Acta, v. 222, p. 618–641, doi:10.1016/j.gca.2017.11.005.

Dixon, J.L., Chadwick, O.A., and Pavich, M.J., 2018, Climatically controlled delivery and retention of meteoric 10Be in soils: Geology, v. 46, p. 899–902, doi:10.1130/G45176.1.

Ebert, K., Willenbring, J., Norton, K.P., Hall, A., and Hättestrand, C., 2012, Meteoric 10Be concentrations from saprolite and till in northern Sweden: Implications for glacial erosion and age: Quaternary Geochronology, v. 12, p. 11–22, doi:10.1016/j.quageo.2012.05.005.

Field, C.V., Schmidt, G.A., Koch, D., and Salyk, C., 2006, Modeling production and climate-related impacts on ^{10} Be concentration in ice cores: Journal of Geophysical Research, v. 111, p. D15107, doi:10.1029/2005JD006410.

Frank, M., Rutgers van der Loeff, M.M., Kubik, P.W., and Mangini, A., 2002, Quasi-conservative behaviour of 10Be in deep waters of the Weddell Sea and the Atlantic sector of the Antarctic Circumpolar Current: Earth and Planetary Science Letters, v. 201, p. 171–186, doi:10.1016/S0012-821X(02)00688-X.

Frank, M., Schwarz, B., Baumann, S., Kubik, P.W., Suter, M., and Mangini, A., 1997, A 200 kyr record of cosmogenic radionuclide production rate and geomagnetic field intensity from 10Be in globally stacked deep-sea sediments: Earth and Planetary Science Letters, v. 149, p. 121–129, doi:10.1016/S0012-821X(97)00070-8.

Gosse, J.C., and Phillips, F.M., 2001, Terrestrial in situ cosmogenic nuclides: theory and application: Quaternary Science Reviews, v. 20, p. 1475–1560, doi:10.1016/S0277-3791(00)00171-2.

Graham, I.J., Carter, R.M., Ditchburn, R.G., and Zondervan, A., 2004, Chronostratigraphy of ODP 181, Site 1121 sediment core (Southwest Pacific Ocean), using 10Be/9Be dating of entrapped ferromanganese nodules: Marine Geology, v. 205, p. 227–247, doi:10.1016/S0025-3227(04)00025-8.

Graly, J.A., Bierman, P.R., Reusser, L.J., and Pavich, M.J., 2010, Meteoric 10Be in soil profiles – A global meta-analysis: Geochimica et Cosmochimica Acta, v. 74, p. 6814–6829, doi:10.1016/j.gca.2010.08.036.

Graly, J.A., Corbett, L.B., Bierman, P.R., Lini, A., and Neumann, T.A., 2018, Meteoric 10Be as a tracer of subglacial processes and interglacial surface exposure in Greenland: Quaternary Science Reviews, v. 191, p. 118–131, doi:10.1016/j.quascirev.2018.05.009.

Graly, J.A., Reusser, L.J., and Bierman, P.R., 2011, Short and long-term delivery rates of meteoric 10Be to terrestrial soils: Earth and Planetary Science Letters, v. 302, p. 329–336, doi:10.1016/j.epsl.2010.12.020.

Heikkila, U., Beer, J., and Feichter, J., 2009, Meridional transport and deposition of atmospheric 10Be: Atmos. Chem. Phys., p. 13.

Heikkilä, U., Beer, J., Jouzel, J., Feichter, J., and Kubik, P., 2008, ^{10}Be measured in a GRIP snow pit and modeled using the ECHAM5-HAM general circulation model: Geophysical Research Letters, v. 35, p. L05817, doi:10.1029/2007GL033067.

Helz, G.R., and Valette-Silver, N., 1992, Beryllium-10 in Chesapeake Bay sediments: An indicator of sediment provenance: Estuarine, Coastal and Shelf Science, v. 34, p. 459–469, doi:10.1016/S0272-7714(05)80117-9.

Knies, D.L. et al., 1994, 7Be, 10Be, and 36Cl in precipitation: Nuclear Instruments and Methods in Physics Research, v. B 92, p. 340–344.

Korschinek, G. et al., 2010a, A new value for the half-life of 10Be by Heavy-Ion Elastic Recoil Detection and liquid scintillation counting: Nuclear Instruments and Methods in Physics Research Section B: Beam Interactions with Materials and Atoms, v. 268, p. 187–191, doi:10.1016/j.nimb.2009.09.020.

Korschinek, G. et al., 2010b, A new value for the half-life of 10Be by Heavy-Ion Elastic Recoil Detection and liquid scintillation counting: Nuclear Instruments and Methods in Physics Research Section B: Beam Interactions with Materials and Atoms, v. 268, p. 187–191, doi:10.1016/j.nimb.2009.09.020.

Korte, M., Donadini, F., and Constable, C.G., 2009, Geomagnetic field for 0-3 ka: 2. A new series of time-varying global models: GEOMAGNETIC FIELD FOR 0-3 KA, 2: Geochemistry, Geophysics, Geosystems, v. 10, p. n/a-n/a, doi:10.1029/2008GC002297.

Laj, C., Kissel, C., and Beer, J., 2013, High Resolution Global Paleointensity Stack Since 75 kyr (GLOPIS-75) Calibrated to Absolute Values, *in* Channell, J.E.T., Kent, D.V., Lowrie, W., and Meert, J.G. eds., Geophysical Monograph Series, Washington, D. C., American Geophysical Union, p. 255–265, doi:10.1029/145GM19.

Lal, D., 2007, Recycling of cosmogenic nuclides after their removal from the atmosphere; special case of appreciable transport of 10Be to polar regions by aeolian dust: Earth and Planetary Science Letters, v. 264, p. 177–187, doi:10.1016/j.epsl.2007.09.030.

Lal, D., and Peters, B., 1967, Cosmic Ray Produced Radioactivity on the Earth, *in* Sitte, K. ed., Kosmische Strahlung II / Cosmic Rays II, Berlin, Heidelberg, Springer Berlin Heidelberg, Handbuch der Physik / Encyclopedia of Physics, v. 9 / 46 / 2, doi:10.1007/978-3-642-46079-1.

Lanci, L., Galeotti, S., Grimani, C., and Huber, M., 2020, Evidence against a long-term control on Earth climate by Galactic Cosmic Ray Flux: Global and Planetary Change, v. 185, p. 103095, doi:10.1016/j.gloplacha.2019.103095.

Li, S., Goldstein, S.L., and Raymo, M.E., 2021, Neogene continental denudation and the beryllium conundrum: Proceedings of the National Academy of Sciences, v. 118, p. e2026456118, doi:10.1073/pnas.2026456118.

Lifton, N., Sato, T., and Dunai, T.J., 2014, Scaling in situ cosmogenic nuclide production rates using analytical approximations to atmospheric cosmic-ray fluxes: Earth and Planetary Science Letters, v. 386, p. 149–160, doi:10.1016/j.epsl.2013.10.052.

Lunblad, K., 2006, Studies on Tropical Palaeo-variation in Climate and Cosmic Ray Influx Geochemical data from stalagmites collected in Tanzania and northern South Africa.

Maher, K., and von Blanckenburg, F., 2016, Surface ages and weathering rates from 10Be (meteoric) and 10Be/9Be: Insights from differential mass balance and reactive transport modeling: Chemical Geology, v. 446, p. 70–86, doi:10.1016/j.chemgeo.2016.07.016.

Mangini, A., Segl, M., Kudrass, H., Wiedicke, M., Bonani, G., Hofmann, H.J., Morenzoni, E., Nessi, M., Suter, M., and Wölfli, W., 1986, Diffusion and supply rates of 10Be and 230Th radioisotopes in two manganese encrustations from the South China Sea: Geochimica et Cosmochimica Acta, v. 50, p. 149–156, doi:10.1016/0016-7037(86)90060-8.

Masarik, J., and Beer, J., 2009, An updated simulation of particle fluxes and cosmogenic nuclide production in the Earth's atmosphere: Journal of Geophysical Research, v. 114, p. D11103, doi:10.1029/2008JD010557.

Masarik, J., and Beer, J., 1999, Simulation of particle fluxes and cosmogenic nuclide production in the Earth's atmosphere: Journal of Geophysical Research: Atmospheres, v. 104, p. 12099–12111, doi:10.1029/1998JD200091.

Maurice, P., 2009, Environmental Surfaces and Interfaces from the Nanoscale to the Global Scale: Wiley.

McHargue, L.R., Donahue, D., Damon, P.E., Sonett, C.P., Biddulph, D., and Burr, G., 2000, Geomagnetic modulation of the late Pleistocene cosmic-ray ¯ux as determined by 10Be from Blake Outer Ridge marine sediments: , p. 7.

Miyahara, H., Horiuchi, K., Sakashita, W., Matsuzaki, H., Xu, H., and Zhou, L., 2020, Measurement of beryllium-10 in terrestrial carbonate deposits from South China: A pilot study: Nuclear Instruments and Methods in Physics Research Section B: Beam Interactions with Materials and Atoms, v. 464, p. 36–40, doi:10.1016/j.nimb.2019.11.036.

Moore, A.K., Granger, D.E., and Conyers, G., 2021, Beryllium cycling through deciduous trees and implications for meteoric 10Be systematics: Chemical Geology, v. 571, p. 120174, doi:10.1016/j.chemgeo.2021.120174.

Morris, J., 1991, Applications of cosmogenic 10Be to problems in the earth sciences: Annu. Rev. Earth Planet. Sci., v. 19, p. 313–350.

Muscheler, R., Beer, J., Kubik, P.W., and Synal, H.-A., 2005, Geomagnetic field intensity during the last 60,000 years based on 10Be and 36Cl from the Summit ice cores and 14C: Quaternary Science Reviews, v. 24, p. 1849–1860, doi:10.1016/j.quascirev.2005.01.012.

Nishiizumi, K., Imamura, M., Caffee, M.W., Southon, J.R., Finkel, R.C., and McAninch, J., 2007, Absolute calibration of 10Be AMS standards: Nuclear Instruments and Methods in Physics Research Section B: Beam Interactions with Materials and Atoms, v. 258, p. 403–413, doi:10.1016/j.nimb.2007.01.297.

Norman, E.B., Rech, G.A., Browne, E., Larimer, R.-M., Dragowsky, M.R., Chan, Y.D., Isaac, M.C.P., McDonald, R.J., and Smith, A.R., 2001, Influence of physical and chemical environments on the decay rates of 7Be and 40K: Physics Letters B, v. 519, p. 15–22, doi:10.1016/S0370-2693(01)01097-8.

Oda, H., Usui, A., Miyagi, I., Joshima, M., Weiss, B.P., Shantz, C., Fong, L.E., McBride, K.K., Harder, R., and Baudenbacher, F.J., 2011, Ultrafine-scale magnetostratigraphy of marine ferromanganese crust: Geology, v. 39, p. 227–230, doi:10.1130/G31610.1.

Pedro, J., van Ommen, T., Curran, M., Morgan, V., Smith, A., and McMorrow, A., 2006, Evidence for climate modulation of the ^{10} Be solar activity proxy: Journal of Geophysical Research, v. 111, p. D21105, doi:10.1029/2005JD006764.

Poluianov, S.V., Kovaltsov, G.A., Mishev, A.L., and Usoskin, I.G., 2016, Production of cosmogenic isotopes ^{7} Be, ^{10} Be, ^{14} C, ^{22} Na, and ^{36} Cl in the atmosphere: Altitudinal profiles of yield functions: COSMOGENIC ISOTOPES IN THE ATMOSPHERE: Journal of Geophysical Research: Atmospheres, v. 121, p. 8125–8136, doi:10.1002/2016JD025034.

Porras, R.C., Hicks Pries, C.E., McFarlane, K.J., Hanson, P.J., and Torn, M.S., 2017, Association with pedogenic iron and aluminum: effects on soil organic carbon storage and stability in four temperate forest soils: Biogeochemistry, v. 133, p. 333–345, doi:10.1007/s10533-017-0337-6.

Rahaman, W., Wittmann, H., and von Blanckenburg, F., 2017, Denudation rates and the degree of chemical weathering in the Ganga River basin from ratios of meteoric cosmogenic 10 Be to stable 9 Be: Earth and Planetary Science Letters, v. 469, p. 156–169, doi:10.1016/j.epsl.2017.04.001.

Raisbeck, G.M., Yiou, F., Cattani, O., and Jouzel, J., 2006, 10Be evidence for the Matuyama–Brunhes geomagnetic reversal in the EPICA Dome C ice core: Nature, v. 444, p. 82–84, doi:10.1038/nature05266.

Scherer, R.P., Aldahan, A., Tulaczyk, S., Possnert, G., Engelhardt, H., and Kamb, B., 1998, Pleistocene Collapse of the West Antarctic Ice Sheet: Science, v. 281, p. 82–85, doi:10.1126/science.281.5373.82.

Schiller, M., Dickinson, W., Ditchburn, R.G., Graham, I.J., and Zondervan, A., 2009, Atmospheric ^{10}Be in an Antarctic soil: Implications for climate change: Journal of Geophysical Research, v. 114, p. F01033, doi:10.1029/2008JF001052.

Shen, C.D., Beer, J., Kubik, P.W., Sun, W.D., Liu, T.S., and Liu, K.X., 2010, 10Be in desert sands, falling dust and loess in China: Nuclear Instruments and Methods in Physics Research Section B: Beam Interactions with Materials and Atoms, v. 268, p. 1050–1053, doi:10.1016/j.nimb.2009.10.095.

Singleton, A.A., Schmidt, A.H., Bierman, P.R., Rood, D.H., Neilson, T.B., Greene, E.S., Bower, J.A., and Perdrial, N., 2017, Effects of grain size, mineralogy, and acid-extractable grain coatings on the distribution of the fallout radionuclides 7Be, 10Be, 137Cs, and 210Pb in river sediment: Geochimica et Cosmochimica Acta, v. 197, p. 71–86, doi:10.1016/j.gca.2016.10.007.

Sjunneskog, C., Scherer, R., Aldahan, A., and Possnert, G., 2007, 10Be in glacial marine sediment of the Ross Sea, Antarctica, a potential tracer of depositional environment and sediment chronology: Nuclear Instruments and Methods in Physics Research Section B: Beam Interactions with Materials and Atoms, v. 259, p. 576–583, doi:10.1016/j.nimb.2007.01.203.

Takahashi, Y., Minai, Y., Ambe, S., Makide, Y., and Ambe, F., 1999, Comparison of adsorption behavior of multiple inorganic ions on kaolinite and silica in the presence of humic acid using the multitracer technique: Geochimica et Cosmochimica Acta, v. 63, p. 815–836, doi:10.1016/S0016-7037(99)00065-4.

Valletta, R.D., Willenbring, J.K., Passchier, S., and Elmi, C., 2018, ^{10}Be/ ^{9}Be Ratios Reflect Antarctic Ice Sheet Freshwater Discharge During Pliocene Warming: Paleoceanography and Paleoclimatology, v. 33, p. 934–944, doi:10.1029/2017PA003283.

Vonmoos, M., Beer, J., and Muscheler, R., 2006, Large variations in Holocene solar activity: Constraints from ^{10}Be in the Greenland Ice Core Project ice core: Journal of Geophysical Research, v. 111, p. A10105, doi:10.1029/2005JA011500.

Wagner, G., Masarik, J., Beer, J., Baumgartner, S., Imboden, D., and Kubik, P.W., 2000, Reconstruction of the geomagnetic ®eld between 20 and 60 kyr BP from cosmogenic radionuclides in the GRIP ice core: , p. 8.

Willenbring, J.K., and von Blanckenburg, F., 2010a, Long-term stability of global erosion rates and weathering during late-Cenozoic cooling: Nature, v. 465, p. 211–214, doi:10.1038/nature09044.

Willenbring, J.K., and von Blanckenburg, F., 2010b, Meteoric cosmogenic Beryllium-10 adsorbed to river sediment and soil: Applications for Earth-surface dynamics: Earth-Science Reviews, v. 98, p. 105–122, doi:10.1016/j.earscirev.2009.10.008.

Wittmann, H., von Blanckenburg, F., Bouchez, J., Dannhaus, N., Naumann, R., Christl, M., and Gaillardet, J., 2012, The dependence of meteoric 10Be concentrations on particle size in Amazon River bed sediment and the extraction of reactive 10Be/9Be ratios: Chemical Geology, v. 318–319, p. 126–138, doi:10.1016/j.chemgeo.2012.04.031.

Wittmann, H., von Blanckenburg, F., Dannhaus, N., Bouchez, J., Gaillardet, J., Guyot, J.L., Maurice, L., Roig, H., Filizola, N., and Christl, M., 2015, A test of the cosmogenic ^{10}Be(meteoric)/^{9}Be proxy for simultaneously determining basin-wide erosion rates, denudation rates, and the degree of weathering in the Amazon basin: EROSION FROM METEORIC ^{10}BE/^{9}BE IN AMAZON: Journal of Geophysical Research: Earth Surface, v. 120, p. 2498–2528, doi:10.1002/2015JF003581.

Xu, H., Miyahara, H., Horiuchi, K., Matsuzaki, H., Sun, H., Luo, W., Zheng, X., Suganuma, Y., Wang, S., and Zhou, L., 2019, High-resolution records of 10Be in endogenic travertine from Baishuitai, China: A new proxy record of annual solar activity? Quaternary Science Reviews, v. 216, p. 34–46, doi:10.1016/j.quascirev.2019.05.012.

Yokoyama, Y. et al., 2016, Widespread collapse of the Ross Ice Shelf during the late Holocene: Proceedings of the National Academy of Sciences, v. 113, p. 2354–2359, doi:10.1073/pnas.1516908113.

You, C.-F., Lee, T., and Lp, Y.-H. The partition of Be between soil and water: , p. 14.

Zhou, W., Priller, A., Beck, J.W., Zhengkun, W., Maobai, C., Zhisheng, A., Kutschera, W., Feng, X., Huagui, Y., and Lin, L., 2007, Disentangling Geomagnetic and Precipitation Signals in an 80-kyr Chinese Loess Record of ^{10} Be: Radiocarbon, v. 49, p. 137–158, doi:10.1017/S0033822200041977.

Zhou, W., Warren Beck, J., Kong, X., An, Z., Qiang, X., Wu, Z., Xian, F., and Ao, H., 2014a, Timing of the Brunhes-Matuyama magnetic polarity reversal in Chinese loess using 10Be: Geology, v. 42, p. 467–470, doi:10.1130/G35443.1.

Zhou, W., Xian, F., Du, Y., Kong, X., and Wu, Z., 2014b, The last 130 ka precipitation reconstruction from Chinese loess ^{10} Be: PRECIPITATION RECONSTRUCTION FROM ^{10} Be: Journal of Geophysical Research: Solid Earth, v. 119, p. 191–197, doi:10.1002/2013JB010296.

Ziegler, L.B., Constable, C.G., Johnson, C.L., and Tauxe, L., 2011, PADM2M: a penalized maximum likelihood model of the 0-2 Ma palaeomagnetic axial dipole moment: PADM2M revised: Geophysical Journal International, v. 184, p. 1069–1089, doi:10.1111/j.1365-246X.2010.04905.x.

CHAPTER 2: ^{10}BE/^{9}BE IN SPELEOTHEMS

As groundwater archives of soil and vadose processes, speleothems have the potential to encode information about chemical weathering in the landscape above. Numerous environmental proxies have been explored in speleothems. Widely-applied indicators such as $\delta^{13}C$ and $\delta^{18}O$ record ecosystem change, paleo-precipitation, paleo-temperature, and changes in climate. Other indicators such as trace element concentrations have been used to explore how reactive transport mechanisms in the vadose zone change under different environmental conditions, and to examine how organic colloids from the soil and bedrock (and associated trace-metals) are delivered to speleothems under different environmental and hydrological regimes. The recently developed $\delta^{7}Li$ weathering metric has been used to explore how the chemical weathering of silicate minerals changes in the landscape above the cave over glacial-interglacial cycles (Pogge von Strandmann et al., 2017).

Here I explore the use of $^{10}Be/^{9}Be$ as a novel indicator of chemical weathering. However, in addition to chemical weathering, the environmental $^{10}Be/^{9}Be$ ratio is impacted by a number of factors that I discuss in chapter 1, including changes in atmospheric ^{10}Be production rate, rainfall, dust flux, and erosion rate. However, only one previous study reports the concentrations of Be isotopes in stalactites/stalagmites (Lundblad, 2006), and Be isotopes have never been used to examine weathering rates using a speleothem. As a new and understudied archive of beryllium isotopes, it is unclear at this point which factor(s) are primary in controlling $^{10}Be/^{9}Be$ in speleothems.

The central motives of my work are to (1) reveal the primary factor(s) that controls the $^{10}Be/^{9}Be$ ratio in speleothems, and (2) to assess the utility of the $^{10}Be/^{9}Be$ ratio in speleothems as a metric of chemical weathering rate.

In section 1 of this chapter I discuss the various metrics and indices of chemical weathering, as well as the relationship between chemical weathering and climate. In section 2 I present a new theoretical framework for using $^{10}Be/^{9}Be$ as a metric of chemical weathering. Finally, I present

and discuss Be isotope measurements I made on speleothems from Soreq Cave in Israel, and compare my data to δ^7Li measurements (a metric of weathering congruency) from the same samples analyzed by Pogge von Strandmann et al. (2017). In Appendix 1 I present additional measurements of ^{10}Be/^{9}Be in a flow stone from Buffalo Cave in South Africa.

Section 1: Background – chemical weathering

Weathering is the breakdown of solids near Earth's surface, involving a suite of physical and biogeochemical processes that work in tandem. Chemical weathering causes the loss of primary phases within a rock or parent material, and partitions the mass into three pools:

1) Dissolved ions ***(diss)***
2) Secondary "reactive" materials that are the products of chemical weathering, including amorphous and crystalline phases that are more thermodynamically favored in Earth's near-surface conditions ***(reac)***
3) Remaining parent minerals as a result of incomplete weathering, eventually resulting in highly stable primary minerals from the parent such as quartz ***(min)***

As I discuss in chapter 1, from the perspective of beryllium isotopes in the model of von Blanckenburg et al. (2012), these three pools of weathering products correspond to Be_{diss}, Be_{reac}, and Be_{min} respectively, although these are operationally defined based on how a researcher chemically separates the beryllium. For example, acid leaching or other extraction techniques may not always dissolve all of the secondary phases within sediment, making the separation of Be from the primary (min) and secondary (reac) pools highly dependent on the chosen laboratory procedure.

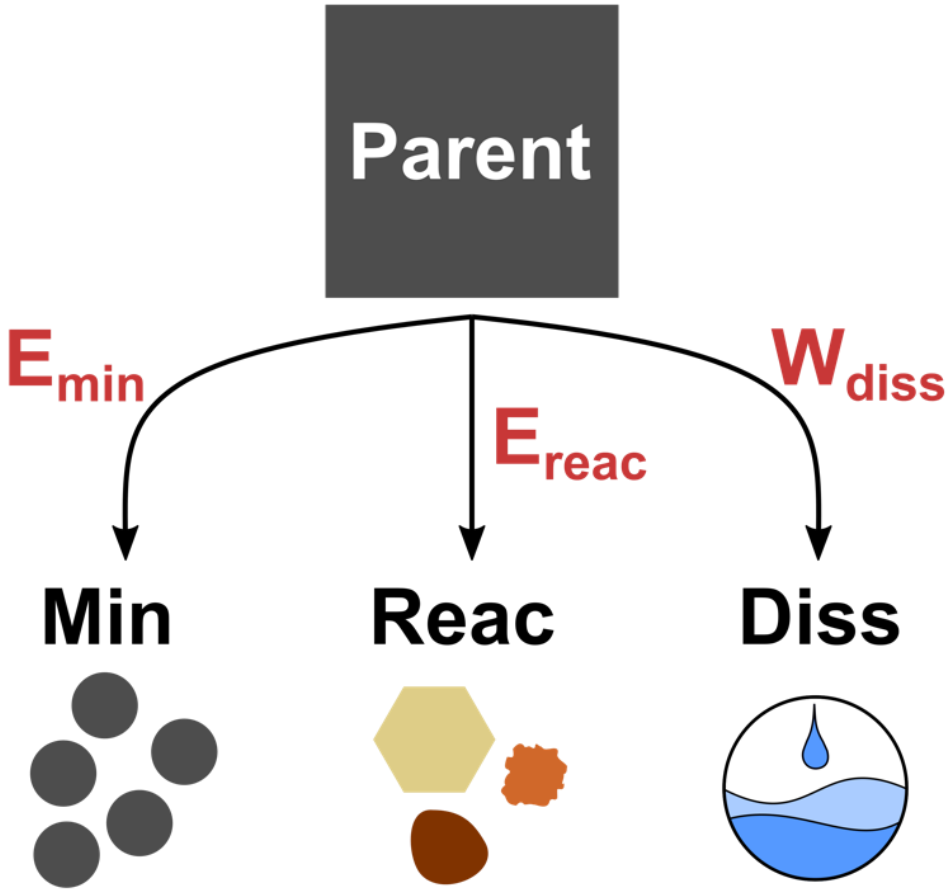

Figure 1: Weathering pools and fluxes

Section 1a: Defining chemical weathering

Chemical weathering is typically gauged in three different ways: weathering rate, congruency, and intensity. I discuss each of these in turn. I also discuss techniques and indices that are used in-practice to examine chemical weathering.

Weathering rate

Chemical weathering rates are typically defined in one of two ways: (1) the chemical erosion rate, which I will refer to as W_{diss}, or (2) the rate of chemical loss of the parent material, which I will refer to as W_p.

The first chemical weathering parameter, the chemical erosion rate (W_{diss}), is the mass loss within the dissolved phase of a given area of land per unit time. This encapsulates only the dissolved pool, and not the "reactive" pool of crystalline and amorphous secondary materials that also form during chemical weathering.

Together, the chemical erosion rate and the total physical erosion rate (E_{tot}) are equivalent to the landscape denudation rate (D), or the total mass loss of a given area per unit time:

$$E_{tot} = E_{min} + E_{reac}$$

(Eq. 2.1.1)

$$D = E_{tot} + W_{diss}$$

(Eq. 2.1.2)

$$W_{diss} = \frac{Q[diss]}{B}$$

(Eq. 2.1.3)

D = Denudation rate (kg m^{-2} yr^{-1})

E = Erosion rates (kg m^{-2} yr^{-1})

W_{diss} = Weathering rate, or chemical erosion rate (kg m^{-2} yr^{-1})

Q = Discharge out of watershed (m^3/yr)

$[diss]$ = Concentration of dissolved species (kg/m^3)

B = Basin area (m^2)

The second way to define chemical weathering is the rate of chemical loss of the parent material. I refer to this as W_p. Unlike the chemical erosion rate, this encapsulates both the dissolved (diss) and "reactive" secondary (reac) pools.

$$W_p = W_{diss} + E_{reac}$$

(Eq. 2.1.4)

In this formulation, the E_{reac} term is the erosion rate of secondary phases. In steady-state (i.e. soil thickness is temporally constant) this is equivalent to the rate of secondary mineral formation.

Weathering congruency

Weathering congruency is the ratio of primary mineral dissolution to secondary mineral formation. When the parent material is entirely dissolved with no solid weathering products the weathering is said to be "congruent," while the production of solid products is said to be "incongruent."

Examples of completely congruent weathering reactions include the dissolution of evaporites and calcite, and the acidic dissolution of kaolinite:

Completely congruent dissolution of halite

$$NaCl \rightarrow Na^{+}_{(aq)} + Cl^{-}_{(aq)}$$

Completely congruent dissolution of calcite

$$CaCO_3 + CO_{2(g)} + H_2O \rightarrow Ca^{2+}_{(aq)} + 2HCO^{-}_{3\ (aq)}$$

Completely congruent dissolution of kaolinite

$$Al_2Si_2O_5(OH)_4 + 6H^{+} \rightarrow 2Al^{3+}_{(aq)} + 2H_4SiO_{4\ (aq)} + H_2O$$

Examples of weathering reactions with mixed-congruency include the formation of kaolinite from anorthite (calcic plagioclase feldspar), and the weathering of kaolinite into gibbsite. These

hydrolysis reactions are common weathering reactions that produce clay minerals, and can have both aqueous and solid products:

Formation of kaolinite and dissolved Ca from the weathering of anorthite

$$CaAl_2Si_2O_8 + H_2O + 2H^+ \rightarrow Al_2Si_2O_5(OH)_4 + Ca^{2+}_{(aq)}$$

Formation of gibbsite and dissolved orthosilicic acid from the weathering of kaolinite

$$Al_2Si_2O_5(OH)_4 + 5H_2O \rightarrow 2Al(OH)_3 + 2H_4SiO_{4(aq)}$$

Weathering congruency describes the partitioning of chemical weathering products into the dissolved (W_{diss}) and reactive (E_{reac}) pools. Therefore, congruency links the two definitions of weathering above, W_{diss} and W_p.

Weathering intensity

Weathering intensity is the fraction of denudation that is accomplished chemically. It is related to the chemical erosion rate (W_{diss}) by the following relationship:

$$Weathering\ Intensity = \frac{W_{diss}}{D} = \frac{W_{diss}}{W_{diss}+E_{tot}}$$

(Eq. 2.1.5)

Gauging weathering in-practice

Chemical weathering rates are different for each element. Aluminum is one of the most recalcitrant elements in the weathering environment, and therefore tends to accumulate in the residuum relative to other elements. One method of gauging the degree of chemical weathering of silicate rocks is the chemical index of alteration (CIA). In order to measure CIA, elemental concentrations are measured in the residuum.

$$CIA = \frac{Al_2O_3}{Al_2O_3 + CaO^* + Na_2O + K_2O} \times 100$$

(Eq. 2.1.6)

(Eq. 1 from Nesbitt & Young, 1982)

CaO^* = Calcium oxide derived from silicates (corrected for carbonate and apatite content)

Alternatively, degree of chemical weathering can be gauged via comparison of immobile-element concentrations between the parent material and the residuum using the chemical depletion fraction (CDF):

$$CDF = 1 - \frac{C_{i,p}}{C_{i,w}}$$

(Eq. 2.1.7)

(Eq. from Riebe et al. 2001)

$C_{i,p}$ = Concentration of immobile element i in the parent material

$C_{i,w}$ = Concentration of immobile element i in the weathered material

During steady-state weathering and erosion, the CDF is related to denudation (D), erosion (E), and chemical weathering (W) by the following relationship (using zirconium as the immobile element):

$$W = D - E = D\left(1 - \frac{[Zr]_{rock}}{[Zr]_{soil}}\right)$$

(Eq. 2.1.8)

(Eq. 1 from Riebe et al. 2004)

Rearranging this equation indicates that in steady-state conditions the CDF is a metric of weathering intensity (W/D):

$$Weathering\ Intensity = \frac{W}{D} = \left(1 - \frac{[Zr]_{rock}}{[Zr]_{soil}}\right) = CDF$$

(Eq. 2.1.9)

(Eq. 2 from Riebe et al. 2004)

Element-specific chemical weathering can also be evaluated. The relative mass loss metric (τ) compares concentrations of immobile and mobile elements in the parent material and weathered material:

$$\tau = \frac{C_{j,soil}}{C_{j,rock}} \frac{[Zr]_{rock}}{[Zr]_{soil}} - 1$$

(Eq. 2.1.10)

(Eq. 3 from Dixon et al. 2012)

$C_{j,soil}$ = Concentration of mobile element j in the soil

$C_{j,rock}$ = Concentration of mobile element j in the parent rock

Section 1b: Weathering congruency from δ^7Li

Stable isotopes of lithium and other elements undergo varying extents of kinetic and equilibrium isotopic fractionation during chemical reactions. Like other stable isotope systems, the lithium isotope ratio is reported based on *per-mil* (‰) deviation from a standard (NIST-8454 LSVEC standard for Li):

$$\delta\,^7Li = \left[\frac{\left(\frac{^7Li}{^6Li}\right)_{sample} - \left(\frac{^7Li}{^6Li}\right)_{standard}}{\left(\frac{^7Li}{^6Li}\right)_{standard}} \right] \times\ 1000\ ‰$$

(Eq. 2.1.11)

The vast majority of lithium in the weathering environment derives from silicates. Lithium concentration in the upper continental crust averages 30.5 ±3.6 µg/g, however, the concentration

of lithium in silicate minerals is typically several orders of magnitude higher than in carbonates (Pogge von Strandmann et al., 2020). The δ^7Li values in continental crust range from -10‰ to +10‰. In contrast, fractionation due to clay production causes δ^7Li in surface waters to range from 2‰ to 43‰ (Pogge von Strandmann et al., 2020).

Laboratory and field studies report no measured fractionation of Li isotopes during mineral dissolution. However, there is wide observation of fractionation during the precipitation of secondary minerals. Li & Liu (2020) observe 36‰ fractionation during laboratory precipitation of kaolinite, and find dominance of kinetic mechanisms of fractionation over equilibrium mechanisms.

These properties make δ^7Li a useful metric of silicate weathering congruency – the ratio of primary silicate mineral dissolution to secondary mineral formation. When silicates weather to clay minerals, ^{6}Li is preferentially incorporated into the clay compared to ^{7}Li. Thus, during periods of low weathering congruency (higher relative rates of clay production), δ^7Li goes up in the dissolved phase, and goes down in the clay minerals.

Section 1c: Kinetics of chemical weathering

Mineral dissolution rate can be either transport-controlled or surface-controlled (Maurice, 2009). In transport-controlled dissolution, the weathering rate is said to be either *transport-limited* or *supply-limited*. In a transport-limited environment, the export rate of reaction products limits dissolution. For instance, if water leaves the weathering zone at a slow rate, the water can become saturated with solutes. As a result, mineral dissolution rates are governed by solubility and water flow rate. On the other hand, in a supply limited environment the supply rate of weathering minerals controls the weathering rate. For example, in a landscape where the weathering minerals are supplied by dust, the dust flux may dictate weathering rate if the dust flux is very low, or if erosion rates are very low then the fresh mineral supply from bedrock can be low.

In contrast, during surface-controlled dissolution, the rate limiting step is at the mineral surface since reaction products do not accumulate, and mineral supply is not limiting. Thus, the rate of

dissolution is said to be *kinetically limited*. For instance, the weathering rate of granite in a watershed could depend on temperature. In the case of surface-controlled weathering, kinetics describes the following relationship for the rate of dissolution of a specific mineral, given steady-state dissolution:

$$R_d = \frac{dC}{dt} = ka$$

(Eq. 2.1.12)

(Eq. 1.88 from Maurice, 2009)

R_d = Rate of dissolution (mol/s)

C = Concentration of product

t = Time

a = surface area of mineral (m^2)

k = Rate constant (mol m^{-2} s^{-1})

As seen in this rate-law, the rate of primary mineral loss can be impacted by a change in either the rate constant (via change in parameters that impact reaction kinetics), or by change in the mineral surface area.

Transition state theory (TST) is a common approach to modeling surface-controlled dissolution. TST posits that a reaction pathway contains an intermediary configuration of atoms or molecules known as the "activated complex" or "transition state." The activation energy of the total reaction is approximately equivalent to the difference in energy between the initial configuration and the arrangement in the activated complex. TST assumes that the activated complex forms in equilibrium with the initial reactants.

The rate constant for a chemical reaction can be related to temperature via the Arrhenius equation:

$$k = Ae^{-\frac{E_a}{RT}}$$

(Eq. 2.1.13)

k = Rate constant

E_a = Activation energy of reaction (J/mol)

R = Ideal gas constant (~8.314 J mol^{-1} K^{-1})

T = Temperature (K)

A = Constant derived empirically or from theory

Numerous other variables can impact the kinetics of chemical weathering beyond temperature. Lasaga (1995) scales the rate of mineral dissolution based on temperature, pH, reactive surface area of the mineral, and ionic strength:

$$Rate = k_{\circ}\, a_{min}\, e^{\frac{-E_a}{RT}}\, X_{H^+,ads}^{n_{H^+,ads}}\, g(I) \prod_i X_{i,ads}^{n_i}\, f(\Delta G_r)$$

(Eq. 2.1.14)

(Eq. 4 from Lasaga, 1995)

$k_{\circ}$ = Intensive rate constant (mol cm^{-2} s^{-1})

a_{min} = Reactive surface area of mineral; the surface area involved in the reaction (cm^2)

E_a = The activation energy of the reaction

R = Ideal gas constant

T = Temperature (K)

$g(I)$ = Effect of ionic strength (I)

$X_{H^+,ads}^{n_{H^+,ads}}$ = Mole fraction of H^+ at the mineral surface

$X_{i,ads}^{n_i}$ = Mole fraction of species i at the mineral surface

$f(\Delta G_r)$ = Variation of rate with deviation from equilibrium (ΔG_r = 0 at equilibrium)

This demonstrates that the constant 'A' in the Arrhenius equation any embody any number of variables. If these variables vary with temperature, they can attenuate or exaggerate the apparent

relationship between temperature and reaction rate. In a landscape, many variables such as rainfall or mineral reactive surface area can impact weathering rates, and can also vary with temperature across glacial/interglacial cycles.

Section 1d: Chemical weathering and climate

The carbonate-silicate cycle

On the modern Earth, the inorganic carbon cycle (also known as the carbonate-silicate cycle) exerts primary control on long-term atmospheric CO_2 concentrations. By limiting large fluctuations in atmospheric CO_2 the carbonate-silicate cycle prevents Earth from reaching unhabitable extremes (Kasting, 2019). This cycle can be simplified to the following reactions:

$$CaSiO_3 + CO_2 \leftrightarrow CaCO_3 + SiO_2$$
$$MgSiO_3 + CO_2 \leftrightarrow MgCO_3 + SiO_2$$

Inorganic degassing of CO_2 occurs when the reaction is driven to the left. This happens at locations such as island arcs, midocean ridges, continental arcs, and zones of carbonate metamorphism. Alternatively, chemical weathering processes at Earth's surface push the reaction to the right. Atmospheric CO_2 dissolves in water as carbonic acid (H_2CO_3). This acidity helps drive chemical weathering reactions that break down silicate minerals. The dissolved calcium and magnesium are delivered to ocean basins where they precipitate as carbonates, thus taking CO_2 from the atmosphere and sequestering it in the lithosphere. This mechanism is thought to be a stabilizing influence on Earth's climate over periods of hundreds of millions of years.

Relationship between climate and chemical weathering reactions

Historically, elevated global chemical weathering *flux* was viewed as the mechanism that drives cooling. Early researchers proposed that cooling is accomplished by heightened *rates* of silicate weathering reactions during warm times (Walker & Hays, 1981). This was an intuitive hypothesis since the rate constants (k) of weathering reactions scale with temperature via the

relationship outlined by the Arrhenius equation (as discussed in section 1c) and with other parameters such as pH and ionic strength.

In addition to the temperature-dependent rate constant (k) of a weathering reaction, the weathering flux (R_d in Eq. 2.1.12) is also impacted by the total mineral surface area (a), which depends on the rate of sediment supply by erosion and comminution.

It was suggested that increased erosion rates during the Neogene led to increased weathering flux, thereby leading to global cooling (Raymo & Ruddiman, 1992; Peizhen & Molnar, 2001). However, the $^{10}Be/^{9}Be$ ratio in marine sedimentary records shows no change for the past ~13 million years (Willenbring & von Blanckenburg, 2010). This implies that there has been a stable chemical weathering flux and rate on the global scale throughout Neogene cooling. This has led to two inter-related conundrums: how does the global chemical weathering rate remain constant, even while physical erosion rates are increasing, and how does the chemical weathering flux remain constant while global temperature and atmospheric CO_2 concentration are decreasing?

Hypothesis 1: change in global reactive surface area counterbalances change in kinetics

Several hypotheses have been proposed that attempt to explain how the global chemical weathering flux could remain stable over glacial/interglacial cycles. A stable weathering flux could theoretically occur if the changes in the rate constants of weathering reactions and the reactive surface area of minerals counterbalance one another. For example, during a period of cooling, the rate constants of weathering reactions could decrease, but the global reactive surface area of primary minerals could increase.

One proposed mechanism that could increase the global reactive mineral surface area is glacial processes (which grind up bedrock and provide an abundance of primary minerals). Another proposed mechanism is sea-level drop. Exposure of the continental shelves during glacial intervals could balance out the lowered continental weathering flux in the marine record (Frings, 2019; Foster & Vance, 2006).

Alternatively, modulation of erosion rate could alter the thickness of regolith, thus changing surface area. Gabet & Mudd (2009) model chemical weathering in the Himalayas and demonstrate that weathering rate can be stable or even decline while erosion rates increase. They postulate that high erosion rates can produce thinner regolith (and therefore less reactive mineral surface area), thus offsetting changes in weathering kinetics.

Hypothesis 2: change in efficiency of CO_2-drawdown by change in weathering intensity

These examples illustrate a variety of mechanisms by which the global weathering flux could remain constant. However, none of these hypotheses directly explain how the global capacity of CO_2-drawdown can change while global chemical weathering flux is stable. The carbonate-silicate cycle must be balanced with respect to alkalinity (i.e. Ca^{2+} and Mg^{2+}) and CO_2. A viable hypothesis must explain a stable weathering flux and rate, an increasing erosion rate, and a declining weathering intensity (or CDF) during cooling.

Additional information on global weathering comes from δ^7Li in marine records. Counter to the long-term stability of the $^{10}Be/^{9}Be$ weathering flux record, the δ^7Li shows a long-term trend towards more incongruent weathering towards the present over the Neogene. This is interpreted as a decrease in silicate weathering intensity as climate cooled (Caves Rugenstein et al., 2019).

A field-based example of the interplay between physical erosion and chemical weathering by Schachtman et al. (2019) examined a core from Little Lake, Oregon, and inferred weathering intensity from CDF and physical erosion rates from *in situ* ^{10}Be in quartz over a glacial-interglacial cycle. They found that erosion rates were higher during colder periods, likely due to frost-cracking processes, but that weathering was less intense (low CDF). The negative correlation between physical erosion and chemical weathering intensity led to a balance, in which the total weathering flux from the watershed remained constant, even while both physical erosion and weathering intensity both changed. If this relationship between CDF and physical erosion rates holds over a broader area of the globe, it could help explain why weathering fluxes remain constant even in the face of increasing erosion and global cooling.

Concordant with this finding, Caves et al. (2016) postulate that global cooling during the Neogene could have been accomplished with no change in the global weathering flux if the *efficiency* of CO_2 drawdown in weathering reactions increased due to an abundance of fresh, reactive Ca- and Mg-bearing silicate mineral surfaces. Mathematically Caves et al. (2016) express this by a change in the constant of proportionality (k in the equation below) between silicate weathering flux and CO_2-drawdown.

$$F_{silw} = \left(\frac{E}{E0}\right)^{asil} k^{*}\left[log_2\left(R_{CO_2}\right) + 1\right]$$

$$R_{CO_2} = \frac{(PCO_2)_t}{(PCO_2)_{modern}}$$

(Eq. 2.1.15 & 2.1.16)

(Eq. 1 from Caves Rugenstein et al. 2019; Caves et al. 2016)

k^{*} = Constant of proportionality relating silicate weathering to atmospheric CO_2 drawdown

F_{silw} = Silicate weathering flux

$(PCO_2)_t$ = The partial pressure of CO_2 in the atmosphere at time t

$(PCO_2)_{modern}$ = The partial pressure of CO_2 in the modern atmosphere

asil = Allows for non-linear relationship between erosion and weathering (empirically calibrated to 0.55 in the model)

Caves et al. (2016) relate changes in temperature and PCO_2 in the atmosphere via an empirical relationship from Knutti & Hegerl (2008):

$$\Delta T = \frac{S\, ln(R_{CO_2})}{ln\,(2)}$$

$$S = \Delta T_{2\times CO_2}$$

(Eq. 2.1.17 & 2.1.18)

(Eq 2 from Knutti & Hegerl, 2008)

ΔT = Change in temperature

$\Delta T_{2\times CO_2}$ = A change in temperature given a doubling of atmospheric CO_2 partial pressure

In the formulations above, because the exponent asil is <1, an increase in erosion rates results in a decrease in weathering intensity (i.e., erosion rates increase faster than weathering rates, so a smaller proportion of total denudation is accomplished by chemical weathering). In order to maintain a constant silicate weathering flux as constrained by the $^{10}Be/^{9}Be$ record, a decrease in atmospheric CO_2 should be accompanied by an increase in erosion rates and a concomitant decrease in weathering intensity. Rugenstein et al. (2019) were able to reconcile global cooling, increased erosion rates, stable weathering flux, and decreasing weathering congruency over the Neogene.

Another way to look at this problem is to consider that, for chemical weathering to be more efficient at drawing down CO_2 during cooling, chemical weathering must also be more efficient in the production of Ca^{2+} and Mg^{2+} concentrations required to produce carbonate minerals. In other words, more calcium and magnesium must be released per gram of primary minerals dissolved. During cold times, higher erosion rates (in regions that are impacted by glacial processes) means that primary minerals spend less time in the weathering zone of the regolith. As a result, chemical weathering is more incomplete, thus yielding more Ca^{2+} and Mg^{2+} since calcium- and magnesium-bearing minerals are likely to be the first minerals to weather. This is supported by the finding of lower weathering intensity (or CDF) during glacial intervals (Schachtman et al., 2019; Caves Rugenstein et al., 2019).

<u>Hypothesis 3: the $^{10}Be/^{9}Be$ ratio in the marine record does not accurately record weathering rates</u>

In contrast to the hypotheses discussed above, Li et al. (2021) argue that the observed stability of $^{10}Be/^{9}Be$ in the marine record across the Neogene is not the result of a stable global weathering rate or flux. Rather, they propose that the marine beryllium isotope ratio is stabilized across glacial/interglacial cycles due to modulation of the degree of coastal scavenging of beryllium. Thus, they argue that global chemical weathering rate and flux should increase during interglacial times, and decrease during glacial intervals.

Speleothems as terrestrial archives of chemical weathering rates

δ^7Li measured in speleothems from Soreq and Tzavoa Caves (0-200 ka) in Israel show a local decrease in weathering intensity and weathering congruency during glacial times (Pogge von Strandmann et al., 2017), the same trend identified in marine records. The motive for my work was to extend the ^{10}Be/^{9}Be weathering proxy to speleothems for comparison with the δ^7Li data measured by Pogge von Strandmann et al. (2017). I worked with some of the same samples from Soreq cave, allowing direct comparison of these two metrics in speleothems for the first time.

Employing beryllium isotopes in speleothems as a weathering metric could offer a new opportunity to examine how weathering rates have varied in a landscape over time. Evaluating the extent to which weathering rates have changed across glacial/interglacial cycles in a variety of settings could shed light on these three hypotheses.

Section 2: *Developing a theoretical framework for a ^{10}Be/^{9}Be weathering rate metric*

Here I discuss novel ways that beryllium isotopes could be used to quantify chemical weathering rates. Additional details regarding the derivations outlined in this section are in Appendix 3.

The equations that I derive in the following discussions ultimately stem from three equations presented in von Blanckenburg et al. (2012). The first is based on the continuity equation, assuming steady-state denudation.

$$D\left[{}^{9}Be\right]_{p} = E\left\{\left[{}^{9}Be\right]_{min} + \left[{}^{9}Be\right]_{reac}\right\} + Q\left[{}^{9}Be\right]_{diss}$$

(Eq. 2.2.1)

(Eq. 5 from von Blanckenburg et al. 2012)

The second equation assumes that beryllium in the reactive phase of the soil is equilibrated with the dissolved phase leaving the soil/bedrock column via a partition coefficient, K_d. It also assumes that K_d is the same for both ^{10}Be and ^{9}Be. Typically, kinetic and equilibrium isotopic fractionation of other elements occurs on the permil level. Therefore, the assumption of uniform K_d between both Be isotopes is a sound assumption within the percent-level uncertainty of ^{9}Be measurements.

$$\boldsymbol{K_d} = \frac{[Be]_{\boldsymbol{reac}}}{[Be]_{\boldsymbol{diss}}}$$

(Eq. 2.2.2)

(Eq. 2 from von Blankenburg et al. 2012)

The third equation assumes that the flux of $^{10}Be_{met}$ into the soil system is equal to the flux out (i.e., steady-state and no radioactive decay).

$$\frac{\boldsymbol{Q}}{\boldsymbol{K_d}} = \frac{F_{met}^{^{10}Be}}{[^{10}Be]_{reac}} - \boldsymbol{E}$$

(Eq. 2.2.3)

(Eq. 3 from von Blankenburg et al. 2012)

By combining the equations above, the following relationship can be established:

$$D[\,^{9}Be]_{p} = E\left\{[\,^{9}Be]_{min} + [\,^{9}Be]_{reac}\right\} + \frac{[\,^{9}Be]_{reac}}{[^{10}Be]_{reac}} F_{met}^{^{10}Be} - E[\,^{9}Be]_{reac}$$

(Eq. 2.2.4)

which simplifies to:

$$D[\,^{9}Be]_{p} = E[\,^{9}Be]_{min} + \frac{[\,^{9}Be]_{reac}}{[^{10}Be]_{reac}} F_{met}^{^{10}Be}$$

(Eq. 2.2.5)

At first glance, it is apparent from this equation that a measured $^{10}Be/^{9}Be$ ratio contains information about chemical weathering. If we were to assume that the $\left[{}^{9}Be \right]_{\boldsymbol{p}}$ term and the $\left[{}^{9}Be \right]_{\boldsymbol{min}}$ term were equivalent, then we could explicitly subtract D-E, which is equivalent to the weathering rate W_{diss}. However, this assumption cannot be made for several reasons. First, the $\left[{}^{9}Be \right]_{\boldsymbol{p}}$ term is in units of atoms of ^{9}Be per gram of parent material, while the $\left[{}^{9}Be \right]_{\boldsymbol{min}}$ term is in units of atoms of ^{9}Be in the mineral pool per gram of total sediment or soil. Second, because the parent material may contain a variety of minerals, each with separate weathering rates and beryllium concentrations, the mineralogical proportions and ^{9}Be concentration within the parent material may be very different from the 'min' pool. For instance, if the parent material is composed of feldspar and quartz, the feldspar/quartz ratio is likely to decrease in the 'min' pool due to the difference in their chemical weathering rates. Likewise, since feldspar commonly has a higher ^{9}Be concentration than quartz, $\left[{}^{9}Be \right]_{\boldsymbol{min}}$ is likely to be lower than $\left[{}^{9}Be \right]_{\boldsymbol{p}}$.

<u>Calculating total weathering rate, assuming homogenous ^{9}Be concentration in the parent material</u>

First I will derive a weathering equation that assumes a homogeneous ^{9}Be concentration within the parent material. Then I will derive equations for more complicated, heterogeneous systems.

The mineral (min), and reactive (reac) geochemical pools are operationally defined based on the chemical extraction procedure employed to isolate beryllium. In some cases, the "min" pool could be viewed as a mixture of residual primary minerals and unreactive secondary phases that do not equilibrate with the reactive pool.

However, for the purpose of developing a weathering metric, I will assume that the "min" pool is only composed of residual primary minerals from the parent material. Therefore I will also assume that the "reac" pool is exclusively composed of secondary phases, all of which are reactive and therefore isotopically equilibrate with respect to $^{10}Be/^{9}Be$ over the timescale of beryllium residence in the weathering zone. This means that there is "open-system" behavior between the reactive and dissolved phases. Finally, I will assume that the sediment is entirely composed of the "min" and "reac" pools:

$$1 = \gamma_{min} + \gamma_{reac}$$

(Eq. 2.2.6)

γ_{min} = Fraction of the sediment that is primary mineral phases

γ_{reac} = Fraction of the sediment that is secondary reactive phases

The way von Blanckenburg et al. (2012) define $[^9Be]_{min}$ and $[^9Be]_{reac}$ is per gram of total sediment. The concentration of beryllium within the mineral pool per gram of mineral material is therefore:

$$[\,^9Be]_{min'} = \frac{[\,^9Be]_{min}}{\gamma_{min}}$$

(Eq. 2.2.7)

$[\,^9Be]_{min}$ = atoms of ^{9}Be in the mineral pool / g total sediment (von Blanckenburg et al., 2012)

$[\,^9Be]_{min'}$ = atoms of ^{9}Be in the mineral pool / g of mineral material

Likewise, the concentration of beryllium within the reactive pool per gram of reactive material is therefore:

$$[\,^9Be]_{reac'} = \frac{[\,^9Be]_{reac}}{\gamma_{reac}}$$

(Eq. 2.2.8)

$[\,^9Be]_{reac}$ = atoms of ^{9}Be in the reactive pool / g total sediment (von Blanckenburg et al., 2012)

$[\,^9Be]_{reac'}$ = atoms of ^{9}Be in the reactive pool / g of mineral material

Thus, we can re-write eq. 2.2.5 from the previous section (derived from von Blanckenburg et al., 2012) as:

$$D\left[\,^9Be\right]_p = E\,\gamma_{min}\left[\,^9Be\right]_{min'} + \frac{\left[\,^9Be\right]_{reac}}{\left[^{10}Be\right]_{reac}} F_{met}^{^{10}Be}$$

(Eq. 2.2.9)

If the parent material has homogenous ^{9}Be concentration, then we can assume that the concentration of beryllium within the mineral phase is equivalent to the concentration of beryllium within the parent:

Assuming $[\,^{9}Be]_{min'} = [\,^{9}Be]_{p}$

(Eq. 2.2.10)

This assumption would not be justified if there was not homogeneous distribution of ^{9}Be among phases within the parent, since differences in weathering and erosion rates of each phase would cause differences in ^{9}Be concentration between the mineral pool and the parent material. I discuss various examples of complex parent materials in the following subsections.

Given this assumption, we can rewrite equation 2.2.9 as:

$$D\left[\,^{9}Be\right]_{min'} = E\,\gamma_{min}\left[\,^{9}Be\right]_{min'} + \frac{\left[\,^{9}Be\right]_{reac}}{\left[^{10}Be\right]_{reac}} F_{met}^{^{10}Be}$$

(Eq. 2.2.11)

Rearranging this equation, we can arrive at

$$\frac{\left[^{10}Be\right]_{reac}}{\left[\,^{9}Be\right]_{reac}} = \frac{F_{met}^{^{10}Be}}{\left[\,^{9}Be\right]_{min'}(D - E\,\gamma_{min})}$$

(Eq. 2.2.12)

which is equivalent to:

$$\frac{\left[^{10}Be\right]_{reac}}{\left[\,^{9}Be\right]_{reac}} = \frac{F_{met}^{^{10}Be}}{\left[\,^{9}Be\right]_{min'}(D - E + E\,\gamma_{reac})}$$

(Eq. 2.2.13)

The D-E term is equivalent to the chemical denudation rate (W_{diss}), since

$D = E_{min} + E_{reac} + W_{diss}$:

$$\frac{[^{10}Be]_{reac}}{[^{9}Be]_{reac}} = \frac{F_{met}^{^{10}Be}}{[^{9}Be]_{min'}(W_{diss}+E\,\gamma_{reac})}$$

(Eq. 2.2.14)

Recalling definitions I provide in section 1a of this chapter, the term $W_{diss} + E\,\gamma_{reac}$ in the denominator is equivalent to the weathering rate of the parent (W_p), since $E\,\gamma_{reac}$ is equal to the erosion rate of reactive phases (E_{reac}), which in steady-state is equivalent to the rate of reactive phase formation:

$$E_{tot} = E_{min} + E_{reac}$$

(Eq. 2.2.15)

$$E\,\gamma_{reac} = E_{reac}$$

(Eq. 2.2.16)

Therefore, the equation simplifies to:

$$\frac{[^{10}Be]_{reac}}{[^{9}Be]_{reac}} = \frac{F_{met}^{^{10}Be}}{[^{9}Be]_{min'}(W_{diss}+E_{reac})}$$

(Eq. 2.2.17)

Together, W_{diss} and E_{reac} are equivalent to the weathering rate of the parent (W_p), which encompasses both the dissolved weathering flux, as well as the eroding secondary phases:

$$W_p = W_{diss} + E_{reac}$$

(Eq. 2.2.18)

Therefore, the equation can be further simplified to:

$$\frac{[^{10}Be]_{reac}}{[^{9}Be]_{reac}} = \frac{F_{met}^{^{10}Be}}{[^{9}Be]_{min'}(W_p)}$$

(Eq. 2.2.19)

However, in order to solve for the chemical denudation rate (W_{diss}), one needs to either know the erosion rate of reactive phases (E_{reac}), or the total erosion rate (E_{tot}) as well as the fraction of the sediment leaving the watershed that is reactive phases (γ_{reac}). These could be difficult to determine. Both the γ_{reac} and E_{reac} parameters are directly related to weathering congruency. If we define weathering congruency, C, as the fraction of chemical weathering accomplished in the dissolved phase, then:

$$C = \frac{W_{diss}}{W_{diss}+E_{reac}}$$

(Eq. 2.2.20)

This definition of weathering congruency is useful since it varies between zero (entirely incongruent weathering) and one (entirely congruent weathering). Based on this definition of weathering congruency, the weathering equation can be rewritten as:

$$\frac{[^{10}Be]_{\boldsymbol{reac}}}{[^{9}Be]_{\boldsymbol{reac}}} = \frac{F_{met}^{^{10}Be}}{[^{9}Be]_{min'}\frac{W_{diss}}{C}}$$

(Eq. 2.2.21)

The weathering equation that I derive above assumes that the parent has a homogeneous concentration of beryllium. Given this assumption the $[\,^{9}Be]_{min'}$ term in the denominator could be interchangeably replaced by $[\,^{9}Be]_{p}$.

These equations demonstrate that, at least in this simplistic model, the chemical erosion rate (W_{diss}) can be determined from a measurement of $^{10}Be/^{9}Be$ if the concentration of ^{9}Be in the mineral phase or parent material, the weathering congruency, and the meteoric ^{10}Be flux can all

be independently determined. Without weathering congruency, the total weathering rate of the parent (W_p) could still be determined. Additionally, if both the values of W_p and weathering congruency are known, the rate of secondary mineral formation (E_{reac}) can also be determined.

Weathering rates with multiple pools of ^{9}Be within the parent material

A uniform Be concentration in the parent material is unlikely, given that beryllium is known to partition into certain minerals. If there are a number of phases within the parent material that have different ^{9}Be concentrations, then the measured $^{10}Be/^{9}Be$ ratio represents the sum of the W_p weathering rates of each phase in the parent material, weighted by their ^{9}Be concentrations:

$$\frac{[^{10}Be]_{reac}}{[^{9}Be]_{reac}} = \frac{F_{met}^{^{10}Be}}{\sum_{x=1}^{n}[^{9}Be]_x W_{p,x}}$$

(Eq. 2.2.22)

n = Number of phases in the parent material

$[^{9}Be]_x$ = Concentration of ^{9}Be in phase x

$W_{p,x}$ = Weathering rate of phase x

Details of the derivation of this equation are outlined in Appendix 3.

If a phase "x" does not contain ^{9}Be (i.e., $[^{9}Be]_x = 0$), or if a phase does not chemically weather (i.e., $W_{p,x} = 0$), then that phase will drop out of the equation. For example, if the parent material was composed of only quartz and feldspar, a total W_p could still be determined since quartz typically has a relatively negligible ^{9}Be concentration, and since the quartz chemical weathering rate is likely to be negligible while feldspar still remains in the weathering zone.

Like in the previous subsection, the phase-specific W_p terms can also be re-written if we define phase-specific weathering congruencies:

$$C_x = \frac{W_{diss,x}}{W_{diss,x}+E_{reac,x}}$$

(Eq. 2.2.23)

C_x = Weathering congruency of phase x from the parent

$W_{diss,x}$ = Weathering rate (chemical erosion rate) of phase x

$E_{reac,x}$ = Erosion rate of reactive phases produced from chemical weathering of phase x in the parent. In steady-state, this is equivalent to the rate of secondary phase formation from parent phase x.

$$\frac{[^{10}Be]_{reac}}{[^{9}Be]_{reac}} = \frac{F_{met}^{^{10}Be}}{\sum_{x=1}^{n}[^{9}Be]_x \frac{W_{diss,x}}{C_x}}$$

(Eq. 2.2.24)

<u>Weathering rates with dust as the parent material, and no addition from bedrock</u>

As I discuss below, a terra rossa soil overlies our field-site at Soreq Cave. This soil is derived from allochthonous dust (containing silicates, clays, and carbonates), rather than the underlying carbonate bedrock. In this case, the incoming dust contributes reactive phases that already contain beryllium with their own $^{10}Be/^{9}Be$ ratio.

Here I derive a weathering rate equation in which the parent material is dust, with no bedrock input. For detailed steps to the derivation, see Appendix 3.

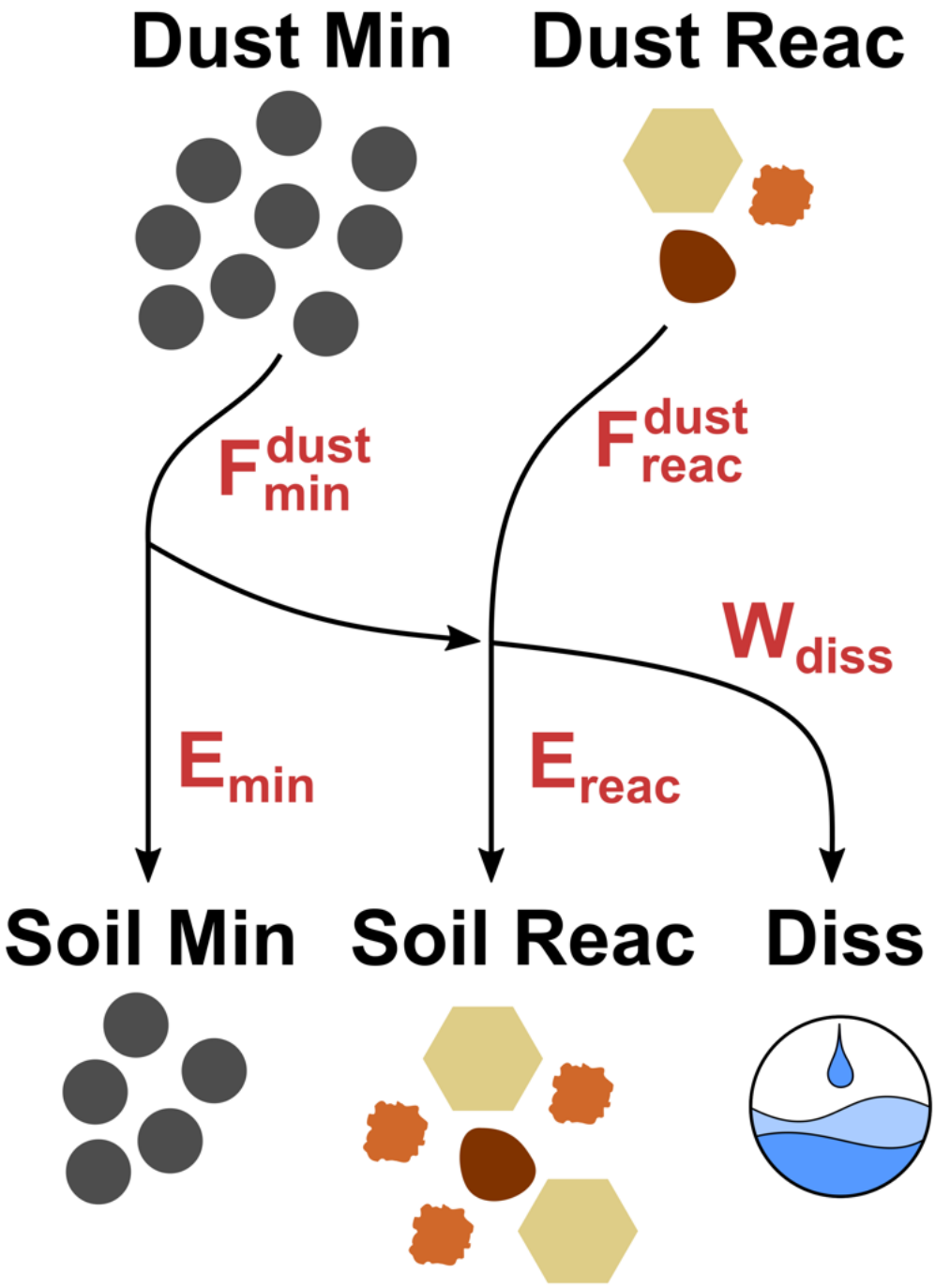

Figure 2: Weathering pools and fluxes with dust

In this case, the weathering rate equation takes a new, complicated form:

$$\left(\frac{^{10}Be}{^{9}Be}\right)^{soil}_{reac} = \frac{F^{^{10}Be}_{met} + F^{dust}_{reac}\ [^{10}Be]^{dust}_{reac\prime}}{[\,^{9}Be]^{dust}_{min\prime} W_p + F^{dust}_{reac}[\,^{9}Be]^{dust}_{reac\prime}}$$

(Eq. 2.2.25)

$\left(\frac{^{10}Be}{^{9}Be}\right)^{soil}_{reac}$ = The $^{10}Be/^{9}Be$ ratio in the reactive pool of the soil

With this equation, we can see that the W_p weathering rate can be determined, but we still require a lot of information. Not only do we need to measure a $^{10}Be/^{9}Be$ ratio and ^{9}Be concentration within the mineral phases of the dust, but we must also measure ^{9}Be and ^{10}Be concentrations within the dust reactive pools, and determine the fluxes of total dust, as well as the flux of dust in the reactive pool.

However, if we can assume that the $^{10}Be/^{9}Be$ ratio in the reactive pool of the dust is the same as the $^{10}Be/^{9}Be$ ratio in the reactive pool of the soil, the equation simplifies a great deal. See Appendix 3 for the detailed steps.

Assuming that $\left(\frac{^{10}Be}{^{9}Be}\right)^{dust}_{reac} = \left(\frac{^{10}Be}{^{9}Be}\right)^{soil}_{reac}$ this equation simplifies to:

$$\left(\frac{^{10}Be}{^{9}Be}\right)^{soil}_{reac} = \frac{F^{^{10}Be}_{met}}{[\,^{9}Be]^{dust}_{min\prime} W_p}$$

(Eq. 2.2.26)

Therefore, if the $^{10}Be/^{9}Be$ ratio in the reactive pool of the dust is the same as the isotope ratio in the reactive pool of the soil, the equation simplifies to the original form, as derived for bedrock weathering. The difference is that, in order to calculate a W_p weathering rate, we must now use the ^{9}Be concentration in the primary mineral pool within the dust, rather than the bedrock.

As with the bedrock weathering model, we could expand this equation for any number of weathering mineral phases within the dust. In this case, the calculated weathering rate (W_p)

would the weighted sum of the weathering rates of the individual mineral phases within the parent dust, weighted by the ^{9}Be concentration within each mineral phase from the dust.

Dissolved ^{10}Be/^{9}Be in groundwater archives

For groundwater archives of beryllium isotopes (i.e. speleothems) to be used to ascertain information about weathering rate, we must make a key assumption. Following von Blanckenburg et al. (2012), the ^{10}Be/^{9}Be ratio in the dissolved phase must equal that in the reactive phase.

Assuming $\left(\frac{^{10}Be}{^{9}Be}\right)_{reac} = \left(\frac{^{10}Be}{^{9}Be}\right)_{diss}$

In this case, the $\left(\frac{^{10}Be}{^{9}Be}\right)_{reac}$ or $\left(\frac{^{9}Be}{^{10}Be}\right)_{reac}$ term in the above equations can be interchangeably substituted for the dissolved ^{10}Be/^{9}Be. Speleothems may contain both dissolved species that co-precipitate with the carbonate, as well as inorganic and organic colloids of the reactive pool that are occluded and trapped within the carbonate as it forms.

Beryllium isotopes in the groundwater have no way of equilibrating with Be isotopes associated with reactive phases at the surface in the soil. Therefore, for this assumption to be true, the groundwater must not pick up any more ^{9}Be in transit from soil to stream. In karst landscapes where a sizeable fraction of chemical weathering occurs in the subsurface, it is possible that this condition is not met, However it is also possible that the beryllium is transported in colloids and as organic complexes, which could potentially bypass the addition of ^{9}Be from dissolution of bedrock in the subsurface.

Trace metals are transported from the soil to speleothems in solution or in association with colloids and particulates (Hartland et al., 2012). Colloids remain permanently in suspension due to Brownian motion and slight currents (Pédrot et al., 2008). The pH in the soil may be acidic if carbonates have been leached out, as is the case in terra rossa. Therefore, reactive pedogenic phases in the soil may form in isotopic equilibrium with the dissolved phase. However, in the

subsoil where carbonates are still present, pH raises to basic, and beryllium should be immobile. Therefore, it is likely that colloids are the primary means of beryllium transport in karst groundwaters. This has yet to be examined.

The concentrations of trace metals in speleothems may be partially controlled by the sizes of the colloids and particulate materials with which they associate (Hartland et al., 2012). In high-flow bedrock systems where dripwater is mostly fracture-fed, particulate material (>1µm), colloids (1nm-1µm), and dissolved (<1nm) fractions migrate at similar rates. However, in slow seepage-flow dripwaters, particulates and small colloids (and associated trace metals) may migrate at different rates, or may even be filtered out through blockage in pores (Hartland et al., 2012).

Furthermore, natural organic matter colloids can be particularly important for the delivery of trace metals to speleothems, and NOM-metal complexes can co-precipitate with speleothems as they form (Hartland et al., 2014). Variations in some trace element concentrations within speleothems can be explained by changes in calcite precipitation rate, and from differences in metal complexation behavior with NOM (Hartland et al., 2014).

Section 3: Background – geological and environmental settings

I combined Be with Li isotopic analyses in speleothems in order to examine temporal variations in weathering attributes (i.e., weathering rate, congruency, and intensity) at a local scale. Although my primary objective was to determine how weathering varied between glacial and interglacial periods, I recognized that a multitude of factors could impact the $^{10}Be/^{9}Be$ ratio, such as changes in rainfall, dust flux, and ^{10}Be production rate in the atmosphere (as I discuss in chapter 1). Rainfall and dust flux in particular could also vary over glacial cycles, much like chemical weathering rate.

My speleothem samples come from Soreq cave in Israel and range from 0 to 168 ka in age. I present additional measurements of Be isotopes in an early-Pleistocene flowstone from Buffalo Cave in South Africa in Appendix 1.

Section 3a: Soreq Cave

I measured beryllium isotopes in 18 samples from 9 speleothems from Soreq Cave. All have δ^7Li measurements by Pogge von Strandmann et al. (2017) which elucidate how chemical weathering congruency is impacted by climate. Geochronology was previously determined by Bar-Matthews et al. (2003), Grant et al. (2012), and Vaks et al. (2006).

Soreq Cave is situated on the western side of the Judean Mountains west of Jerusalem and has a continuous record through both glacial and interglacial times. In contrast, Tzavoa Cave, which I use for some Li data, is situated in the Northern Negev Desert. No modern speleothem growth occurs in Tzavoa cave, and the speleothem record is discontinuous during segments of interglacial times (Vaks et al., 2006).

Changes in temperature

Paleotemperature proxies indicate that the region was approximately 5-10 ºC cooler than present at the Last Glacial Maximum (LGM), with a maximum temperature of 17-22 ºC at 120-130 ka during the last interglacial period. Local paleotemperatures have been constrained by clumped isotopes from Soreq Cave speleothems (Affek et al., 2008), and δD measurements (McGarry et al., 2004) from fluid inclusions in speleothems from Soreq and other Eastern-Mediterranean caves.

Additionally, a discontinuous record of sea-surface temperature comes from a marine core in the Mediterranean, in which Emeis et al. (1998) constrained temperatures using marine alkenones. They specifically sampled from sapropels (dark sediments rich in organic carbon) that form during high-rainfall, low temperature conditions. Each of these sapropels roughly correspond with periods of low δ^{18}O in the Soreq Cave speleothems (Bar-Matthews et al., 2000).

Pogge von Strandmann et al. (2017) find a close relationship between δ^7Li and paleotemperature in speleothems from Soreq and Tzavoa caves. This led them to conclude that temperature exerts primary control of weathering congruency, with congruent weathering occurring during warmer temperatures. These data make Soreq Cave a unique setting in which my Be-isotope

measurements in speleothems can be compared to independent temperature and weathering proxies.

Changes in rainfall

Rainfall is an important variable to consider when exploring the relationships between chemical weathering and climate. Additionally, the $^{10}Be/^{9}Be$ ratio may also be sensitive to variations in $^{10}Be_{met}$ flux due to changes in rainfall.

During the 200 ka timespan of speleothem growth for the Soreq and Tzavoa samples, no substantial speleothems formed south of Tzavoa Cave. Samples from both caves display similar $\delta^{18}O$ trends, suggesting a shared moisture source. These lines of evidence led Vaks et al. (2006) to conclude that Eastern Mediterranean Sea has remained the primary source for rainfall in both caves throughout the period of speleothem growth.

Several workers have speculated on the extent to which rainfall has varied above Soreq Cave over the last several hundred thousand years. Many proxies for moisture (such as speleothem growth rates or the level of nearby paleo-lake Lisan) depend on evaporation as well as rainfall. Nevertheless, Vaks et al. (2010) infer that intervals of speleothem growth in the Negev Desert, south of Soreq Cave, indicate that rainfall could have been relatively high during 225–190 ka (Negev Humid Period 2) and 142–109 ka (Negev Humid Period 1).

Bar-Matthews et al. (2003) reconstruct a discontinuous record of annual rainfall above Soreq cave using oxygen isotopes and find a long-term trend of increasing aridity over the last 7 ka. However, their paleo-precipitation record is limited to periods in which separate proxies exist for paleotemperature, as they needed to correct the oxygen isotope fractionation for variations in temperature. Furthermore, their rainfall reconstruction relies on an empirically-derived relationship between $\delta^{18}O$ and rainfall that was calibrated by modern measurements. Therefore their rainfall reconstruction is only valid for periods in which the $\delta^{18}O$ of the moisture source (i.e. the Mediterranean) was the same as it is today.

Terra rossa soil: dust flux and source

Dust flux and source are important both because dust is likely to be the primary source of silicates to the landscape above Soreq cave, and because dust may carry beryllium with a foreign $^{10}Be/^{9}Be$ ratio.

The soil above Soreq cave is a Mediterranean terra rossa. These soils characteristically form in karstic limestone landscapes in Mediterranean climates with loess or alluvium covers. The bedrock promotes a neutral pH and quick drainage (Boero & Schwertmann, 1989). Terra rossas get their bright red hue from an abundance of hematite, formed from iron released during weathering of the autochthonous carbonate bedrock and allochthonous loess or alluvium.

Silicates and phyllosilicates in the soil above Soreq Cave must derive from dust, and not bedrock (Ben-Asher et al., 2019). Analysis of a terra rossa soil from Bar Giora in the Judan Mountains, less than 4km away from Soreq Cave, reveals that the soil is composed of quartz, phyllosilicates, feldspar, dolomite, and calcite. The dust contains these phases as well, but the bedrock at Soreq Cave does not contain the silicates and phyllosilicates.

To evaluate variations in dust flux, Frumkin and Stein (2004) examined $^{87}Sr/^{86}Sr$ ratios in speleothems from Jerusalem West Cave in the Judea Hills. The dust has a higher Sr isotope ratio than the dust. During glacial periods, the Sr isotopes approach the end-member of dust associated with the terra rosa from above the cave. During interglacial periods, the Sr isotope signature moves toward the dolomitic limestone bedrock end-member. This indicates that the dust flux to the landscape above Soreq cave was highest during glacial times, concurrent with heightened terra rossa soil accumulation. Jerusalem West Cave is farther inland than Soreq, and therefore the Sr isotope ratio is less impacted by Mediterranean sea-salts.

On a regional scale, Frumkin and Stein's (2004) findings of rapid dust accumulation during glacial periods are supported by loess deposits in the Negev Desert dating from the last glacial period (Magaritz, 1986), as well as deposition of desert dust in paleo-Lake Lisan, which existed from approximately 70ka to 15ka, and was the predecessor to the modern Dead Sea.

Sedimentary and geochemical evidence indicate that the Negev loess originated from multiple source regions. The grainsize of dust is bimodal, with a coarse fraction of 30-60μm, and a fine fraction of 4-8μm (Crouvi et al., 2008). The coarse fraction is mainly composed of quartz with other silicates while the finer fraction contains Al-silicates and carbonates.

Ben-Israel et al. (2015) determined that the coarse fraction of loess originates from the proximal source of the Nile delta's Sinai-Negev dunes and is produced by aeolian abrasion. Proximal loess production was intensified during glacial periods, most likely facilitated by the exposure of the delta during lower sea level.

In contrast, the fine fraction originates from two distal sources in the Sahara and Arabian Deserts. They have remained sources for the fine Negev loess for the last 200 ka. However, it appears that changes in the climates of the Sahara and the Arabian deserts have likely modulated their relative contributions to the fine fraction of loess. Ben-Israel et al. (2015) find that heightened εNd and Mg/Al in Negev primary loess sequences (dated via optically stimulated luminescence by Crouvi et al. 2008, 2009, 2010) correspond with sapropels in Mediterranean sediments. These sapropels have pronounced negative $\delta^{18}O$ values, and mark times of high Nile discharge from the strengthened African summer monsoon. Ben-Israel et al. (2015) therefore surmise that the heightened εNd and Mg/Al may indicate a decreasing dust contribution from a wetter Sahara, and/or a possible increased magnitude of Arabian dust storms.

Section 4: Methods

Since Soreq Cave is overlain by a terra rossa soil that is pedogenically derived from dust with minimal input from the underlying bedrock, I apply equation 2.2.26 from section 2 of this chapter in order to quantify chemical weathering rates (W_p):

$$\left(\frac{^{10}Be}{^{9}Be}\right)^{speleothem}_{reac\ or\ diss} = \left(\frac{^{10}Be}{^{9}Be}\right)^{soil}_{reac} = \frac{^{10}Be}{[\,^{9}Be]^{dust}_{min}, W_p}$$

(Eq. 2.4.1)

In section 4a I outline how I estimate $F_{met}^{^{10}Be}$ and $\left[\ ^{9}Be\right]_{min}^{dust}$, values. In section 4b I discuss a method to account for the long beryllium residence time in the soil, and how there may be a delayed response of the $^{10}Be/^{9}Be$ ratio to quick changes in $F_{met}^{^{10}Be}$ or W_p. Finally, in section 4c I outline the laboratory methods I used to measure the $^{10}Be/^{9}Be$ ratio in the speleothems.

Section 4a: Estimating modern and paleo-^{10}Be flux and ^{9}Be concentration in the parent

In addition to chemical weathering rate, the $^{10}Be/^{9}Be$ ratio in the speleothems could vary as a result of changes in the $^{10}Be_{met}$ flux. As I describe in chapter one, two major variables that modulate the $^{10}Be_{met}$ flux are changes in rainfall and ^{10}Be production rate in the atmosphere.

We can express the ^{10}Be flux at a given time as a function of the modern-day ^{10}Be flux, as well as the relative atmospheric production rate, and relative rainfall:

$$F_{met\ t}^{^{10}Be} = F_{met\ o}^{^{10}Be} \times \left(\frac{P_t}{P_o}\right)^{\varepsilon_P} \times \left(\frac{r_t}{r_o}\right)^{\varepsilon_{r,Be}} \times K$$

(Eq. 2.4.2)

$F_{met\ t}^{^{10}Be}$ = The flux of ^{10}Be at time 't' (atoms/cm^2/yr)

$F_{met\ o}^{^{10}Be}$ = The modern flux of ^{10}Be (atoms/cm^2/yr)

P_t = The production rate of ^{10}Be in the atmosphere at time 't'

P_o = The modern production rate of ^{10}Be in the atmosphere

r_t = Rainfall at time 't'

r_o = Modern rainfall

ε_P = Allows for a non-linear relationship between production rate and ^{10}Be flux

$\varepsilon_{r,Be}$ = Allows for a non-linear relationship between rainfall and ^{10}Be flux

K = A constant that embodies additional factors that impact ^{10}Be flux (i.e. atmospheric transport)

With this expanded definition for ^{10}Be production rate, the chemical weathering equation takes this form:

$$\left(\frac{^{10}Be}{^{9}Be}\right)_{reac}^{soil} = \frac{F_{met\ o}^{^{10}Be} \times \left(\frac{P_t}{P_o}\right)^{\varepsilon_P} \times \left(\frac{r_t}{r_o}\right)^{\varepsilon_{r,Be}} \times K}{[\,^{9}Be]_{min'}^{dust} W_p}$$

(Eq. 2.4.3)

I assume a linear relationship between rainfall and ^{10}Be flux at Soreq Cave (and therefore assume $\varepsilon_{r,Be} = 1$). This is a reasonable assumption since rainfall is low enough that we should not expect complete rainout of aerosols.

Likewise, I assume a linear relationship between atmospheric ^{10}Be production rate and ^{10}Be flux ($\varepsilon_P = 1$). Modeling by Heikkilä et al. (2009) demonstrates that the fraction of the total global ^{10}Be$_{met}$ deposited at a given latitude remains constant through changes in atmospheric ^{10}Be production rate due to modulation of geomagnetic field strength. However, a change in atmospheric transport could still change the flux in ways that are difficult to quantify.

Given these assumptions, we can simplify and rearrange this equation to solve for chemical weathering rate:

$$W_p = \frac{F_{met\ o}^{^{10}Be} \times \frac{P_t}{P_o} \times \frac{r_t}{r_o} \times K}{[\,^{9}Be]_{min'}^{dust} \times \left(\frac{^{10}Be}{^{9}Be}\right)_{Speleothem}}$$

(Eq. 2.4.4)

As I show below, we can estimate the modern ^{10}Be flux ($F_{met\ o}^{^{10}Be}$), the relative production rate in the atmosphere ($\frac{P_t}{P_o}$), as well as $[\,^{9}Be]_{min'}^{dust}$, or the ^{9}Be concentration in the weathering minerals.

<u>Estimating the modern ^{10}Be flux at Soreq and Buffalo Caves</u>

The modern-day ^{10}Be flux ($F_{met\ o}^{^{10}Be}$) at Soreq Cave can be estimated in two ways. First I use the empirically-derived equation in Graly et al. (2011), which determines the ^{10}Be flux given the latitude and rainfall at the site:

$$F_{met\ o}^{^{10}Be} = r_o \left(\frac{1.44}{1+e^{\frac{30.7-L}{4.36}}} + 0.63 \right) \times 10^4$$

(Eq. 2.4.5)

r_o = Rainfall in cm/yr

L = Latitude

$F_{met\ o}^{^{10}Be}$ = Modern ^{10}Be flux from rainfall (atoms/cm^2/yr)

Based on a modern rainfall of 500-600 mm/yr (Vaks et al., 2010; Ben-Asher et al., 2019) and the latitude of Soreq Cave (31.75ºN), this yields a value for $F_{met\ o}^{^{10}Be}$ in the range of 718,000 to 862,000 atoms/cm^2/yr.

The modern ^{10}Be flux can also be estimated using previous measurements of ^{10}Be concentrations in rainfall. Belmaker et al. (2008) measure 1000 atoms/g in rainwater from Jerusalem. Given a rainfall of 500-600 mm/yr, and assuming a rainwater density of 1g/cm^3, this measurement yields a $F_{met\ o}^{^{10}Be}$ of 750,000 to 900,000 atoms/cm^2/yr. These two methods of flux calculation are in general agreement, in part because the data from Belmaker et al. (2008) were used to calibrate the relationship in Graly et al. (2011).

Between these two methods of estimation, the average modern ^{10}Be flux at Soreq Cave is equal to approximately 807,000 atoms/cm^2/yr. I use this $F_{met\ o}^{^{10}Be}$ in the chemical weathering calculations that follow.

The model developed by Heikkilä et al (2009) is another common way to estimate the ^{10}Be flux at a site. Their work utilizes an atmospheric general circulation model to calculate ^{10}Be

deposition at a given latitude and longitude. This method yields an estimated $F_{met\ o}^{^{10}Be}$ of approximately 354,000 atoms/cm^2/yr. This value is in disagreement with the value calculated above using the method of Graly et al (2011). Nevertheless, I disregard this result using the Heikkilä (2009) method since the value calculated using the method of Graly et al. (2011) is validated by the rainwater ^{10}Be measurement of Belmaker et al. (2008).

Estimating effects of geomagnetic intensity on ^{10}Be production rate and ^{10}Be flux

In order to evaluate the impact of changes in atmospheric production rate of ^{10}Be on the $^{10}Be_{met}$ flux at Soreq and Buffalo Caves, I use the relationship outlined by the Elsässer equation:

$$\frac{P_t}{P_0} = \sqrt{\frac{M_0}{M_t}}$$

(Eq. 2.4.6)

(Eq. 9 in supplement of von Blanckenburg et al. 2015; originally Eq. 5 in Elsässer et al., 1956)

P_t = Global ^{10}Be production rate within the atmosphere at time t

P_0 = Current global ^{10}Be production rate within the atmosphere

M_0 = Current dipole moment value

M_t = Dipole moment value at time t

I used the M_t/M_0 data from the Matlab code of Lifton et al. (2014), which is used for the quantification of *in situ* cosmogenic nuclide production rates. Lifton et al. (2014) use the geomagnetic paleointensity data from CALS3K.3 (0-3 ka; Korte et al., 2009), CALS7K.2 (3-7 ka), GLOPIS-75 (7-18 ka; Laj et al., 2004), and PADM2M (beyond 18 ka; Ziegler et al., 2011).

Determining a ^{9}Be concentration in the weathering parent material

Since beryllium is insoluble in the normal pH range of karst groundwater, I expect that beryllium is transported from the soil to the speleothem via organic and inorganic colloids from the soil. If this is the case, the beryllium isotopes should record the ^{10}Be/^{9}Be ratio from the soil, and

therefore should record the chemical weathering rate (W_p) of phases in the soil. Since the most abundant mineral that is weathering in the soil is feldspar, I use a $\left[{}^{9}Be \right]_{min'}^{dust}$ value of 5 ppm, a mid-level concentration for beryllium in feldspar (Evensen & London, 2002). Future work should measure concentrations of beryllium in felspar and other mineral phases in the dust and soil in order to better constrain a reasonable $\left[{}^{9}Be \right]_{min'}^{dust}$ value.

Relative rainfall

As I discuss above, we have no quantitative reconstruction of paleo-rainfall at Soreq Cave. Without this constraint, I must assume that $\frac{r_t}{r_o} = 1$, meaning that rainfall has remained the same throughout the period I examine. Therefore, the weathering rates that I calculate are not corrected for changes in ^{10}Be flux due to changes in rainfall. This means that I will under-estimate W_p during periods with higher-than-modern rainfall, and over-estimate W_p during periods with lower-than-modern rainfall.

For ease of writing, I will refer to the weathering rates I calculate, which are not corrected for changes in ^{10}Be flux due to variation in rainfall, as W_p^*:

$$W_p{}^* = \frac{W_p}{\frac{r_t}{r_o} \times K} = \frac{F_{met\ o}^{^{10}Be} \times \frac{P_t}{P_o}}{\left[{}^{9}Be \right]_{min'}^{dust} \times \left(\frac{^{10}Be}{^{9}Be} \right)_{Speleothem}}$$

(Eq. 2.4.7)

Section 4b: Accounting for beryllium residence time in the soil

As I discuss earlier in the chapter, I expect that the ^{10}Be/^{9}Be ratio in the speleothems at Soreq Cave is recording the ^{10}Be/^{9}Be ratio in the soil above. Soils act as reservoirs of beryllium isotopes. Therefore, the ^{10}Be/^{9}Be ratio in the soil should reflect the ^{10}Be and ^{9}Be fluxes, averaged over the residence time of beryllium in the soil reservoir, and not the instantaneous ^{10}Be and ^{9}Be fluxes.

For example, if there is a sudden increase in the flux of ^{10}Be to the soil due to an increase in production rate in the atmosphere, there will be a delay between the timing of the spike and when the ^{10}Be/^{9}Be ratio increases in the soil and speleothems since beryllium residence time in the soil could be on the order of tens-of-thousands-of-years. Likewise, if chemical weathering rate increases due to an increase in temperature, thus releasing ^{9}Be at a faster rate, there will be a lag between the rise in temperature and the corresponding decrease in ^{10}Be/^{9}Be ratio in the soil and speleothem.

The residence time of beryllium isotopes in a soil can be estimated by the soil's ^{10}Be inventory and the ^{10}Be flux, or alternatively, the depth of the soil and the denudation rate (von Blanckenburg et al., 2012):

$$^{10}Be_{met}\ Residence\ Time = \frac{I}{F_{met}^{^{10}Be}} = \frac{[^{10}Be]_{soil}\sigma_{soil}\theta_{soil}}{F_{met}^{^{10}Be}}$$

$$^{9}Be \quad Residence\ Time \approx \frac{\theta_{soil}}{D} = Denudation\ Timescale$$

(Eq. 2.4.8 & 2.4.9)

D = The denudation rate (g cm^{-2} yr^{-1})

$F_{met}^{^{10}Be}$ = The flux of ^{10}Be$_{met}$ to the site (atoms cm^{-2} yr^{-1})

I = The integrated inventory of ^{10}Be$_{met}$ in the soil profile (atoms/cm^2)

σ_{soil} = Density of soil (g/cm^3)

θ_{soil} = Depth of soil (cm)

We can calculate a ^{10}Be residence time in the soil at Soreq Cave using the $F_{met}^{^{10}Be}$ value I calculate above of 807,000 atoms/cm^2/yr, as well as a soil ^{10}Be concentration of 12.5 x 10^8 atoms/g (measured by Belmaker et al., 2008 in a terra rossa soil west of Jerusalem), and assuming a bulk soil density of 1.5-2 g/cm^3 (Belmaker et al., 2008). Soil depth is difficult to constrain, since the soil above Soreq Cave is derived from dust, which extends into crevices within the bedrock below. Furthermore, the soil is patchy and non-uniform across the landscape. In certain areas,

bedrock is exposed, while other pockets contain developed soil. Further field investigation should be conducted to determine a suitable soil depth for estimation of beryllium residence time, and the ^{10}Be concentration and inventory within the soil at the field site.

Table 2.4.1: Calculated soil residence times of beryllium

Total soil depth	1 cm	5 cm	10 cm	15 cm	20 cm
^{10}Be residence time in Soil	2.7 ka	13.5 ka	27.1 ka	40.6 ka	54.2 ka

I assume the soil depth is within the range of 5-10 cm. Based on this value, I use a ^{10}Be residence time in the soil of 20,000 years. I will also assume this is roughly the residence time of ^{9}Be in the soil as well.

In order to correct the production rate for soil residence time in my calculation of weathering rate, I average $(\frac{P_t}{P_0})$ for the previous 20,000 years. Likewise, I average temperatures for the previous 20,000 years to explore the relationship between chemical weathering rate and temperature. I repeat these calculations for a 10,000 year lag-time in order to evaluate the impact of thinner soil thickness on weathering rates and the temperature dependance of weathering rates. I also present weathering rates with no corrections for soil residence time.

Section 4c: Chemistry procedures

I measured ^{10}Be and ^{9}Be concentrations in eighteen samples from nine different speleothems from Soreq Cave. I measured native ^{9}Be concentrations in the speleothems via inductively coupled plasma optical emissions spectroscopy (ICP-OES), and ^{10}Be concentrations via accelerator mass spectrometry (AMS). The detailed step-by-step methods I used are outlined in Appendix 4.

I dissolved the speleothems in HNO_3. After the carbonate was completely dissolved, I filtered the solution using a centrifuge filter (0.22µm cellulose acetate) to remove insoluble materials. I took

a small aliquot of this solution for analysis of speleothem trace element composition. The rest of the solution proceeded through chemical preparation for measurement of ^{9}Be and ^{10}Be.

Chemical preparation for ^{9}Be measurement via ICP-OES and ^{10}Be measurement via AMS

The low concentration of Be in the speleothem calcite together with the high concentration of organics proved to be obstacles for ICP-OES measurement. Dissolving multiple grams of calcite in a small volume of acid is necessary to produce solutions with a sufficiently high Be concentration to make an ICP-OES measurement. However, this approach results in unacceptably high Ca concentrations.

In order to separate calcium from beryllium I used a solvent extraction procedure. The details of this procedure are outlined in the Appendix. In short, after dissolving the speleothem and filtering the solution, I complexed the beryllium with acetylacetone (~1% by volume in solution), and complexed most of the calcium with 0.5M Na_2-EDTA at pH=7. At this acidity, quantitative retention of beryllium by the acetylacetone is expected (Shigematsu & Tabushi, 1960). Next, I used chloroform to dissolve the acetylacetone and beryllium. I separated the chloroform (with Be) and aqueous EDTA solution (with most of the Ca) by density. Then, I back-extracted the beryllium from the chloroform using 50% HCl.

Finally, after drying-down the HCl, I dissolved the residue in 5% HNO_3. One aliquot of this solution went to the ICP-OES for measurement of the native ^{9}Be concentration within the speleothem carbonate. The rest of the solution was allocated for ^{10}Be measurement via AMS. I spiked this solution with beryllium carrier and proceeded with the chemical procedures to produce AMS targets, as outlined in Appendix 4.

Loss of beryllium during the solvent extraction could impact the calculated ^{10}Be and ^{9}Be concentrations within the speleothem. However, incomplete recovery of beryllium during the solvent extraction should have no impact on the measured speleothem $^{10}Be/^{9}Be$ ratio since both the ICP-OES measurement of ^{9}Be, and the AMS measurement of ^{10}Be were conducted on aliquots of the same solution after the solvent extraction. Nevertheless, the absolute ^{10}Be and ^{9}Be

concentrations within the speleothems were important data to assess. Therefore, I sought to evaluate the efficiency of beryllium recovery during the solvent extraction procedure.

To evaluate the potential for beryllium loss in the solvent extraction method, I examined several samples with unusually high beryllium concentrations. With high Be concentrations I could dissolve a smaller mass of carbonate and still make a direct measurement on the ICP-OES without concern for high Ca concentration. Therefore, for these samples I could compare the directly measured Be concentrations with Be concentrations measured after solvent extraction.

The first sample I used for comparison was a commercially available travertine tile. I crushed the tile into a homogenous powder using a shatterbox. I directly measured the Be concentration on one aliquot, while I separated the Be from the Ca with a second aliquot using the solvent extraction method. The direct measurement yielded 176.8 ng of Be per g calcite.
The solvent extraction recovered 181.8 ng of Be per g calcite. The less-than 3% difference between these two reported concentrations is within the uncertainty of the ICP-OES measurements. Furthermore, the aliquot measured after the solvent extraction procedure produced a higher calculated Be concentration. Therefore, this test indicated that the solvent extraction procedure quantitatively recovers all of the beryllium from the carbonate, within the uncertainty of ICP-OES measurement. This agrees with the findings of Shigematsu & Tabushi (1960).

Measurement of trace element concentrations via ICP-OES

With the aliquot of the dissolved speleothem taken before the solvent extraction procedure, I measured a suite of speleothem trace-elements including Al (167.018nm), P (177.433nm), Ni (221.65nm), Fe (238.207nm), Mn (260.575nm), Ti (334.941nm), Sr (407.771nm), and Ba (493.408nm). This was primarily to evaluate the transport mechanisms of beryllium within the vadose zone.

Section 5: Results

Concentrations of ^{9}Be range from 8-28 ppb in the speleothems from Soreq Cave, while ^{10}Be concentrations range from $1.807x10^{6}$ to $19.305x10^{6}$ atoms/g. The decay-corrected $^{10}Be/^{9}Be$ ratios range from $3.597x10^{-9}$ to $1.157x10^{-8}$, indicating that the ratio varies by a factor of 3.2 over the time-interval measured.

In Figure 3 I present the $^{10}Be/^{9}Be$ data in context with the $\delta^{7}Li$ weathering-congruency proxy (Pogge von Strandmann et al., 2017), the $^{87}Sr/^{86}Sr$ dust-flux proxy (Frumkin & Stein, 2004), along with cave temperatures (McGarry et al., 2004; Affek et al., 2008) and speleothem $\delta^{18}O$ (Bar-Matthews et al., 2003). The $^{10}Be/^{9}Be$ ratio appears to decrease from the earliest records until approximately 125ka. Then it increases over the interval of 125ka to the LGM. This follows the same trend as $\delta^{7}Li$ in Soreq Cave and $^{87}Sr/^{86}Sr$ in the nearby Jerusalem West Cave, and the inverse trend of cave temperatures at Soreq.

The samples during the Holocene break with this trend; while measured temperatures rise rapidly from the LGM to the present, $\delta^{7}Li$ and $^{87}Sr/^{86}Sr$ change rapidly as well, however the measured $^{10}Be/^{9}Be$ remains stagnant. Due to these differences between the pre- and post-LGM samples, and the anomalously low $^{10}Be/^{9}Be$ of the sample at the LGM, I have labeled the data as "pre-LGM, at-LGM, and post-LGM" in Figures 5, 6, 7, and 8.

Calculated chemical weathering rates (W_p) range from roughly 2-9 tons/km^2/yr based on the assumption that the weathering mineral pool has a ^{9}Be concentration of 5ppm (roughly matching feldspar, as I discuss in section 4 of this chapter). Changing the assumed concentration would change the absolute value of the calculated weathering rate, but not the relationship between weathering rate and temperature, or other parameters.

Based on the estimated residence time of beryllium in the soil of 20,000 years, I present lag-corrections of the production rates and temperatures in Figure 4, along with a 10,000 year lag in order to explore the impact of thinner soils on the weathering rate and its relationship with temperature. Production rates were mostly higher than today throughout the time interval. Therefore, $^{10}Be/^{9}Be$ normalized by relative production rate is mostly lower than the measured

$^{10}Be/^{9}Be$. Thus, most of the calculated chemical weathering rates are higher once production rate variation is taken into account (Figure 4).

Figure 5 shows the relationship between $^{10}Be/^{9}Be$ and temperature, and Figure 6 shows the relationship between the calculated weathering rates and temperature. These plots only show the temporal subset of beryllium data for which temperatures have been measured. Therefore they exclude data past ~125 ka. Taken as a whole, the measured $^{10}Be/^{9}Be$ ratio does not display a meaningful relationship with temperature. However, the pre-LGM samples display an inverse relationship between $^{10}Be/^{9}Be$ and temperature, while the post-LGM samples show a flat relationship. In contrast, once a 20,000 year soil residence time is taken into account, the pre-LGM and post-LGM samples fall on the same curve, however the sample at the LGM remains noticeably different than all other samples. These findings are similar for weathering rate and temperature. With a 20,000 year soil residence time, chemical weathering rates show a clear positive relationship with temperature.

Figure 7 shows the relationship between $^{10}Be/^{9}Be$ and $^{87}Sr/^{86}Sr$, a dust-flux proxy measured in speleothems from Jerusalem West cave by Frumkin & Stein (2004). The relationship between Be isotope and Sr isotope ratios is weak, even when taking into account a 20,000 year soil residence time. There is a slight positive relationship between the two isotope ratios, although the relationship is more pronounced for the Pre-LGM samples.

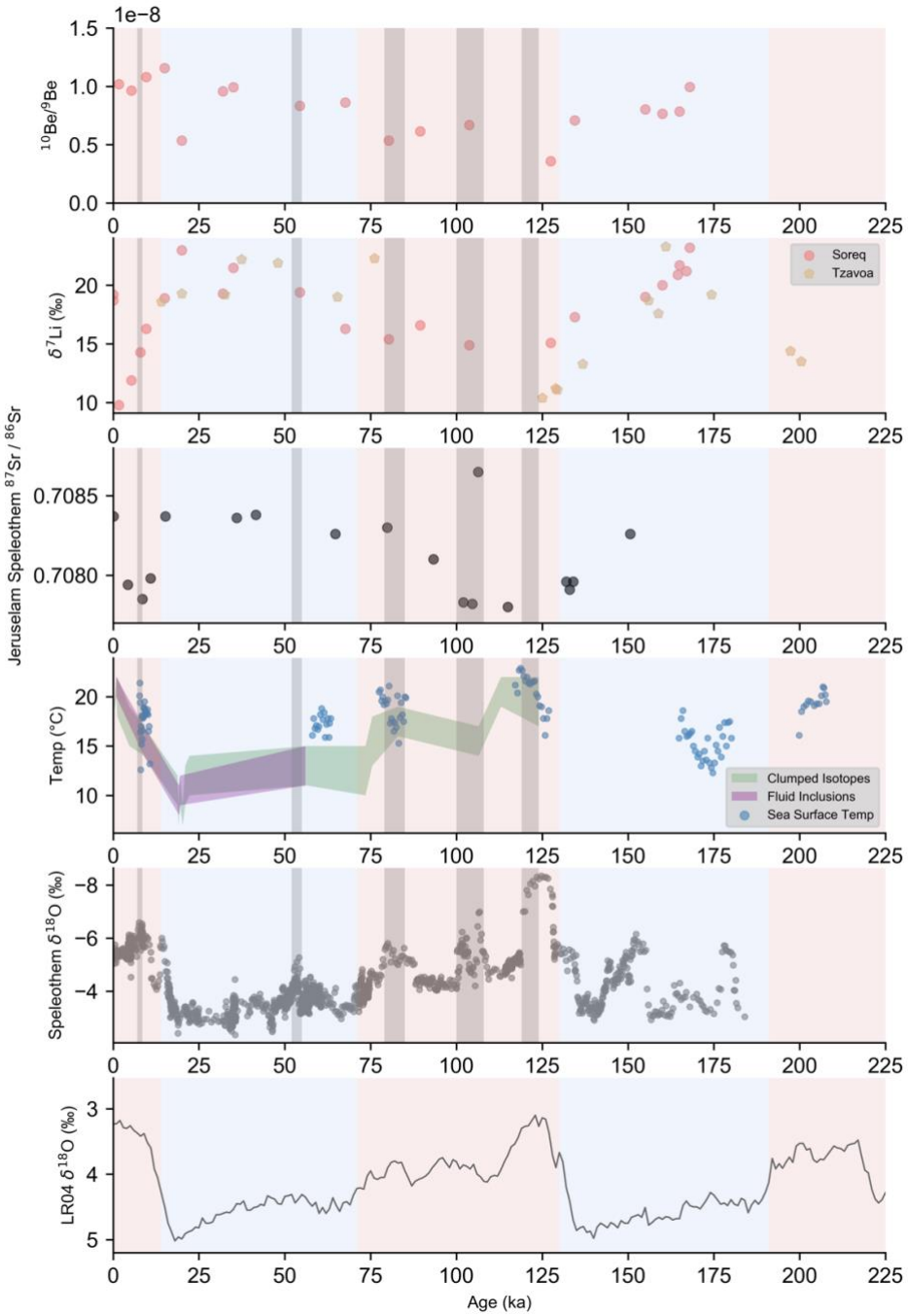

Figure 3: Soreq Cave data in context: paleotemperature and Be, Li, Sr, and O isotopes

Be-isotope data from Soreq Cave and comparison to δ^{7}Li weathering congruency proxy (Pogge von Strandmann et al.,2017), Sr-isotope proxy for dust-flux from Jerusalem West Cave (Frumkin & Stein, 2004), Soreq Cave temperatures (dD in fluid inclusions from McGarry et al., 2004 and clumped isotopes from Affek et al.,2008), Mediterranean sea-surface temperatures (marine alkenones from Emeis et al., 1998), speleothem $\delta^{18}O$ (Bar-Matthews et al., 2003), and the global bethic stack $\delta^{18}O$ (LR04: Lisiecki & Raymo, 2005). Vertical gray bands represent periods of low speleothem $\delta^{18}O$ which correspond roughly to sapropels in the Mediterranean sedimentary record (Bar-Matthews et al., 2000). Light-red shading represents global interglacial intervals, and light-blue shading represents global glacial intervals based on marine isotope stages (Lisiecki & Raymo, 2005).

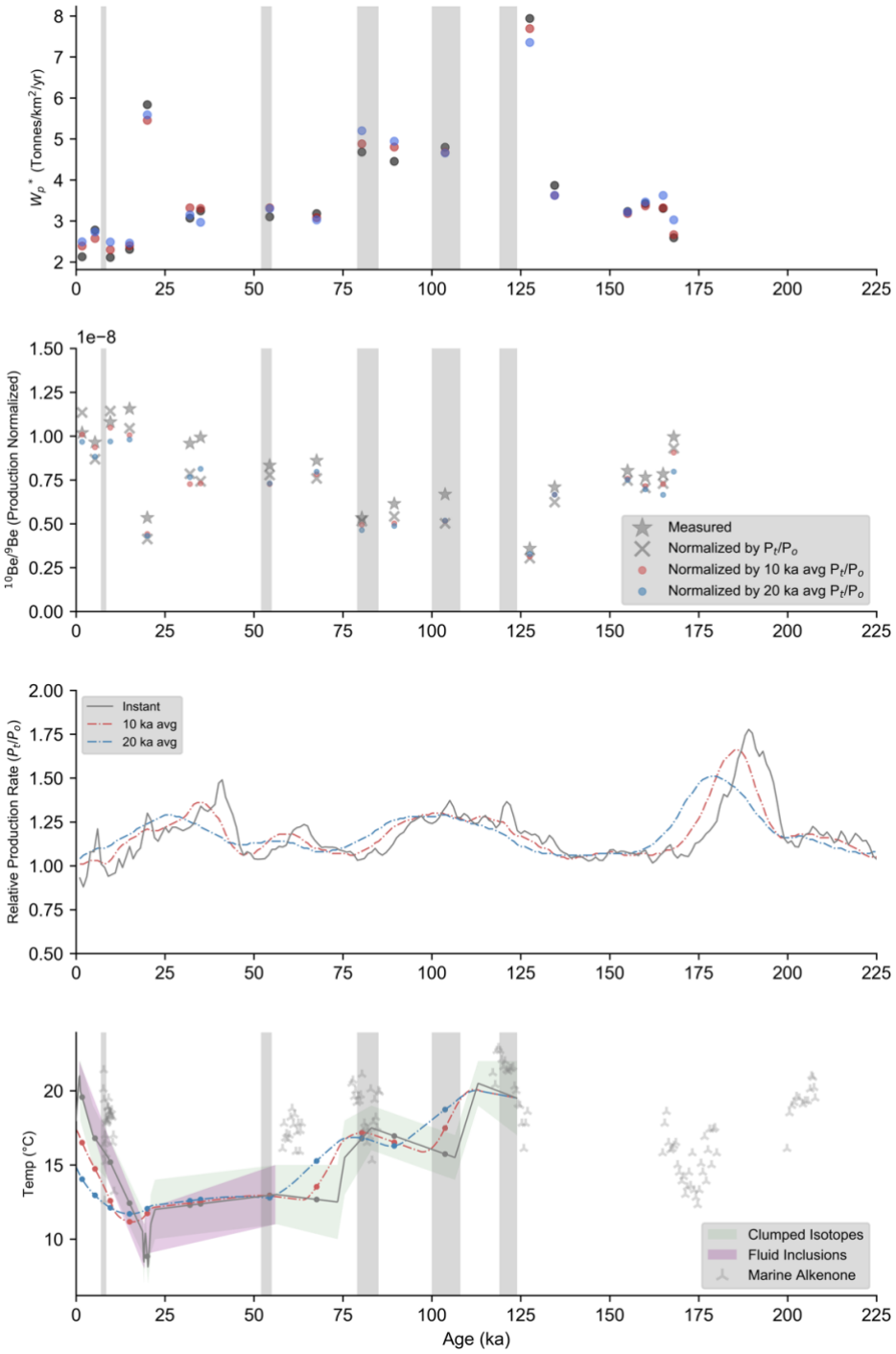

Figure 4: Accounting for soil residence time: lagged temperature, production rate, ^{10}Be/^{9}Be, and W_p^* weathering

From bottom to top: (1) Average cave temperatures at Soreq Cave. Gray curve is the instantaneous average temperature. The red curve averages the previous 10 ka of temperatures, the blue curve averages the previous 20 ka of temperatures. Marine temps are presented, but are not used for the calculation of these curves. (2) Production rate of ^{10}Be in the atmosphere relative to today. Details in the methods section. The gray curve is the instantaneous production rate. The red curve averages the previous 10 ka of production, and the blue curve averages the previous 20 ka of production. (3) The ^{10}Be/^{9}Be ratio. Starred values are directly measured and decay-corrected. Gray 'x' symbols are normalized by instantaneous ^{10}Be production, while red and blue points are normalized by 10 ka and 20 ka averaged production. (4) Rainfall-normalized weathering rates, with same normalizations

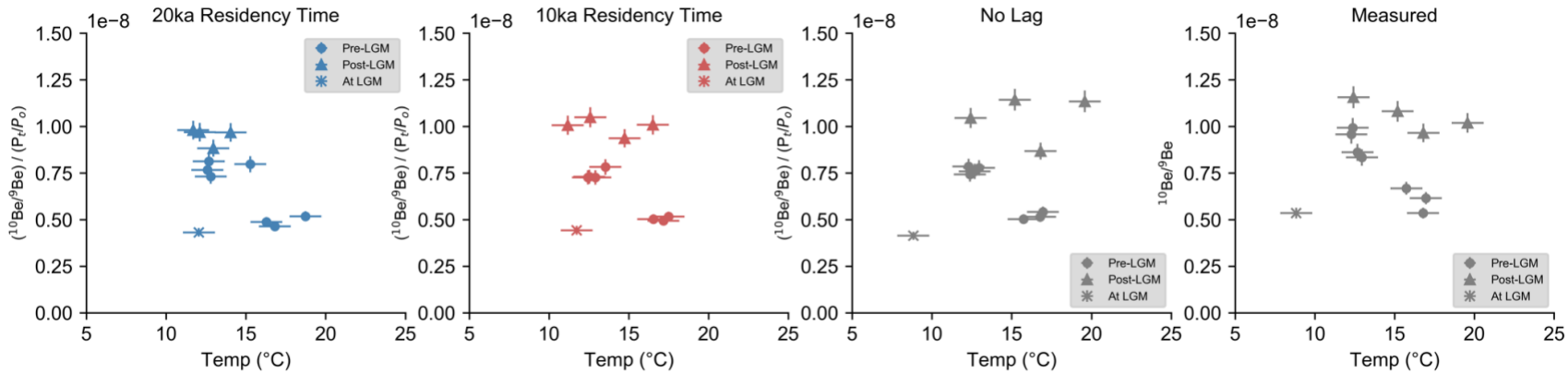

Figure 5: $^{10}Be/^{9}Be$ versus temperature

Decay-corrected $^{10}Be/^{9}Be$ versus cave temperatures. From right to left: (1) Measured values. (2) Be-isotope ratio is normalized by instantaneous ^{10}Be production rates. (3) Be-isotope ratio is normalized by the previous 10 ka of ^{10}Be production rates, while temperatures are the average of the previous 10 ka of cave temperatures. (4) Be-isotope ratio is normalized by the previous 20 ka of ^{10}Be production rates, while temperatures are the average of the previous 20 ka of cave temperatures. Be-isotope uncertainties are analytical (1-sigma). Temperature uncertainties are ±1.5°C.

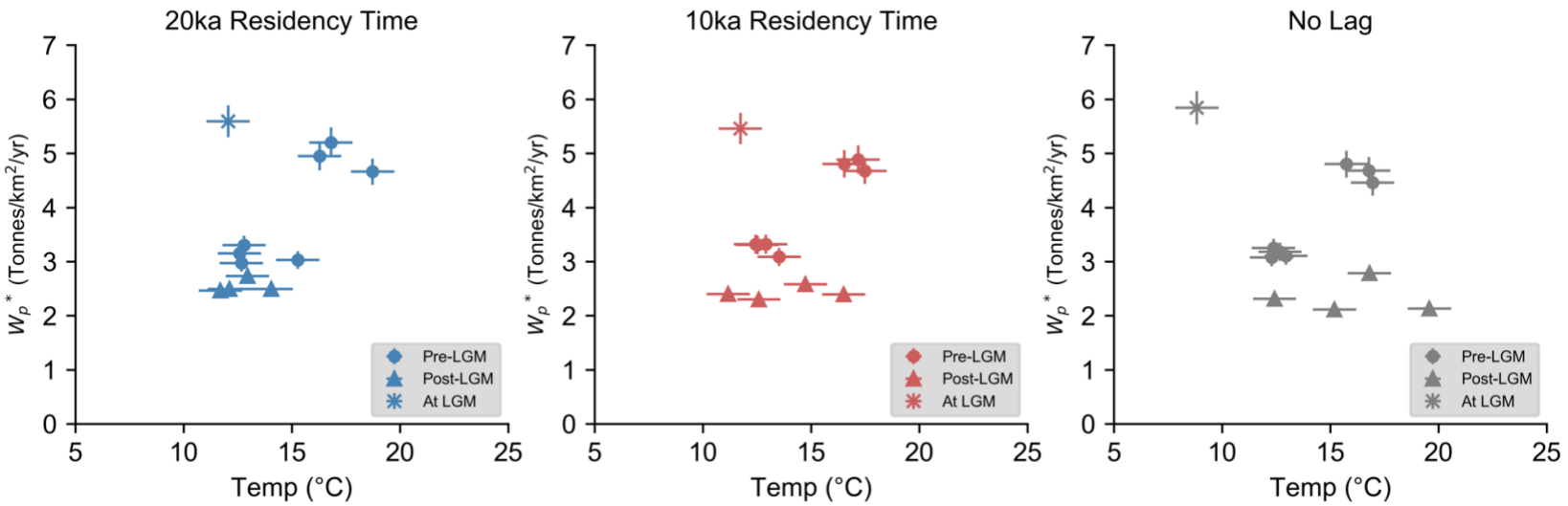

Figure 6: Rainfall-normalized weathering rate versus temperature

Calculated rainfall-normalized chemical weathering rates versus cave temperatures. From right to left: (1) No temporal lag. Weathering rates calculated with the instantaneous ^{10}Be production rate. (2) Weathering rates calculated with the 10 ka production-rate average. Temperatures are average of previous 10 ka. (3) Weathering rates calculated with the 20 ka production-rate average. Temperatures are average of previous 20 ka. Weathering rate uncertainties are analytical (1-sigma). Temperature uncertainties are ±1.5°C.

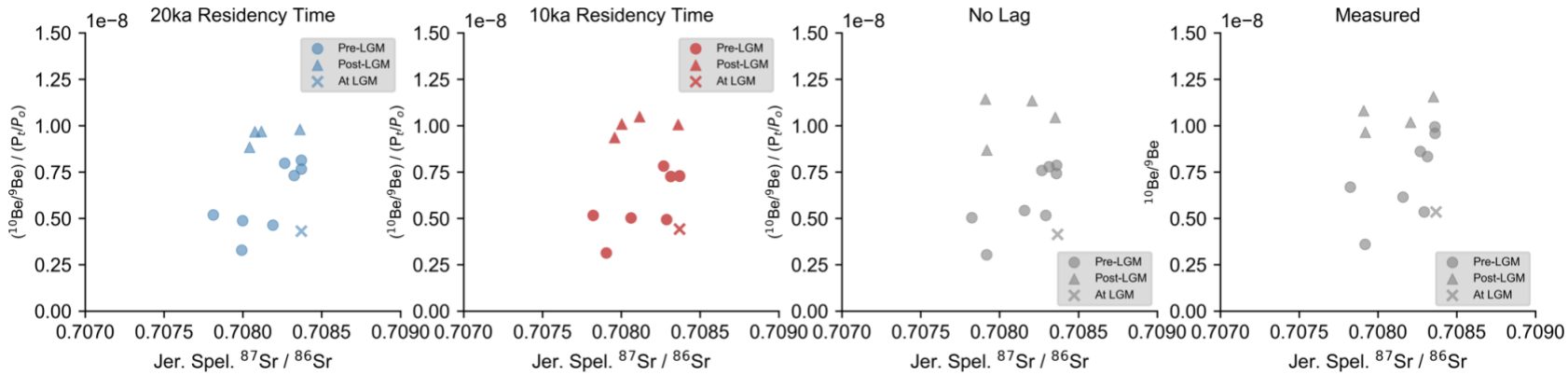

Figure 7: $^{10}Be/^{9}Be$ versus $^{87}Sr/^{86}Sr$

Decay-corrected $^{10}Be/^{9}Be$ in Soreq Cave versus $^{87}Sr/^{86}Sr$ from Jerusalem West Cave (Frumkin & Stein, 2004). From right to left: (1) Measured values. (2) Be-isotope ratio is normalized by instantaneous ^{10}Be production rates. (3) Be-isotope ratio is normalized by the previous 10 ka of ^{10}Be production rates, while Sr-isotopes are the average of the previous 10 ka. (4) Be-isotope ratio is normalized by the previous 20 ka of ^{10}Be production rates, while Sr-isotopes are the average of the previous 20 ka.

Section 6: Discussion

Section 6a: Temperature-dependance of chemical weathering: Arrhenius relationship

The $^{10}Be/^{9}Be$ ratio and the calculated W_p show pronounced relationships with temperature, especially once a 20,000 year lag in temperature and ^{10}Be production rate is applied in order to account for the residence time of beryllium in the soil reservoir. But how reasonable is this relationship? Do our calculated weathering rates increase by a reasonable percentage, given the increase in temperature? In order to evaluate this question, we can calculate an activation-energy (E_a) for chemical weathering, based on our measured relationship between weathering rate and temperature.

As I discuss earlier in this chapter, the Arrhenius equation relates reaction rates to temperature.

$$W_p = Ae^{\frac{-E_a}{RT}}$$

(Eq. 2.6.1)

E_a = Activation energy of chemical weathering (J/mol)

A = Constant that embodies many other factors besides temperature

T = Temperature (K)

R = Ideal gas constant ≅ 8.31446 J/mol/K

Since chemical weathering rates can depend on rainfall, we can factor relative rainfall out of the 'A' constant in the Arrhenius equation, and solve for rainfall-normalized weathering rate:

$$\frac{W_p}{\left(\frac{r_t}{r_o}\right)^{\varepsilon_w}} = A_1 e^{\frac{-E_a}{RT}}$$

(Eq. 2.6.2)

ε_w = Exponent that permits for non-linear relationship between rainfall and chemical weathering

We can also solve for rainfall-normalized chemical weathering rate using the Be isotope equation:

$$\frac{W_p}{\left(\frac{r_t}{r_o}\right)^{\varepsilon_{r,Be}}} = \frac{F_{met\,o}^{^{10}Be} \times \frac{p_t}{p_o} \times K}{\left[{}^{9}Be\right]_{min'}^{dust} \times \left(\frac{^{10}Be}{^{9}Be}\right)_{Speleothem}} = W_p{}^{*} \times K$$

(Eq. 2.6.3)

Therefore, if we assume that chemical weathering and ^{10}Be flux both have a similar relationship to rainfall (i.e. assuming $\varepsilon_w = \varepsilon_{r,Be}$), the two equations can be set equal to one another:

$$W_p{}^{*} \times K = A_1 e^{\frac{-E_a}{RT}}$$

(Eq. 2.6.4)

By taking the natural-log of both sides of this equation, we can express this in a liner form:

$$ln\left(W_p{}^{*}\right) = \ln\left(\frac{A_1}{K}\right) - E_a\left(\frac{1}{RT}\right)$$

(Eq. 2.6.5)

With this relationship, we can fit a line with the slope of $-E_a$ to the measured data by plotting $\frac{1}{RT}$ versus $ln\left(W_p{}^{*}\right)$. The Y-intercept of $\ln\left(\frac{A_1}{K}\right)$ is controlled by factors other than temperature and rainfall that influence chemical weathering rate and/or ^{10}Be flux (such as the influence of soil pH, or the impact of atmospheric transport processes on ^{10}Be deposition).

Notably, since we have assumed that weathering rate and ^{10}Be flux are both impacted by rainfall in a similar manner, this equation demonstrates that we don't need to account for changes in rainfall in order to solve for an activation energy. Thus, we can calculate an activation energy without knowing the rainfall history.

I present the fit activation energy for Soreq Cave in Figure 8. Based on a beryllium residence time of 20,000 years in the soil, I calculate an activation energy of 96.7 ± 16.3 kJ/mol. Since I expect that the beryllium isotope ratio is measuring the weathering rate of feldspar in the soil above the cave, I interpret this as the activation energy of feldspar chemical weathering.

How does this activation energy compare to activation energies for feldspar that are reported in the literature? It is important to note that the chemical weathering rate that the beryllium isotopes are measuring (W_p) is the sum of several weathering reactions including direct dissolution of feldspar into the dissolved phase, as well as secondary mineral production from feldspar (for example kaolinization of feldspar). Therefore, the activation energy I calculate could be different from the activation energies of these individual weathering reactions (i.e. the E_a of kaolinization of feldspar).

The activation energy that I calculate is high, but within the range of field-based estimates for feldspar. Williams et al. (2010) estimate an E_a of 75±14 kJ/mol for the chemical weathering of albite in loess soils across a climate gradient along the Mississippi River in North America. They use the release of Na from the albite to quantify mineral loss. This means that their activation energy should encompass albite loss to both the secondary mineral pool and the dissolved pool, since Na is not significantly incorporated into secondary phases. Velbel (1993) calculates an E_a of 77 kJ/mol for plagioclase in a watershed in North Carolina. Dorn & Brady (1995) calculate a higher E_a of 109 kJ/mol for plagioclase by measuring plagioclase porosity via scanning electron microscopy in basalts along a temperature gradient in Hawaii.

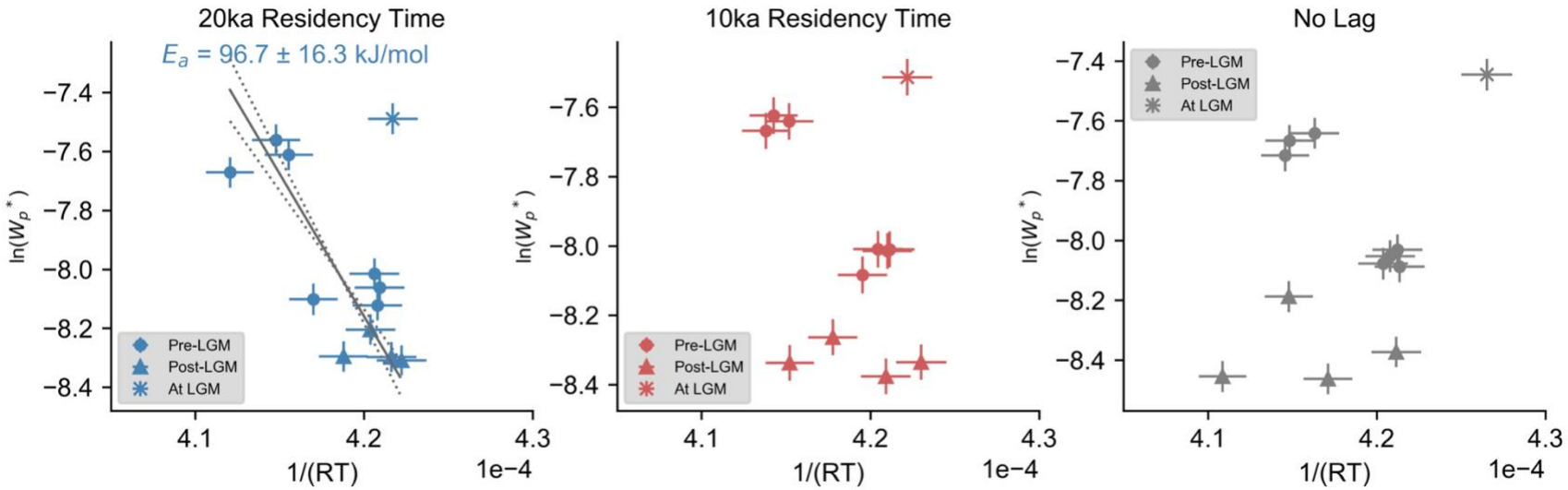

Figure 8: Arrhenius relationship of weathering rate and temperature

Calculated activation energy (E_a) of chemical weathering. Slope of the regression equals the negative activation-energy. From right to left : (1) No temporal lag. Weathering rates calculated with the instantaneous ^{10}Be production rate. (2) Weathering rates calculated with the 10 ka production-rate average. Temperatures are average of previous 10 ka. (3) Weathering rates calculated with the 20 ka production-rate average. Temperatures are average of previous 20 ka. Weathering rate uncertainties are analytical. Temperature uncertainties are ±1.5°C. Activation energy and associated uncertainty calculated via a York regression, taking into account both X and Y uncertainties of 1-sigma.

Section 6b: What if rainfall and temperature co-vary?

The $\frac{r_t}{r_o}$ term in the weathering rate equation accounts for the impact of rainfall on ^{10}Be flux. Since we don't have good quantitative constraints on rainfall, the weathering rates (W_p^*) that I calculate are all based on modern day rainfall (and therefore, modern-day ^{10}Be flux). In other words, for all the weathering rates that I calculate I use a $\frac{r_t}{r_o}$ value of 1. However, if we could reasonably quantify how rainfall changed over time ($\frac{r_t}{r_o}$) with an independent proxy, we could determine more accurate W_p values.

Since I have used modern rainfall for the ($\frac{r_t}{r_o}$) value for every sample, I am under-estimating W_p during periods with higher-than-modern rainfall, and over-estimating W_p during periods with lower-than-modern rainfall. Therefore, since temperature and rainfall are likely to co-vary, this means that I am likely over-estimating W_p during colder times, and under-estimating W_p during warmer times.

However, it is important to note that the ($\frac{r_t}{r_o}$) term assumes that ^{10}Be flux tracks with local changes in rainfall. However, it is possible that comparison to global rainfall is more important for determining ^{10}Be flux. For instance, if global rainfall was lower during the Pleistocene, then a local decrease in rainfall during the Pleistocene could in actuality have little impact on ^{10}Be flux, since rainfall at the site would be similar relative to the global average (i.e. if $\left(\frac{r_t}{r_o}\right)_{global} \cong \left(\frac{r_t}{r_o}\right)_{site}$).

The ^{10}Be/^{9}Be ratios I calculate vary by a factor of more than 3 during the examined timeframe, and show a negative relationship with temperature. This suggests that the beryllium isotope ratio is reflecting changes in temperature-dependent chemical weathering rates. However, since temperature and rainfall are likely to co-vary at this site (i.e. higher rainfall during warm times), this relationship could also be impacted by changes in ^{10}Be flux. It is important to note that the rainfall should have the opposite impact of weathering on ^{10}Be/^{9}Be. During warm times, high

rainfall should push the $^{10}Be/^{9}Be$ ratio higher, but higher weathering rates should push the $^{10}Be/^{9}Be$ ratio lower. Thus the pronounced negative relationship between temperature and $^{10}Be/^{9}Be$ indicate that, at Soreq Cave, chemical weathering is the dominant factor controlling the Be isotope ratio, not rainfall.

Section 6c: *Validating recent chemical weathering rates with modern CDF estimates*

Since we don't currently have other means to determine the temporal variation of chemical weathering rates in the landscape above Soreq Cave, it is difficult to assess the validity of the beryllium isotope weathering metric. However, we do have modern measurements of dust flux, as well as measurements of the mineralogical and elemental compositions of the dust and soil. This allows the opportunity to compare the recent beryllium-based chemical weathering rates to modern chemical weathering rates estimated from CDF.

Since the weathering rate (W_p) I calculate via beryllium isotopes is likely to reflect the weathering rate of feldspar in the soil, it is best for us to compare our data to estimates of feldspar-specific weathering rates. Feldspar and quartz are not appreciably present in the underlying carbonate bedrock as Soreq. Therefore, we will assume that both are derived exclusively from dust input.

The dust contains 35-45% quartz and 8-10% feldspar (Ben-Asher et al., 2019; their table gives a maximum value of 40% for feldspar, but this disagrees with their primary sources). In contrast, a soil from Bar Giora in the Judean Mountains (less than 4km away from Soreq) contains 39-70% quartz and 5-12% feldspar. If we assume that the quartz and feldspar concentrations are correlated, and that the remainder of the mineral abundances are carbonates and clays, then the feldspar/quartz ratio decreases from 0.222-0.229 in the dust to 0.128-0.171 in the soil. Since the chemical weathering of quartz is negligible while feldspar is present, this change in mineralogical ratio is likely to reflect the chemical weathering of feldspar in the soil relative to recalcitrant quartz.

As I discuss earlier in this chapter, CDF can be used to calculate a total chemical weathering rate if a denudation rate is known. The chemical weathering rate of a particular element can also be determined via the following relationship:

$$W_{diss,x} = D\left([x]_{rock} - [x]_{soil}\frac{[Zr]_{rock}}{[Zr]_{soil}}\right)$$

(Eq. 2.6.6)

(Eq. 3 from Riebe et al., 2004)

$W_{diss,x}$ = Weathering rate of element 'x'

D = Denudation rate

[x] = Concentration of element 'x'

If we replace the elemental concentrations with mineral concentrations, the equation can be re-written as:

$$W_{p,Fs} = F^{dust}\left([Fs]_{dust} - [Fs]_{soil}\frac{[Qz]_{dust}}{[Qz]_{soil}}\right)$$

(Eq. 2.6.7)

$W_{p,Fs}$ = W_p of feldspar

F^{dust} = Dust flux ($g/m^2/yr$)

$[Fs]_{dust}$ = Concentration of feldspar in the dust (g/g)

$[Fs]_{soil}$ = Concentration of feldspar in the soil (g/g)

$[Qz]_{dust}$ = Concentration of quartz in the dust (g/g)

$[Qz]_{soil}$ = Concentration of quartz in the soil (g/g)

I derive this equation in Appendix 7 and demonstrate how we can model this system as a set of steady-state fluxes into and out of the soil.

Comparison of recent $W_{p,Fs}$ measurements via CDF and Be isotopes

Based on this equation from Riebe et al. (2004), and using a modern dust flux of 100g/m^2/yr (Ben-Asher et al., 2019 and citations within) I estimate a modern feldspar W_p value of approximately 2.8 tons/km^2/yr. This is comparable to the most recent W_p value of 2.5 tons/km^2/yr from Be isotopes. This indicates that the ^{10}Be/^{9}Be ratio in the speleothems at Soreq Cave could be reasonably recording changes in feldspar chemical weathering rate (W_p).

Section 6d: Dust flux, chemical weathering, and ^{10}Be flux

The clear relationship between temperature and our calculated chemical weathering rates is a compelling argument that feldspar chemical weathering is kinetically-limited in the landscape above Soreq Cave. Dust flux (as observed from ^{86}Sr/^{87}Sr Frumkin & Stein, 2004) and temperature appear to inversely correlate, with higher dust fluxes during cold times (Figure 3). If chemical weathering was supply-limited in this landscape, then we would expect higher weathering rates during times with high dust flux. Figure 7 demonstrates that this is not the case. Higher ^{86}Sr/^{87}Sr ratios, (i.e., higher dust fluxes), are weakly associated with higher ^{10}Be/^{9}Be ratios. This is the opposite of what we would expect if dust supply was controlling the weathering rate. This further supports the argument that chemical weathering is kinetically-limited.

On the other hand, this weak positive relationship between dust flux and ^{10}Be/^{9}Be could indicate that the dust might contain reactive phases with a higher ^{10}Be/^{9}Be ratio than the reactive phases the soil. This is difficult to assess without direct measurements, and is certainly difficult to assess over the entire timeframe of our speleothem measurements. Nevertheless, if the dust does have a different ^{10}Be/^{9}Be than the soil, this could pose a problem for our weathering rate calculations, since we have assumed that they have similar ratios in the reactive pool. This warrants further investigation.

Section 7: Conclusions

I have developed a new metric of chemical weathering rate using beryllium isotopes. I demonstrate how the $^{10}Be/^{9}Be$ ratio can be used to determine the weathering rate W_p, which encompasses loss of parent material in both the dissolved and secondary (reactive) phases.

In order to apply this new Be isotope weathering metric, I measured $^{10}Be/^{9}Be$ ratios in speleothems from Soreq Cave in Israel. Separate proxies for temperature and dust flux allowed me to examine the extent to which chemical weathering is kinetically-limited or supply-limited. The results indicate that chemical weathering rates in this landscape increase with temperature, and have a weak inverse relationship with dust flux. This indicates that chemical weathering is kinetically limited in this environment.

The most recent chemical weathering rate calculated with Be isotopes seems to reasonably match modern chemical weathering rates of feldspar calculated via the CDF-method using quartz and feldspar ratios in the soil and dust. Likewise, the calculated Arrhenius activation energy of chemical weathering (E_a) appears to be within the range of other independent estimates of felspar weathering in the literature. This indicates that the temperature-dependance of chemical weathering that is recorded by Be isotopes at Soreq Cave is a reasonable value for feldspar.

These findings support the hypothesis that Be isotopes in speleothems at Soreq Cave are recording feldspar chemical weathering rates in the soil above the cave, and not weathering of carbonate in the pore-space of the bedrock. The finding that the calculated chemical weathering rate appears to match feldspar specifically, and not other soil minerals, is likely because feldspar is an abundant parent phase in the soil (unlike many other silicates), contains a relatively high beryllium concentration (unlike carbonates and quartz), and weathers at an appreciable rate (unlike quartz).

Without quantified values for paleo-rainfall, I cannot correct the weathering rates for changes in ^{10}Be flux due to changes in rainfall. This is particularly problematic if rainfall and temperature co-vary. This would mean that I have over-estimated weathering rates during colder times, and under-estimated weathering rates during warmer times.

Speleothems show promise as archives of the groundwater beryllium isotope ratio, and as records of chemical weathering in the landscape above caves. However, future researchers should proceed with caution before applying this weathering metric in new settings. A great deal of information about the landscape is necessary to properly interpret the data. For instance, while our data at Soreq Cave show that the $^{10}Be/^{9}Be$ ratio in the speleothems is primarily recording changes in weathering rate, at other sites with larger changes in ^{10}Be flux, the $^{10}Be/^{9}Be$ ratio could be more influenced by changes in rainfall.

Section 7a: Comparison to marine $^{10}Be/^{9}Be$

The $^{10}Be/^{9}Be$ ratio in marine sedimentary records has been stable for the past ~13 million years (Willenbring & von Blanckenburg, 2010), suggesting that the global chemical weathering flux and rate have remained constant, even as temperature has decreased throughout the Neogene, and while physical erosion rates have increased. Li et al. (2021) question this interpretation, and suggest that the stable marine $^{10}Be/^{9}Be$ ratio is the result of coastal scavenging processes.

Nevertheless, Schachtman et al. (2019) show on a local scale that chemical weathering rates can indeed remain constant across glacial-interglacial cycles. In sediments from a lake in Oregon they find that weathering intensity decreases while erosion rate increases during cooling, implying stability of chemical weathering rate.

At Soreq Cave I don't observe this trend. The calculated weathering rates vary with temperature across glacial-interglacial cycles. The landscape at Soreq Cave differs from the landscape explored by Schachtman et al. (2019) in many ways. The karst carbonate setting of Soreq Cave is certainly an uncommon setting to be studying silicate weathering rates. Another large difference between these sites is impact of glacial processes. Unlike Soreq Cave, the Oregon landscape has experienced large changes in processes such as frost shattering across glacial-interglacial cycles. Glacial processes can play a large role in modulating erosion rate.

If global weathering rate truly remains stable during cooling, then local decreases in chemical weathering must be balanced by increases elsewhere. It is possible that glacial processes help to counterbalance the decrease in weathering kinetics during cold times. Recent work on the Greenland ice sheet (Graly et al., 2014) and Antarctic ice sheet (Graly et al., 2020) indicate that modern subglacial chemical weathering rates are substantial and higher than previously assumed. Further research should explore this in greater detail.

The weathering rate data from Soreq Cave are local and cannot be extrapolated to a global scale. However, the fact that we can use Be isotopes in speleothems as a record of chemical weathering rate of silicates in the soil opens up a new way of examining how weathering rates vary spatially and temporally.

Can the differences between my results and the results of Schachtman et al. (2019) and Willenbring and von Blanckenburg (2010) be explained by differences in impact of glacial processes? How heterogeneous is the response of weathering rates to changes in temperature across continental interiors? Do changes and differences in erosion rates and glacial processes such as frost shattering cause this heterogeneity? Future research should examine how weathering rates measured with beryllium isotopes vary across latitudes and elevations (i.e. degree of impact of glacial processes), across landscapes, and across time.

Chapter 2 references

Affek, H.P., Bar-Matthews, M., Ayalon, A., Matthews, A., and Eiler, J.M., 2008, Glacial/interglacial temperature variations in Soreq cave speleothems as recorded by 'clumped isotope' thermometry: Geochimica et Cosmochimica Acta, v. 72, p. 5351–5360, doi:10.1016/j.gca.2008.06.031.

Bar-Matthews, M., Ayalon, A., Gilmour, M., Matthews, A., and Hawkesworth, C.J., 2003, Sea–land oxygen isotopic relationships from planktonic foraminifera and speleothems in the Eastern Mediterranean region and their implication for paleorainfall during interglacial intervals: Geochimica et Cosmochimica Acta, v. 67, p. 3181–3199, doi:10.1016/S0016-7037(02)01031-1.

Bar-Matthews, M., Ayalon, A., and Kaufman, A., 2000, Timing and hydrological conditions of Sapropel events in the Eastern Mediterranean, as evident from speleothems, Soreq cave, Israel: Chemical Geology, v. 169, p. 145–156, doi:10.1016/S0009-2541(99)00232-6.

Belmaker, R., Lazar, B., Tepelyakov, N., Stein, M., and Beer, J., 2008, 10Be in Lake Lisan sediments — A proxy for production or climate? Earth and Planetary Science Letters, v. 269, p. 448–457, doi:10.1016/j.epsl.2008.02.032.

Ben-Asher, M., Haviv, I., Roering, J.J., and Crouvi, O., 2019, The potential influence of dust flux and chemical weathering on hillslope morphology: Convex soil-mantled carbonate hillslopes in the Eastern Mediterranean: Geomorphology, v. 341, p. 203–215, doi:10.1016/j.geomorph.2019.05.021.

Ben-Israel, M., Enzel, Y., Amit, R., and Erel, Y., 2015, Provenance of the Various Grain-Size Fractions in the Negev Loess and Potential changes in Major dust Sources to the Eastern Mediterranean: Quaternary Research, v. 83, p. 105–115, doi:10.1016/j.yqres.2014.08.001.

von Blanckenburg, F., Bouchez, J., Ibarra, D.E., and Maher, K., 2015, Stable runoff and weathering fluxes into the oceans over Quaternary climate cycles: Nature Geoscience, v. 8, p. 538–542, doi:10.1038/ngeo2452.

von Blanckenburg, F., Bouchez, J., and Wittmann, H., 2012, Earth surface erosion and weathering from the 10Be (meteoric)/9Be ratio: Earth and Planetary Science Letters, v. 351–352, p. 295–305, doi:10.1016/j.epsl.2012.07.022.

Boero, V., and Schwertmann, U., 1989, Iron oxide mineralogy of terra rossa and its genetic implications: Geoderma, v. 44, p. 319–327, doi:10.1016/0016-7061(89)90039-6.

Caves, J.K., Jost, A.B., Lau, K.V., and Maher, K., 2016, Cenozoic carbon cycle imbalances and a variable weathering feedback: Earth and Planetary Science Letters, v. 450, p. 152–163, doi:10.1016/j.epsl.2016.06.035.

Caves Rugenstein, J.K., Ibarra, D.E., and von Blanckenburg, F., 2019, Neogene cooling driven by land surface reactivity rather than increased weathering fluxes: Nature, v. 571, p. 99–102, doi:10.1038/s41586-019-1332-y.

Crouvi, O., Amit, R., Enzel, Y., and Gillespie, A.R., 2010, Active sand seas and the formation of desert loess: Quaternary Science Reviews, v. 29, p. 2087–2098, doi:10.1016/j.quascirev.2010.04.026.

Crouvi, O., Amit, R., Enzel, Y., Porat, N., and Sandler, A., 2008, Sand dunes as a major proximal dust source for late Pleistocene loess in the Negev Desert, Israel: Quaternary Research, v. 70, p. 275–282, doi:10.1016/j.yqres.2008.04.011.

Crouvi, O., Amit, R., Porat, N., Gillespie, A.R., McDonald, E.V., and Enzel, Y., 2009, Significance of primary hilltop loess in reconstructing dust chronology, accretion rates, and sources: An example from the Negev Desert, Israel: Journal of Geophysical Research, v. 114, p. F02017, doi:10.1029/2008JF001083.

Dixon, J.L., Hartshorn, A.S., Heimsath, A.M., DiBiase, R.A., and Whipple, K.X., 2012, Chemical weathering response to tectonic forcing: A soils perspective from the San Gabriel Mountains, California: Earth and Planetary Science Letters, v. 323–324, p. 40–49, doi:10.1016/j.epsl.2012.01.010.

Dorn, R.I., and Brady, P.V., 1995, Rock-based measurement of temperature-dependent plagioclase weathering: Geochimica et Cosmochimica Acta, v. 59, p. 2847–2852, doi:10.1016/0016-7037(95)00159-W.

Elsasser, W., Ney, E.P., and Winckler, J.R., 1956, Cosmic-Ray Intensity and Geomagnetism: Nature, v. 178, p. 1226–1227, doi:10.1038/1781226a0.

Emeis, K.-C., Schulz, H.-M., Struck, U., Sakamoto, T., Doose, H., Erlenkeuser, H., Howell, M., Kroon, D., and Paterne, M., 1998, 26. Stable Isotope and Alkenone Temperature Records of Sapropels from Site 964 and 967: Constraining the Physical Environment of Sapropel Formation in the Eastern Mediterranean Sea, *in* Robertson, A.H.F., Emeis, K.-C., Richter, C., and Camerlenghi, A. eds., Proceedings of the Ocean Drilling Program, Scientific Results, Ocean Drilling Program, Proceedings of the Ocean Drilling Program, v. 160, doi:10.2973/odp.proc.sr.160.1998.

Evensen, J.M., and London, D., 2002, Experimental silicate mineral/melt partition coefficients for beryllium and the crustal Be cycle from migmatite to pegmatite: Geochimica et Cosmochimica Acta, v. 66, p. 2239–2265, doi:10.1016/S0016-7037(02)00889-X.

Foster, G.L., and Vance, D., 2006, Negligible glacial–interglacial variation in continental chemical weathering rates: Nature, v. 444, p. 918–921, doi:10.1038/nature05365.

Frings, P.J., 2019, Palaeoweathering: How Do Weathering Rates Vary with Climate? Elements, v. 15, p. 259–265, doi:10.2138/gselements.15.4.259.

Frumkin, A., and Stein, M., 2004, The Sahara–East Mediterranean dust and climate connection revealed by strontium and uranium isotopes in a Jerusalem speleothem: Earth and Planetary Science Letters, v. 217, p. 451–464, doi:10.1016/S0012-821X(03)00589-2.

Gabet, E.J., and Mudd, S.M., 2009, A theoretical model coupling chemical weathering rates with denudation rates: Geology, v. 37, p. 151–154, doi:10.1130/G25270A.1.

Graly, J.A., Reusser, L.J., and Bierman, P.R., 2011, Short and long-term delivery rates of meteoric 10Be to terrestrial soils: Earth and Planetary Science Letters, v. 302, p. 329–336, doi:10.1016/j.epsl.2010.12.020.

Grant, K.M., Rohling, E.J., Bar-Matthews, M., Ayalon, A., Medina-Elizalde, M., Ramsey, C.B., Satow, C., and Roberts, A.P., 2012, Rapid coupling between ice volume and polar temperature over the past 150,000 years: Nature, v. 491, p. 744–747, doi:10.1038/nature11593.

Haliva-Cohen, A., Stein, M., Goldstein, S.L., Sandler, A., and Starinsky, A., 2012, Sources and transport routes of fine detritus material to the Late Quaternary Dead Sea basin: Quaternary Science Reviews, v. 50, p. 55–70, doi:10.1016/j.quascirev.2012.06.014.

Hartland, A., Fairchild, I.J., Lead, J.R., Borsato, A., Baker, A., Frisia, S., and Baalousha, M., 2012, From soil to cave: Transport of trace metals by natural organic matter in karst dripwaters: Chemical Geology, v. 304–305, p. 68–82, doi:10.1016/j.chemgeo.2012.01.032.

Hartland, A., Fairchild, I.J., Müller, W., and Dominguez-Villar, D., 2014, Preservation of NOM-metal complexes in a modern hyperalkaline stalagmite: Implications for speleothem trace element geochemistry: Geochimica et Cosmochimica Acta, v. 128, p. 29–43, doi:10.1016/j.gca.2013.12.005.

Heikkila, U., Beer, J., and Feichter, J., 2009, Meridional transport and deposition of atmospheric 10Be: Atmos. Chem. Phys., p. 13.

Kasting, J.F., 2019, The Goldilocks Planet? How Silicate Weathering Maintains Earth "Just Right": Elements, v. 15, p. 235–240, doi:10.2138/gselements.15.4.235.

Knutti, R., and Hegerl, G.C., 2008, The equilibrium sensitivity of the Earth's temperature to radiation changes: Nature Geoscience, v. 1, p. 735–743, doi:10.1038/ngeo337.

Korte, M., Donadini, F., and Constable, C.G., 2009, Geomagnetic field for 0-3 ka: 2. A new series of time-varying global models: GEOMAGNETIC FIELD FOR 0-3 KA, 2: Geochemistry, Geophysics, Geosystems, v. 10, p. n/a-n/a, doi:10.1029/2008GC002297.

Laj, C., Kissel, C., and Beer, J., 2013, High Resolution Global Paleointensity Stack Since 75 kyr (GLOPIS-75) Calibrated to Absolute Values, *in* Channell, J.E.T., Kent, D.V., Lowrie, W., and Meert, J.G. eds., Geophysical Monograph Series, Washington, D. C., American Geophysical Union, p. 255–265, doi:10.1029/145GM19.

Lasaga, A.C., 1995, Chapter 2. Fundamental Approaches in Describing Mineral Dissolution and Precipitation Rates, *in* Chemical Weathering Rates of Silicate Minerals,.

Li, S., Goldstein, S.L., and Raymo, M.E., 2021, Neogene continental denudation and the beryllium conundrum: Proceedings of the National Academy of Sciences, v. 118, p. e2026456118, doi:10.1073/pnas.2026456118.

Li, W., and Liu, X.-M., 2020, Experimental investigation of lithium isotope fractionation during kaolinite adsorption: Implications for chemical weathering: Geochimica et Cosmochimica Acta, v. 284, p. 156–172, doi:10.1016/j.gca.2020.06.025.

Lifton, N., Sato, T., and Dunai, T.J., 2014, Scaling in situ cosmogenic nuclide production rates using analytical approximations to atmospheric cosmic-ray fluxes: Earth and Planetary Science Letters, v. 386, p. 149–160, doi:10.1016/j.epsl.2013.10.052.

Lunblad, K., 2006, Studies on Tropical Palaeo-variation in Climate and Cosmic Ray Influx Geochemical data from stalagmites collected in Tanzania and northern South Africa.

Magaritz, M., 1986, Environmental changes recorded in the Upper Pleistocene along the desert boundary, Southern Israel: Palaeogeography, Palaeoclimatology, Palaeoecology, v. 53, p. 213–229, doi:10.1016/0031-0182(86)90045-3.

Maurice, P., 2009, Environmental Surfaces and Interfaces from the Nanoscale to the Global Scale: Wiley.

McGarry, S., Bar-Matthews, M., Matthews, A., Vaks, A., Schilman, B., and Ayalon, A., 2004, Constraints on hydrological and paleotemperature variations in the Eastern Mediterranean region in the last 140ka given by the δD values of speleothem fluid inclusions: Quaternary Science Reviews, v. 23, p. 919–934, doi:10.1016/j.quascirev.2003.06.020.

Nesbitt, H.W., and Young, G.M., 1982, Early Proterozoic climates and plate motions inferred from major element chemistry of lutites: Nature, v. 299, p. 715–717, doi:10.1038/299715a0.

Pédrot, M., Dia, A., Davranche, M., Bouhnik-Le Coz, M., Henin, O., and Gruau, G., 2008, Insights into colloid-mediated trace element release at the soil/water interface: Journal of Colloid and Interface Science, v. 325, p. 187–197, doi:10.1016/j.jcis.2008.05.019.

Peizhen, Z., Molnar, P., and Downs, W.R., 2001, Increased sedimentation rates and grain sizes 2±4 Myr ago due to the in¯uence of climate change on erosion rates: v. 410, p. 7.

Pogge von Strandmann, P.A.E., Vaks, A., Bar-Matthews, M., Ayalon, A., Jacob, E., and Henderson, G.M., 2017, Lithium isotopes in speleothems: Temperature-controlled variation in silicate weathering during glacial cycles: Earth and Planetary Science Letters, v. 469, p. 64–74, doi:10.1016/j.epsl.2017.04.014.

Raymo, M.E., and Ruddiman, W.F., 1992, Tectonic forcing of late Cenozoic climate: Nature, v. 359, p. 117–122, doi:10.1038/359117a0.

Riebe, C.S., Kirchner, J.W., and Finkel, R.C., 2004, Erosional and climatic effects on long-term chemical weathering rates in granitic landscapes spanning diverse climate regimes: Earth and Planetary Science Letters, v. 224, p. 547–562, doi:10.1016/j.epsl.2004.05.019.

Riebe, C.S., Kirchner, J.W., Granger, D.E., and Finkel, R.C., 2001, Strong tectonic and weak climatic control of long-term chemical weathering rates: , p. 4.

Schachtman, N.S., Roering, J.J., Marshall, J.A., Gavin, D.G., and Granger, D.E., 2019, The interplay between physical and chemical erosion over glacial-interglacial cycles: Geology, v. 47, p. 613–616, doi:10.1130/G45940.1.

Shigematsu, T., and Tabushi, M., 1960, Extraction Behavior of Metal Acetylacetonates: Bulletin of the Institute for Chemical Research, Kyoto University, v. 39, p. 35–42.

von Strandmann, P.A.E.P., Kasemann, S.A., and Wimpenny, J.B., 2020, Lithium and Lithium Isotopes in Earth's Surface Cycles: Elements, v. 16, p. 253–258, doi:10.2138/gselements.16.4.253.

Vaks, A., Bar-Matthews, M., Ayalon, A., Matthews, A., Frumkin, A., Dayan, U., Halicz, L., Almogi-Labin, A., and Schilman, B., 2006, Paleoclimate and location of the border between Mediterranean climate region and the Saharo–Arabian Desert as revealed by speleothems from the northern Negev Desert, Israel: Earth and Planetary Science Letters, v. 249, p. 384–399, doi:10.1016/j.epsl.2006.07.009.

Vaks, A., Bar-Matthews, M., Matthews, A., Ayalon, A., and Frumkin, A., 2010, Middle-Late Quaternary paleoclimate of northern margins of the Saharan-Arabian Desert: reconstruction from speleothems of Negev Desert, Israel: Quaternary Science Reviews, v. 29, p. 2647–2662, doi:10.1016/j.quascirev.2010.06.014.

Velbel, M.A., 1993, Temperature dependence of silicate weathering in nature: How strong a negative feedback on long-term accumulation of atmospheric CO2 and global greenhouse warming? Geology, v. 21, p. 1059, doi:10.1130/0091-7613(1993)021<1059:TDOSWI>2.3.CO;2.

Walker, J.C.G., Hays, P.B., and Kasting, J.F., 1981, A negative feedback mechanism for the long-term stabilization of Earth's surface temperature: Journal of Geophysical Research, v. 86, p. 9776, doi:10.1029/JC086iC10p09776.

Willenbring, J.K., and von Blanckenburg, F., 2010, Long-term stability of global erosion rates and weathering during late-Cenozoic cooling: Nature, v. 465, p. 211–214, doi:10.1038/nature09044.

Williams, J.Z., Bandstra, J.Z., Pollard, D., and Brantley, S.L., 2010, The temperature dependence of feldspar dissolution determined using a coupled weathering–climate model for Holocene-aged loess soils: Geoderma, v. 156, p. 11–19, doi:10.1016/j.geoderma.2009.12.029.

Ziegler, L.B., Constable, C.G., Johnson, C.L., and Tauxe, L., 2011, PADM2M: a penalized maximum likelihood model of the 0-2 Ma palaeomagnetic axial dipole moment: PADM2M revised: Geophysical Journal International, v. 184, p. 1069–1089, doi:10.1111/j.1365-246X.2010.04905.x.

APPENDIX 1: BUFFALO CAVE FLOWSTONE

As I discuss in chapter 2, the Be-data data from Soreq Cave elucidate the relationship between chemical weathering rate and temperature in the soil above the cave. In order to evaluate whether this technique could be extended to other field sites, I measured Be-isotopes in a Pleistocene flowstone from Buffalo Cave in Makapansgat Valley, North-Eastern South Africa (1.8374 Ma to 1.5377 Ma).

Buffalo Cave sits within dolomitic limestone from the Malmani Subgroup. Unlike Soreq Cave, this setting has very little data to help constrain external variables such as temperature or dust flux.

Age Determination

Hopley et al. (2007) used several lines of evidence to date the Buffalo Cave flowstone. First, the age was approximated by comparison of faunal data from overlying fossiliferous strata. These comparisons indicate that the flowstone should be older than 0.6-0.96 Ma, based on the presence of bovid fossils that have been correlated with radiometrically dated deposits from elsewhere in southern and eastern Africa (Herries et al., 2006). Magnetostratigraphy places these faunal deposits within the Matuyama chron, and the underlying strata contain the Jaramillo normal polarity event at 1.07-0.99 Ma. The upper segment of the flowstone is reversed polarity, indicating that the youngest portion dates from within the interval of 1.77 and 1.07 Ma. At the base of the flowstone, normal and intermediate normal polarities indicate that the oldest segment dates to the Olduvai event between 1.95 and 1.78 Ma.

Attempts at radiometric dating have been unfruitful (Hopley et al., 2018; 2007). U-Pb geochronology was ineffectual due to large uncertainties associated with high $^{207}Pb/^{206}Pb$ ratios. U-Th measurements provided only a minimum age of 500 ka, as four out of six samples were in secular equilibrium. The remaining, seemingly younger samples are stratigraphically bounded by

samples that are in secular equilibrium. Textural evidence suggests that their isotopic ratios have been altered by the addition of younger, secondary calcite.

In addition to these other dating methods, Hopley et al. (2018) showed that the flowstone retains distinctive annual banding. They confirmed this using 11 tie-points to orbitally tuned $\delta^{18}O$ and $\delta^{13}C$ measurements. Via automated lamellae counting they demonstrated that there were no substantial interruptions in speleothem growth during its span. By analyzing a time series of the thickness of the laminae, they found orbital cycles. This allowed the use of orbital tuning of oxygen isotopes to more accurately constrain the timespan of the flowstone (Hopley et al., 2007).

Changes in Climate and Ecosystem

Stable isotope measurements from this flowstone demonstrate that orbital forcing controlled South African rainfall and ecosystems during the recorded period. The $\delta^{18}O$ follows the periodicity of orbital precession (18-23 ka), tracking the sub-tropical monsoon. $\delta^{13}C$ follows the periodicity of orbital obliquity (40 ka), recording shifts between C_4 grasses and C_3 trees and shrubs, suggesting that high-latitude ice-sheets were primarily responsible for driving changes in the ecosystem (Hopley et al., 2007). An additional coupling of $\delta^{13}C$ and orbital precession indicates that variations in precipitation could have also secondarily influenced changes in the ecosystem.

Long-term aridification and ecosystem change took place in southern and eastern Africa between approximately 1.8 and 1.7 Ma, driven by the onset of the Walker Circulation at 1.8 Ma. This is reflected in decreasing speleothem $\delta^{18}O$, a proxy for monsoon rainfall. A concurrent rise in speleothem $\delta^{13}C$ has been interpreted as a shift from forest to savanna. This ecosystem change is believed to be of importance for the evolution of *Homo erectus (s.l.)* in Africa (Hopley et al., 2007).

Methods

I measured beryllium isotope concentrations using the same methods that I applied for the Soreq Cave samples. The detailed methodology is outlined in chapter 2 as well as appendix 4.

Soils at the site are thin, but their meteoric ^{10}Be inventory has never been measured. Without constraints on early-Pleistocene ^{10}Be flux and the concentration of ^{9}Be in the weathering minerals, it is difficult to quantify chemical weathering rates. Furthermore, without knowing soil thickness and the ^{10}Be inventory, it is also difficult to determine the timescale of beryllium residency in the soil. Therefore, it is unclear how long of an interval the $^{10}Be/^{9}Be$ ratio is averaging. Nevertheless, I can still qualitatively compare the measured Be-isotopes to other qualitative metrics of temperature and rainfall. Future work can address these additional measurements needed for a more quantitative interpretation.

I calculated instantaneous atmospheric ^{10}Be production rates using the paleo-intensity of the geomagnetic field (M_t/M_o), following the approach I took in chapter 2 for Soreq Cave. Without a reasonable estimate of beryllium residency time in the soil, the interval over which the soil is averaging production rate variability is unclear. For the sake of discussion I present 10 ka and 20 ka moving averages (similar to chapter 2), but the true averaging time could be longer or shorter.

Results

I present the beryllium data in Figure A1.1. I corrected the $^{10}Be/^{9}Be$ ratio for decay of ^{10}Be using the orbitally-tuned ages from Hopley et al. (2007). The Buffalo Cave flowstone records an initial rise in $^{10}Be/^{9}Be$ between 1.7838 Ma and 1.7074 Ma., increasing by a factor of 3.6. After this interval, there is slow decline of $^{10}Be/^{9}Be$ between 1.7074 Ma and 1.5377 Ma., lowering by a factor of 1.2. The magnitude of this trend is not notably impacted after normalization by production rate.

Discussion

If the $^{10}Be/^{9}Be$ ratio is interpreted as a weathering rate proxy at Buffalo Cave, then weathering rates initially decreased rather dramatically between 1.7838 Ma and 1.7074 Ma., and then later increased slightly between 1.7074 Ma and 1.5377 Ma. These trends hold up even if relative atmospheric ^{10}Be production rate is taken into account (Figure A.1.1).

How does this trend in chemical weathering rate compare to climate proxies? The initial fall in chemical weathering (rise in $^{10}Be/^{9}Be$) could be attributed to the concurrent aridification and shift towards savanna grasslands. It is important to note that lower chemical weathering and lower rainfall should have opposite effects on the $^{10}Be/^{9}Be$ ratio; $^{10}Be/^{9}Be$ is increasing as it gets drier, so this trend cannot be explained by a change in ^{10}Be flux with rain. Therefore, if the Be-isotopes are recording a change in weathering rate, then the change is being under-estimated.

Without a temperature proxy with sufficient temporal resolution, it is difficult to assess the relative influences of rainfall, ecosystem, and temperature on chemical weathering at Buffalo Cave. Caley et al. (2018) reconstruct sea surface temperatures off shore of the Limpopo catchment in the Indian Ocean using foraminifera and Mg/Ca ratios in core MD96-2048. Their data reflect a regional trend of increasing temperature between 2.1 Ma and 1.4 Ma. However, the data are not sufficiently high in resolution to determine finer-scale trends in temperature in the duration recorded by the flowstone (1.8374 Ma to 1.5377 Ma). Thus, it is difficult to determine if temperature increased throughout speleothem growth, or if temperature decreased, then increased.

If temperature has risen monotonically throughout this interval, then it is likely that the interpreted initial decrease in weathering rate between 1.8374 Ma and 1.7074 Ma is the result of increasing aridity and/or changing ecosystem. Alternatively, if temperature initially decreased as the landscape became more arid, then increased afterwards, then the temporal variation in chemical weathering observed with speleothem $^{10}Be/^{9}Be$ could be partially or entirely driven by temperature.

An alternative explanation for the increase in $^{10}Be/^{9}Be$ during the 1.8 to 1.7 Ma interval is a change in the distribution of roots with depth in the soil, rather than a change in chemical weathering rate. Moore et al. (2021) measure ^{10}Be and ^{9}Be concentrations in soil as well as the roots and leaves of four deciduous tree species and find that trees source beryllium from the soil, drawing it up in their roots. If the $^{10}Be/^{9}Be$ ratio varies with depth in the soil above the cave, then a change in the distribution of roots with depth in the soil could change the $^{10}Be/^{9}Be$ ratio of the biomass. If the speleothem is receiving its beryllium primarily from soil-derived organic colloids (a hypothesis that requires examination), then a change in rooting depth could impact the $^{10}Be/^{9}Be$ ratio recorded in the flowstone. Nevertheless, February & Higgins (2010) find similar depth-distributions of fine tree and grass roots in the Kruger National Park savanna in South Africa. This suggests that this explanation is unlikely, although it is possible that rooting depths are different in the thin-soiled dolomite bedrock at Buffalo Cave.

Conclusion

The Be-isotope data from Buffalo Cave indicate that chemical weathering likely decreased between 1.8374 Ma and 1.7074 Ma, and could have increased slightly between 1.7074 Ma and 1.5377 Ma. Without a detailed proxy for temperature, it is difficult to assess the relative roles of temperature, rainfall/aridity, and shifting ecosystem in driving these changes. Nevertheless, the alignment of the $^{10}Be/^{9}Be$ signal with stable isotope variation illustrates a possible relationship between climate, ecosystem, and chemical weathering. There are ample opportunities for future research in beryllium sources and mobility in this landscape.

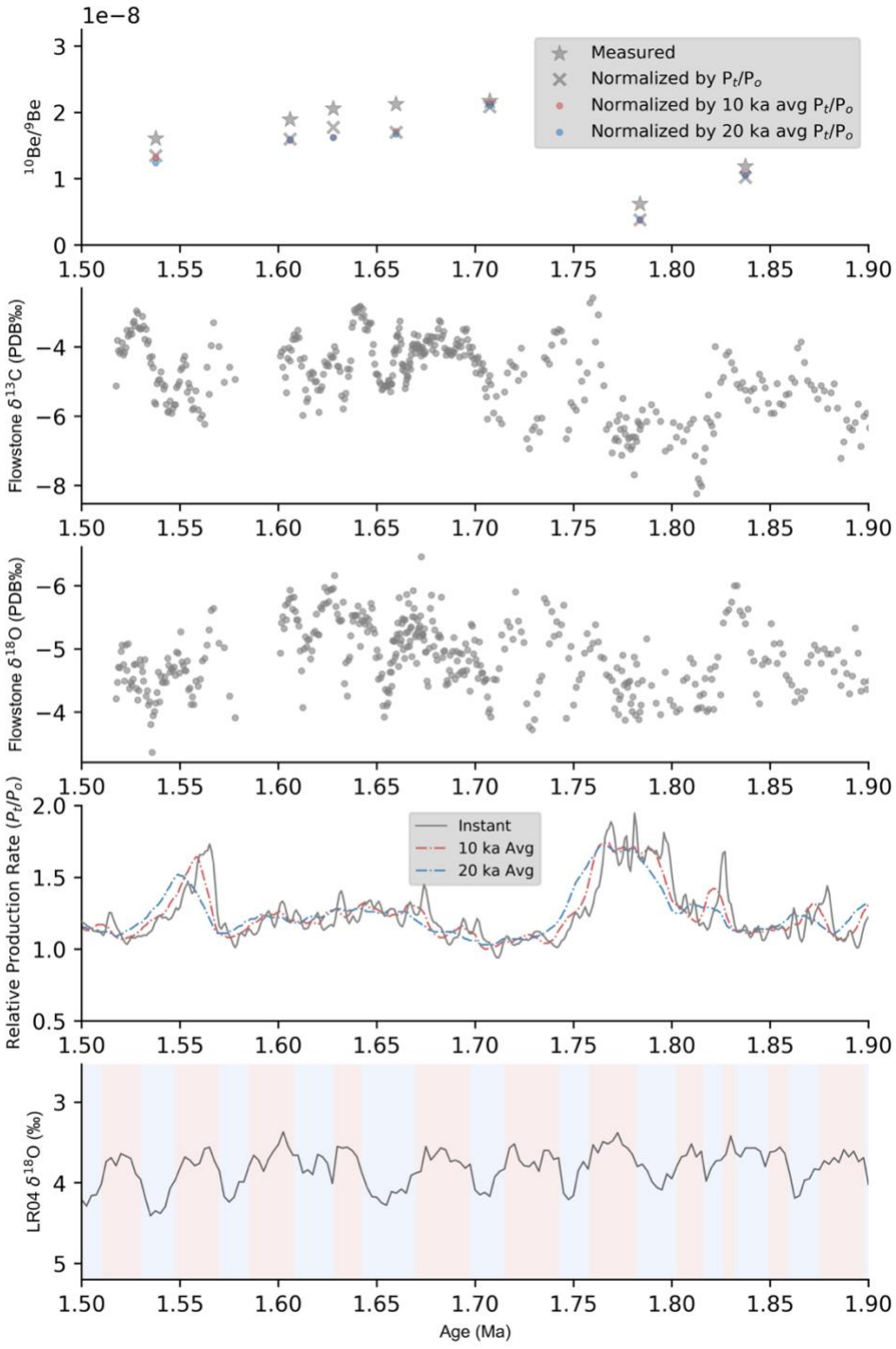

Figure A1.1: Data from Buffalo Cave flowstone. Flowstone oxygen and carbon isotopes from Hopley et al. (2007). Benthic stack oxygen isotopes from Lisiecki & Raymo, 2005. Relative ^{10}Be atmospheric production rate calculated using geomagnetic field intensity, following the same method outlined in chapter 2 of this thesis. 10 ka and 20 ka averaging times are for sake of discussion, and are not based on soil residency time of beryllium. $^{10}Be/^{9}Be$ ratio corrected for decay since speleothem formation. Uncertainties on the $^{10}Be/^{9}Be$ ratio are analytical and 1-sigma. Shaded time intervals represent odd (red) and even (blue) marine isotope stages.

APPENDIX 2: MN-OXIDES FROM THE APPALACHIANS

In addition to speleothems, I explored terrestrial manganese oxides as archives of beryllium isotopes in groundwater. In the marine setting, the utility of manganese oxides as records of beryllium isotopes is well established (as I discuss in chapter 1). However, to my knowledge $^{10}Be/^{9}Be$ in terrestrial manganese oxides is yet to be explored.

I sought to evaluate the usage of Be-isotopes in manganese oxides as a dating tool, using the decay of ^{10}Be after oxide precipitation as a chronometer. I measured ^{10}Be and ^{9}Be in Mn-oxides collected by Odom (2020) from the southern and central Appalachians. Odom (2020) painstakingly separated cryptomelane, a K-bearing manganese oxide, from Mn oxides and determined mineral ages via $^{40}Ar/^{39}Ar$ geochronology. The difficulty of this technique demonstrates the need for a less labor intensive chronometer for Mn-oxides.

In order to use Be-isotopes as a chronometer in Mn-oxides, two conditions must be met:

1) The Mn-oxides act must as a closed-system with respect to beryllium, with no loss or addition of Be after precipitation, except for radioactive decay of ^{10}Be.
2) The temporal variations in the $^{10}Be/^{9}Be$ ratio within the groundwater from which the Mn-oxides precipitate must be negligible compared to ^{10}Be decay. (i.e. the time differences between sample ages are long enough such that ^{10}Be decay is the primary control of the $^{10}Be/^{9}Be$ ratio, not variation in groundwater Be-isotopes)

<u>Geologic setting</u>

The origin of manganese oxide deposits in the Appalachians is not well understood and have formed in a variety of morphologies, including concretionary forms such as botryoidal nodules and as the matrix in breccias (Carmichael et al., 2017). I identified two breccia samples that could test the closed vs. open system behavior of beryllium. Sample 12-11-17A from the Gap Mountain Exposure in Virginia has an $^{40}Ar/^{39}Ar$ age of 8.0 ± 0.3 Ma. In contrast, sample 2-16-

18A from Fork Ridge Mine in Virginia has an $^{40}Ar/^{39}Ar$ age of 30.38 ± 0.17 Ma. Additionally, I examined a botryoidal nodule with concentric lamellae from Mine Bank Mine, in Virginia. A breccia from the same site has an $^{40}Ar/^{39}Ar$ age of 8.74 ± 0.13 Ma. I used this sample to test the hypothesis that I could date the ages of the lamellae using Be-isotopes.

Methods

I used a dissecting microscope to look hand-trace lamellae within the botryoidal nodule (sample Nod1). I identified 4 layers that appeared continuous and used a Dremel to carve out a sample from along 3 of the layers. I also used a coring drill bit to sample from the center of the nodule.

Before dissolving the samples, I leached them in 50% HNO_3 for approximately one hour at 99ºC to remove meteoric ^{10}Be that could have been adsorbed to the sample surface. I rinsed the samples in DI water and dried them in an oven.

After the HNO_3 pre-treatment, I dissolved the massed-samples of Mn-oxides (~1 g per sample) in ~30 ml of 50% HCl. I placed the samples in a dry-bath at 99ºC and waited 2 hours until the Mn-oxides were dissolved. I centrifuged to separate insoluble materials (including quartz and other silicates) and took an aliquot of the solution for measurement of ^{9}Be.

I spiked the remaining solution with Be-carrier (~250 µg of Be added) for AMS measurement of ^{10}Be. After homogenizing the solution, I centrifuged once again, and pipetted off the solution into a fresh centrifuge tube. I dried the remaining residue and re-measured the mass in order to determine the mass of insoluble materials.

In the new centrifuge tube I precipitated Mn, Fe, and Ti at high pH (~14) by adding 10ml of 50% NaOH and centrifuged to separate the beryllium (in the supernatant) from the Mn, Fe, and Ti. I precipitated the beryllium from the supernatant by adjusting the pH to 7 with ~3 ml of HCl and several drops of NaOH. After several rinses of the beryllium precipitate, I dissolved the beryllium gel in 10 ml of 0.4 M oxalic acid and proceeded with cation column chemistry, as outlined for the speleothem samples in Appendix 4.

I measured ^{9}Be in the aliquots via ICP-OES. Samples and standards were prepared in 5% HCl. The calibration curve was made using a 0ppm standard and 1.922 ppm standard. I measured intensity on the 313.107 nm line, since the HCl matrix could interfere with the 313.042 nm line (Cl) and since Fe could raise the intensity of the 234.861 nm line.

Table A2.1: Beryllium isotope data from Mn-oxides

Sample	**^{10}Be/^{9}Be measured**	**±**	**Ar/Ar age (Odom, 2020)**	**Site**	**Morphology**
Nod1-L1 (rim)	2.437E-11	1.694E-12	8.74 ± 0.13 Ma (from breccia at same site)	Mine Bank Mine, VA	Botryoidal Nodule
Nod1-L2B	2.608E-11	1.791E-12	8.74 ± 0.13 Ma (from breccia at same site)	Mine Bank Mine, VA	Botryoidal Nodule
Nod1-L3	8.902E-11	6.548E-12	8.74 ± 0.13 Ma (from breccia at same site)	Mine Bank Mine, VA	Botryoidal Nodule
Nod1-C1 (core)	1.876E-11	1.319E-12	8.74 ± 0.13 Ma (from breccia at same site)	Mine Bank Mine, VA	Botryoidal Nodule
12-11-17A	2.305E-11	1.610E-12	8.0 ± 0.3 Ma	Gap Mountain Exposure, VA	Breccia
2-16-18A	9.651E-11	6.006E-12	30.38 ± 0.17 Ma	Fork Ridge Mine, VA	Breccia

Results

The ^{10}Be/^{9}Be ratio does not systematically vary with radial distance from the core of the botryoidal manganese nodeule (Nod1). The lowest measured Be-isotope ratio is at the core of the nodule, while the highest ^{10}Be/^{9}Be ratio is the sample closest to the core sample. Both samples 12-11-17A and 2-16-18A, which come from the matrix in breccias, contain appreciable concentrations of ^{10}Be.

Discussion

Despite the wide range of $^{40}Ar/^{39}Ar$ ages of the cryptomelane in these samples (from approximately 8 to 30.38 Ma), all of the samples have $^{10}Be/^{9}Be$ ratios of the same order of magnitude (10^{-11}). The $^{40}Ar/^{39}Ar$ age of sample 2-16-18A (30.38 Ma) is equivalent to more than 22 half-lives of ^{10}Be in age. The measurable ^{10}Be within the sample thus suggests that it has not been a closed-system with respect to Be-isotopes, and that ^{10}Be must have been added since the original formation of the cryptomelane.

There are two possible explanations that could explain the discrepancy between the $^{40}Ar/^{39}Ar$ age and the $^{10}Be/^{9}Be$ ratio. Firstly, the cryptomelane could be a different age than other phases within samples. Cross-cutting relationships in the texture of the botryoidal nodule (Figure A2.1, sample Nod1) could represent multiple generations of Mn-oxide and Fe-oxide growth and recrystallization within the nodule. The second explanation could be a laboratory issue. When the BeOH from the samples was drying in quartz vials on the heating block, one sample splattered. This could have cross-contaminated the other samples. However, the blank from the same batch of samples did not have an elevated $^{10}Be/^{9}Be$ ratio on the AMS, so this explanation seems unlikely.

Conclusion

Beryllium isotopes in terrestrial manganese oxides from the Appalachians do not follow closed system behavior. It is likely that these deposits have undergone multiple intervals of growth spaced out appreciably in time. Further work should examine whether $^{10}Be/^{9}Be$ varies in different phases within the Mn-oxides. For instance, if $^{10}Be/^{9}Be$ varies with the Fe/(Fe+Mn) ratio, or within specific mineral separates.

Figure A2.1: Sample NOD1: a botryoidal Mn-oxide nodule from Mine Bank Mine, VA. Traced layers are visible in pencil markings. NOD1-C1 is a drilled-out core from the center of the nodule. NOD1-L3, NOD1-L2b, and NOD1-L1 are layers that are further out from the core. NOD1-L1 is the rim. Note the oxidized iron near the center of the nodule, and the shiny erratic layers near the center that appear to cross-cut the concentric lamellae. These could imply that alteration has occurred after the initial precipitation of the nodule.

APPENDIX 3: DERIVATION OF THE WEATHERING RATE EQUATIONS

Weathering rates with multiple pools of ^{9}Be within the parent material

In order to expand the weathering equation out for multiple weathering minerals, let us consider a parent material containing three mineral phases, each with their own ^{9}Be concentrations, and each with their own weathering rates and weathering congruencies.

In this scenario, the concentration of ^{9}Be within the parent, $[\,^{9}Be]_p$ is based on the relative abundances of each phase within the parent material. Therefore:

$$[\,^{9}Be]_p = [\,^{9}Be]_1 \alpha_1 + [\,^{9}Be]_2 \alpha_2 + [\,^{9}Be]_3 \alpha_3$$

(Eq. A3.1)

$[\,^{9}Be]_1$ = Concentration of 9Be within phase 1 in the parent
α_1 = Fraction of parent material that is phase 1
α_2 = Fraction of parent material that is phase 2
α_3 = Fraction of parent material that is phase 3
Note, $1 = \alpha_1 + \alpha_2 + \alpha_3$

Next, let us assume that the total denudation rate is the sum of the denudation rates of each of the three phases that make up the parent material. Therefore:

$$D_{total} = D_1 + D_2 + D_3$$
(Eq. A3.2)

D_1 = Denudation rate of phase 1

D_2 = Denudation rate of phase 2

D_3 = Denudation rate of phase 3

Thus,

$$D_{total}\left[{}^{9}Be\right]_p = D_{total} \times \left\{\left[{}^{9}Be\right]_1 \alpha_1 + \left[{}^{9}Be\right]_2 \alpha_2 + \left[{}^{9}Be\right]_3 \alpha_3\right\}$$

(Eq. A3.3)

Since the total denudation rate multiplied by the abundance of a given phase in the parent material equals the phase-specific denudation rate (ie. $D_{total} \times \alpha_1 = D_1$), we can further simplify this equation:

$$D_{total}\left[{}^{9}Be\right]_p = \left[{}^{9}Be\right]_1 D_1 + \left[{}^{9}Be\right]_2 D_2 + \left[{}^{9}Be\right]_3 D_3$$

(Eq. A3.4)

Therefore, we can replace the $D_{total}\left[{}^{9}Be\right]_p$ term in equation 2.2.9 in chapter 2 with this phase-specific term in equation A3.4:

$$D\left[{}^{9}Be\right]_p = E\,\gamma_{min}\left[{}^{9}Be\right]_{min'} + \frac{\left[{}^{9}Be\right]_{reac}}{\left[{}^{10}Be\right]_{reac}} F_{met}^{{}^{10}Be}$$

(Eq. A3.5)

(Eq. 2.2.9 from chapter 2, derived from von Blanckenburg et al., 2012)

$$\left[{}^{9}Be\right]_1 D_1 + \left[{}^{9}Be\right]_2 D_2 + \left[{}^{9}Be\right]_3 D_3 = E\,\gamma_{min}\left[{}^{9}Be\right]_{min'} + \frac{\left[{}^{9}Be\right]_{\boldsymbol{reac}}}{\left[{}^{10}Be\right]_{\boldsymbol{reac}}} F_{met}^{{}^{10}Be}$$

(Eq. A3.6)

By splitting the total denudation rate into phase-specific denudation rates, we are therefore assuming that each phase has its own values for W_{diss}, E_{reac}, and E_{min}, since $D = W_{diss} + E_{reac} + E_{min}$.

Therefore, the total mineral erosion rate is equal to the sum of each of the phase-specific mineral erosion rates:

$$E_{min} = E_{min,1} + E_{min,2} + E_{min,3}$$

(Eq. A3.7)

Looking again at equation x from the section above, we can break the $E\ \gamma_{min}\left[\ ^{9}Be\right]_{min'}$ term into phase-specific terms. Firstly, we can simply the term:

Since $E\ \times\ \gamma_{min} = E_{min}$

Therefore,

$$E\ \gamma_{min}\left[\ ^{9}Be\right]_{min'} = E_{min}\ \left[\ ^{9}Be\right]_{min'}$$

(Eq. A3.8)

Next, we can break the fraction of sediment in the mineral pool (γ_{min}) into phase-specific fractions:

$$\gamma_{min} = \gamma_{min,1} + \gamma_{min,2} + \gamma_{min,3}$$

(Eq. A3.9)

It is important to note that these phase-fractions of the mineral phase do not have to add up to one:

$$\gamma_{min,1} + \gamma_{min,2} + \gamma_{min,3} \leq 1$$

(Eq. A3.10)

If they do sum to 1, it implies that there is no secondary materials forming, and that eroding material is entirely from the 'min' pool, since $\gamma_{min} + \gamma_{reac} = 1$.

In this formulation, the fraction of the 'min' sediment pool from phase 1 is:

$$Fraction\ of\ \ 'min'\ pool\ from\ phase\ 1 = \frac{\gamma_{min,1}}{\gamma_{min,1}+\gamma_{min,2}+\gamma_{min,3}} = \frac{\gamma_{min,1}}{\gamma_{min}}$$

(Eq. A3.11)

Thus, $1 = \frac{\gamma_{min,1}}{\gamma_{min}} + \frac{\gamma_{min,2}}{\gamma_{min}} + \frac{\gamma_{min,3}}{\gamma_{min}}$

(Eq. A3.12)

Therefore, the total concentration of ^{9}Be in the mineral pool, $\left[\ ^{9}Be\right]_{min'}$, can be expressed by multiplying these phase-specific fractions of the mineral pool by the ^{9}Be concentration in each respective phase:

$$\left[\ ^{9}Be\right]_{min'} = \left[\ ^{9}Be\right]_{min',1} \times \frac{\gamma_{min,1}}{\gamma_{min}} + \left[\ ^{9}Be\right]_{min',2} \times \frac{\gamma_{min,2}}{\gamma_{min}} + \left[\ ^{9}Be\right]_{min',3} \times \frac{\gamma_{min,3}}{\gamma_{min}}$$

(Eq. A3.13)

Returning to equation A3.6, derived from von Blanckenburg et al. (2012), we can now substitute in this phase-specific formulation of $\left[\ ^{9}Be\right]_{min'}$:

$$\left[\ ^{9}Be\right]_{1} D_1 + \left[\ ^{9}Be\right]_{2} D_2 + \left[\ ^{9}Be\right]_{3} D_3 = E_{min} \times \left\{\left[\ ^{9}Be\right]_{min',1} \times \frac{\gamma_{min,1}}{\gamma_{min,1}+\gamma_{min,2}+\gamma_{min,3}} + \left[\ ^{9}Be\right]_{min',2} \times \frac{\gamma_{min,2}}{\gamma_{min,1}+\gamma_{min,2}+\gamma_{min,3}} + \left[\ ^{9}Be\right]_{min',3} \times \frac{\gamma_{min,3}}{\gamma_{min,1}+\gamma_{min,2}+\gamma_{min,3}}\right\} + \frac{\left[\ ^{9}Be\right]_{\boldsymbol{reac}}}{\left[^{10}Be\right]_{\boldsymbol{reac}}} F_{met}^{\ ^{10}Be}$$

(Eq. A3.14)

The erosion rate of a given phase within the mineral pool is equivalent to the product of the total E_{min} and the specific phase's fractional abundance in the min pool. For example:

$$E_{min,1} = E_{min} \times \frac{\gamma_{min,1}}{\gamma_{min}}$$

(Eq. A3.15)

Therefore, the equation further simplifies to:

$$\left[{}^{9}Be\right]_1 D_1 + \left[{}^{9}Be\right]_2 D_2 + \left[{}^{9}Be\right]_3 D_3 = E_{min,1}\left[{}^{9}Be\right]_{min',1} + E_{min,2}\left[{}^{9}Be\right]_{min',2} + E_{min,3}\left[{}^{9}Be\right]_{min',3} + \frac{\left[{}^{9}Be\right]_{reac}}{\left[{}^{10}Be\right]_{reac}} F_{met}^{{}^{10}Be}$$

(Eq. A3.16)

Finally, we must assume that the concentration of ^{9}Be in each phase within the parent is the same as the ^{9}Be concentration of the same phase within the 'min' pool:

Assuming

$$\left[{}^{9}Be\right]_1 = \left[{}^{9}Be\right]_{min',1}$$

$$\left[{}^{9}Be\right]_2 = \left[{}^{9}Be\right]_{min',2}$$

$$\left[{}^{9}Be\right]_3 = \left[{}^{9}Be\right]_{min',3}$$

As I discuss above, this assumption means that the mineral pool is entirely composed of primary minerals from the parent material, and that the reactive pool is composed entirely of secondary materials that form in isotopic equilibrium with the dissolved phase. Therefore, this assumes that there is no pool of unreactive secondary materials.

Given this assumption, the equation simplifies further:

$$\left[{}^{9}Be\right]_1\left(D_1 - E_{min,1}\right) + \left[{}^{9}Be\right]_2\left(D_2 - E_{min,2}\right) + \left[{}^{9}Be\right]_3\left(D_3 - E_{min,3}\right) = \frac{\left[{}^{9}Be\right]_{reac}}{\left[{}^{10}Be\right]_{reac}} F_{met}^{{}^{10}Be}$$

(Eq. A3.17)

Since $D - E_{min} = W_p$, this equation can finally be rewritten as:

$$\frac{\left[{}^{10}Be\right]_{reac}}{\left[{}^{9}Be\right]_{reac}} = \frac{F_{met}^{{}^{10}Be}}{\left[{}^{9}Be\right]_1 W_{p,1} + \left[{}^{9}Be\right]_2 W_{p,2} + \left[{}^{9}Be\right]_3 W_{p,3}}$$

(Eq. A3.18)

This equation demonstrates that, if there are phases within the parent material that have different ^{9}Be concentrations, then the measured ^{10}Be/^{9}Be ratio represents the sum of the W_p weathering rates of each phase in the parent material, weighted by their ^{9}Be concentrations:

$$\frac{[^{10}Be]_{reac}}{[^{9}Be]_{reac}} = \frac{F_{met}^{^{10}Be}}{\sum_{x=1}^{n}[^{9}Be]_x W_{p,x}}$$

(Eq. A3.19)

n = Number of phases in the parent material

$\left[{}^{9}Be \right]_x$ = Concentration of ^{9}Be in phase x

$W_{p,x}$ = Weathering rate of phase x

If a phase "x" does not contain ^{9}Be (ie. $\left[{}^{9}Be \right]_x = 0$), or if a phase does not chemically weather (ie. $W_{p,x} = 0$), then that phase will drop out of the equation. For example, if the parent material was composed of only quartz and feldspar, a total W_p could still be determined since quartz typically has a relatively negligible ^{9}Be concentration, and since the quartz chemical weathering rate is likely to be negligible while feldspar still remains in the weathering zone.

The phase-specific W_p terms can also be re-written if we define phase-specific weathering congruencies:

$$C_x = \frac{W_{diss,x}}{W_{diss,x} + E_{reac,x}}$$

(Eq. A3.20)

C_x = Weathering congruency of phase x from the parent

$W_{diss,x}$ = Weathering rate (chemical erosion rate) of phase x

$E_{reac,x}$ = Erosion rate of reactive phases produced from chemical weathering of phase x in the parent. In steady-state, this is equivalent to the rate of secondary phase formation from parent phase x.

$$\frac{[^{10}Be]_{reac}}{[^{9}Be]_{reac}} = \frac{F_{met}^{^{10}Be}}{\sum_{x=1}^{n}[^{9}Be]_{x}\frac{W_{diss,x}}{C_x}}$$

(Eq. A3.21)

Weathering rates with dust as the parent material, and no addition from bedrock

Here I derive weathering rate equations for a landscape in which the weathering parent material is entirely derived from dust, with no bedrock input. I assume the dust contains both mineral and reactive phases.

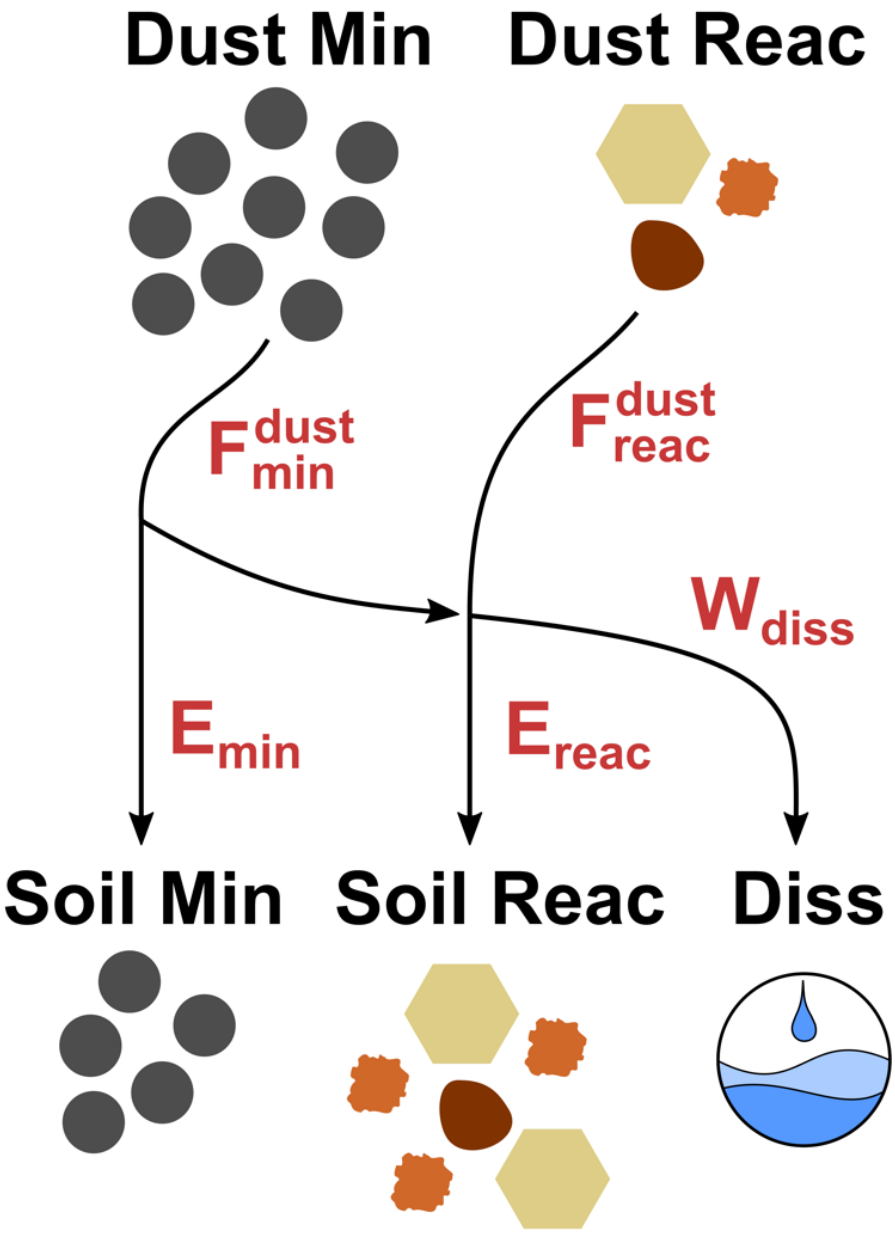

Figure A3.1: Weathering pools and fluxes with dust

First we will define a landscape dust flux, F^{dust} in g/cm^2/yr. The dust contains both a reactive and mineral pool each with their own ^{10}Be and ^{9}Be concentrations. The dust flux can therefore be broken down into a flux of reactive phases (F_{reac}^{dust}) and a flux of weatherable primary minerals in the 'min' phase (F_{min}^{dust}). Like in the previous derivations, the mass of material entering the system must equal the mass leaving. However, instead of bedrock supplying mass via a

denudation rate, here mass is supplied by dust flux. Therefore, conservation of mass can be expressed in the following manner:

$$F^{dust} = E_{min} + E_{reac} + W_{diss}$$

or alternatively,

$$F_{min}^{dust} + F_{reac}^{dust} = E_{min} + E_{reac} + W_{diss}$$

(Eq. A3.22)

However, in this case chemical weathering of the min pool is not the only contributor to the reactive and dissolved pools, since there is a flux of reactive phases from the incoming dust. Therefore we must revise our definition of W_p :

$$E_{reac} + W_{diss} \neq W_p$$

$$F_{min}^{dust} - E_{min} = W_p$$

$$E_{reac} + W_{diss} - F_{reac}^{dust} = W_p$$

(Eq. A3.23)

Since the mineral pool does not contain ^{10}Be, the total flux of ^{10}Be into the system is the sum of the primary ^{10}Be flux from rain and the ^{10}Be contribution from reactive phases in the dust.

$$^{10}Be\ flux\ into\ the\ soil = F_{met}^{^{10}Be} + \left[^{10}Be\right]_{reac}^{dust} \times F^{dust}$$

(Eq. A3.24)

On the other hand, ^{9}Be resides within both the reactive and mineral pools in the dust. With no bedrock input, the total ^{9}Be flux into the soil is the sum of these two pools.

$$^{9}Be\ flux\ into\ the\ soil = F^{dust} \times \left(\left[\,^{9}Be\right]_{min}^{dust} + \left[\,^{9}Be\right]_{reac}^{dust}\right)$$

(Eq. A3.25)

In the equations above, the ^{10}Be and ^{9}Be concentrations in the dust are expressed in the units that are defined by von Blanckenburg et al (2012). For instance, $\left[{}^{10}Be\right]_{reac}^{dust}$ is equal to atoms of ^{10}Be in the reactive pool of dust per gram of total dust. $\left[\ {}^{9}Be\right]_{min}^{dust}$ is equal to atoms of ^{9}Be in the mineral pool of dust per gram of total dust.

The flux of ^{10}Be and ^{9}Be out of the soil can then be defined based on their concentrations within the soil reactive and mineral pools, as well as the dissolved pool.

$$^{10}Be\ flux\ out\ of\ the\ soil = \ E\left[{}^{10}Be\right]_{reac}^{soil} + Q\left[{}^{10}Be\right]_{diss}$$

(Eq. A3.26)

$$^{9}Be\ flux\ out\ of\ the\ soil = \ E\left(\left[\ {}^{9}Be\right]_{reac}^{soil} + \left[\ {}^{9}Be\right]_{min}^{soil}\right) + Q\left[\ {}^{9}Be\right]_{diss}$$

(Eq. A3.27)

In steady-state, the flux of beryllium isotopes into the soil will equal the flux out. Therefore, we can set the fluxes equal to one another:

$$E\left(\left[\ {}^{9}Be\right]_{reac}^{soil} + \left[\ {}^{9}Be\right]_{min}^{soil}\right) + Q\left[\ {}^{9}Be\right]_{diss} = \ F^{dust}\left(\left[\ {}^{9}Be\right]_{min}^{dust} + \left[\ {}^{9}Be\right]_{reac}^{dust}\right)$$

(Eq. A3.28)

Recalling the definition of K_d from von Blanckenburg et al. (2012), we can re-write the $Q\left[\ {}^{9}Be\right]_{diss}$ term as $\frac{Q}{K_d}\left[\ {}^{9}Be\right]_{reac}^{soil}$ since $K_d = \frac{[Be]_{reac}}{[Be]_{diss}}$:

$$E\left(\left[\ {}^{9}Be\right]_{reac}^{soil} + \left[\ {}^{9}Be\right]_{min}^{soil}\right) + \frac{Q}{K_d}\left[\ {}^{9}Be\right]_{reac}^{soil} = \ F^{dust}\left(\left[\ {}^{9}Be\right]_{min}^{dust} + \left[\ {}^{9}Be\right]_{reac}^{dust}\right)$$

(Eq. A3.29)

Now we can set the ^{10}Be fluxes equal to one another in a similar way:

$$E\left[{}^{10}Be\right]_{reac}^{soil} + Q\left[{}^{10}Be\right]_{diss} = F_{met}^{{}^{10}Be} + \left[{}^{10}Be\right]_{reac}^{dust} \times F^{dust}$$

(Eq. A3.30)

Once again recalling the definition of K_d, the equation can be rewritten as:

$$\left(E + \frac{Q}{K_d}\right)\left[{}^{10}Be\right]_{reac}^{soil} = F_{met}^{{}^{10}Be} + \left[{}^{10}Be\right]_{reac}^{dust} \times F^{dust}$$

(Eq. A3.31)

By solving this equation for $\frac{Q}{K_d}$, the entire ^{10}Be steady-state equation can replace the $\frac{Q}{K_d}$ term in the ^{9}Be steady state equation above. Combined, these two equations take the following form:

$$\left(\frac{{}^{10}Be}{{}^{9}Be}\right)_{reac}^{soil} = \frac{F_{met}^{{}^{10}Be} + F^{dust}\left[{}^{10}Be\right]_{reac}^{dust}}{F^{dust}\left(\left[{}^{9}Be\right]_{min}^{dust} + \left[{}^{9}Be\right]_{reac}^{dust}\right) - E\left[{}^{9}Be\right]_{min}^{soil}}$$

(Eq. A3.32)

Similar to the previous derivations, we can break the dust into fractions:

$$1 = \gamma_{min}^{dust} + \gamma_{reac}^{dust}$$

(Eq. A3.33)

γ_{min}^{dust} = Fraction of the incoming dust that is primary mineral phases

γ_{reac}^{dust} = Fraction of the incoming dust that is secondary reactive phases

Therefore, the total dust flux can be broken into separate fluxes of the reactive and mineral pools by multiplying by the flux fractions:

$$F^{dust} = F_{reac}^{dust} + F_{min}^{dust} = \gamma_{reac}^{dust} F^{dust} + \gamma_{min}^{dust} F^{dust}$$

(Eq. A3.34)

Since so far we've defined the beryllium concentrations in the manner of von Blanckenburg et al. (2012), we can use these fractions to convert the concentrations to more useful units, similar to what we did in the previous derivations:

$$\left[{}^{9}Be \right]_{min\prime}^{dust} = \frac{\left[{}^{9}Be \right]_{min}^{dust}}{\gamma_{min}^{dust}}$$

(Eq. A3.35)

$\left[{}^{9}Be \right]_{min}^{dust}$ = atoms of ^{9}Be in the mineral pool of the dust / g of total dust

$\left[{}^{9}Be \right]_{min\prime}^{dust}$ = atoms of ^{9}Be in the mineral pool of the dust / g of mineral material in the dust

Likewise, the concentration of beryllium within the reactive pool of dust per gram of reactive material is therefore:

$$\left[{}^{9}Be \right]_{reac\prime}^{dust} = \frac{\left[{}^{9}Be \right]_{reac}^{dust}}{\gamma_{reac}^{dust}}$$

(Eq. A3.36)

$\left[{}^{9}Be \right]_{reac}^{dust}$ = atoms of ^{9}Be in the mineral pool of the dust / g of total dust

$\left[{}^{9}Be \right]_{reac}^{dust}$ = atoms of ^{9}Be in the mineral pool of the dust / g of mineral material in the dust

Therefore, we can break down the $\left[{}^{9}Be \right]_{min}^{dust} + \left[{}^{9}Be \right]_{reac}^{dust}$ term in the denominator of equation A3.32 above in the following manner:

$$\left(\frac{{}^{10}Be}{{}^{9}Be} \right)_{reac}^{soil} = \frac{F_{met}^{{}^{10}Be} + F^{dust} \left[{}^{10}Be \right]_{reac}^{dust}}{F^{dust} \left(\gamma_{min}^{dust} \left[{}^{9}Be \right]_{min\prime}^{dust} + \gamma_{reac}^{dust} \left[{}^{9}Be \right]_{reac\prime}^{dust} \right) - E \left[{}^{9}Be \right]_{min}^{soil}}$$

(Eq. A3.37)

Distributing the F^{dust} term then breaks the dust flux into the mineral and reactive dust fluxes:

$$\left(\frac{^{10}Be}{^{9}Be}\right)_{reac}^{soil} = \frac{F_{met}^{^{10}Be} + F^{dust}[^{10}Be]_{reac}^{dust}}{F_{min}^{dust}[\,^{9}Be]_{min'}^{dust} + F_{reac}^{dust}[\,^{9}Be]_{reac'}^{dust} - E[\,^{9}Be]_{min}^{soil}}$$

(Eq. A3.38)

We can use similar conversions for the soil concentrations. We can break the soil into fractions in the mineral and reactive pools:

$$1 = \gamma_{min}^{soil} + \gamma_{reac}^{soil}$$

(Eq. A3.39)

γ_{min}^{soil} = Fraction of the soil that is primary mineral phases

γ_{reac}^{soil} = Fraction of the soil that is secondary reactive phases

Thus, we arrive at the following definitions for soil beryllium concentrations:

$$[\,^{9}Be]_{min'}^{soil} = \frac{[\,^{9}Be]_{min}^{soil}}{\gamma_{min}^{soil}}$$

(Eq. A3.40)

$[\,^{9}Be]_{min}^{soil}$ = atoms of ^{9}Be in the mineral pool of the soil / g of total soil

$[\,^{9}Be]_{min'}^{soil}$ = atoms of ^{9}Be in the mineral pool of the soil / g of mineral material in the soil

Therefore, the $[\,^{9}Be]_{min}^{soil}$ term in the denominator can also converted similar to how we converted the dust flux fractions:

$$\left(\frac{^{10}Be}{^{9}Be}\right)_{reac}^{soil} = \frac{F_{met}^{^{10}Be} + F^{dust}[^{10}Be]_{reac}^{dust}}{F_{min}^{dust}[\,^{9}Be]_{min'}^{dust} + F_{reac}^{dust}[\,^{9}Be]_{reac'}^{dust} - E \times \gamma_{min}^{soil} \times [\,^{9}Be]_{min'}^{soil}}$$

(Eq. A3.41)

The total erosion rate can then broken into separate fluxes of the reactive and mineral pools by multiplying by the flux fractions:

$$E = E_{reac} + E_{min} = E\,\gamma_{reac}^{soil} + E\,\gamma_{min}^{soil}$$

(Eq. A3.42)

Thus, the equation above simplifies to:

$$\left(\frac{^{10}Be}{^{9}Be}\right)_{reac}^{soil} = \frac{F_{met}^{^{10}Be} + F^{dust}[^{10}Be]_{reac}^{dust}}{F_{min}^{dust}[\,^{9}Be]_{min'}^{dust} + F_{reac}^{dust}[\,^{9}Be]_{reac'}^{dust} - E_{min}[\,^{9}Be]_{min'}^{soil}}$$

(Eq. A3.43)

Next, we can replace the $[^{10}Be]_{reac}^{dust}$ term in the numerator in a similar manner to the ^{9}Be concentrations, using the γ_{reac}^{dust} term to convert the units.

$$[^{10}Be]_{reac'}^{dust} = \frac{[^{10}Be]_{reac}^{dust}}{\gamma_{reac}^{dust}}$$

(Eq. A3.44)

$[^{10}Be]_{reac}^{dust}$ = atoms of ^{10}Be in the reac pool of dust / g of total dust

$[^{10}Be]_{reac'}^{dust}$ = atoms of ^{9}Be in the reac pool of dust / g of reactive phases in dust

Therefore:

$$\left(\frac{^{10}Be}{^{9}Be}\right)^{soil}_{reac} = \frac{F_{met}^{^{10}Be} + F^{dust} \times \gamma_{reac}^{dust} \times [^{10}Be]_{reac\prime}^{dust}}{F_{min}^{dust}[\,^{9}Be]_{min\prime}^{dust} + F_{reac}^{dust}[\,^{9}Be]_{reac\prime}^{dust} - E_{min}[\,^{9}Be]_{min\prime}^{soil}}$$

(Eq. A3.45)

And since $F^{dust} \times \gamma_{reac}^{dust} = F_{reac}^{dust}$ the equation further simplifies to:

$$\left(\frac{^{10}Be}{^{9}Be}\right)^{soil}_{reac} = \frac{F_{met}^{^{10}Be} + F_{reac}^{dust}\,[^{10}Be]_{reac\prime}^{dust}}{F_{min}^{dust}[\,^{9}Be]_{min\prime}^{dust} + F_{reac}^{dust}[\,^{9}Be]_{reac\prime}^{dust} - E_{min}[\,^{9}Be]_{min\prime}^{soil}}$$

(Eq. A3.46)

Now, like in the previous derivations, we will assume that the concentration of ^{9}Be within the mineral phase in the soil is the same as the concentration within the mineral phase of the dust. Once again, this assumption will be valid if there is a homogeneous distribution of ^{9}Be across all mineral phases in the dust. However, if the 'min' pool contains various minerals with different ^{9}Be concentrations and weathering rates, this assumption will be violated. However, much like the previous derivation, we can break this equation down into phase-specific weathering rates.

Given the assumption that $[\,^{9}Be]_{min\prime}^{dust} = [\,^{9}Be]_{min\prime}^{soil}$, the equation can be rewritten as:

$$\left(\frac{^{10}Be}{^{9}Be}\right)^{soil}_{reac} = \frac{F_{met}^{^{10}Be} + F_{reac}^{dust}\,[^{10}Be]_{reac\prime}^{dust}}{[\,^{9}Be]_{min\prime}^{dust}(F_{min}^{dust} - E_{min}) + F_{reac}^{dust}[\,^{9}Be]_{reac\prime}^{dust}}$$

(Eq. A3.47)

Next, since $W_p = F_{min}^{dust} - E_{min}$, the equation simplifies to:

$$\left(\frac{^{10}Be}{^{9}Be}\right)^{soil}_{reac} = \frac{F_{met}^{^{10}Be} + F_{reac}^{dust}\,[^{10}Be]_{reac\prime}^{dust}}{[\,^{9}Be]_{min\prime}^{dust} W_p + F_{reac}^{dust}[\,^{9}Be]_{reac\prime}^{dust}}$$

(Eq. A3.48)

With this equation, we can see that the W_p weathering rate can be determined, but we still require a lot of information. Not only do we need to measure a $^{10}Be/^{9}Be$ ratio and ^{9}Be concentration within the mineral phases of the dust, but we must also measure ^{9}Be and ^{10}Be concentrations within the dust reactive pools, and determine the fluxes of total dust, as well as the flux of dust in the reactive pool.

However, if we can assume that the $^{10}Be/^{9}Be$ ratio in the reactive pool of the dust is the same as the $^{10}Be/^{9}Be$ ratio in the reactive pool of the soil, the equation simplifies a great deal.

First, we must recast the $\left[\,{}^{9}Be\right]_{reac'}^{dust}$ term in the denominator in terms of the $^{10}Be/^{9}Be$ ratio:

$$\left[\,{}^{9}Be\right]_{reac'}^{dust} = \frac{\left[{}^{10}Be\right]_{reac'}^{dust}}{\left[{}^{10}Be\right]_{reac'}^{dust} \Big/ \left[\,{}^{9}Be\right]_{reac'}^{dust}}$$

(Eq. A3.49)

Placing this term into the equation, we arrive at:

$$\left(\frac{{}^{10}Be}{{}^{9}Be}\right)_{reac}^{soil} = \frac{F_{met}^{{}^{10}Be} + F_{reac}^{dust}\left[{}^{10}Be\right]_{reac'}^{dust}}{\left[\,{}^{9}Be\right]_{min'}^{dust} W_p + F_{reac}^{dust} \times \frac{\left[{}^{10}Be\right]_{reac'}^{dust}}{\left(\frac{{}^{10}Be}{{}^{9}Be}\right)_{reac}^{dust}}}$$

(Eq. A3.50)

Assuming that $\left(\frac{{}^{10}Be}{{}^{9}Be}\right)_{reac}^{dust} = \left(\frac{{}^{10}Be}{{}^{9}Be}\right)_{reac}^{soil}$ this equation simplifies to:

$$\left(\frac{{}^{10}Be}{{}^{9}Be}\right)_{reac}^{soil} = \frac{F_{met}^{{}^{10}Be}}{\left[\,{}^{9}Be\right]_{min'}^{dust} W_p}$$

(Eq. A3.51)

APPENDIX 4: SPELEOTHEM CHEMISTRY METHODS

Here I describe the step-by-step procedure I took to prepare the speleothem samples for ^{9}Be measurement via ICP-OES, and ^{10}Be measurement via AMS. I include the chemistry data from Soreq Cave as well as the details of ICP-OES measurements in appendix 5.

To summarize, I performed the following steps:

1) Dissolve speleothem
2) Filter solution via centrifuge filter
3) Take archival aliquot for trace element analysis (see appendix 6)
4) Rest of solution undergoes solvent extraction (removes most Ca, keeps Be)
5) Dry down solution after solvent extraction
6) Take up solution in 5% HNO_3
7) Take aliquot of solution for ICP-OES measurement of ^{9}Be
8) Spike the rest of the solution with Be-carrier for AMS measurement
9) Proceed with steps to prepare cathodes for AMS

Sample Preparation:

Cleaning the Sample:

- ☐ If there are sharpie markings on the sample, wipe and soak in ethanol for ~1hr
- ☐ Sonicate the sample in DI water in a centrifuge tube for 1 hour
- ☐ Decant, rinse the sample in DI water, and triple-rinse the centrifuge tube
- ☐ Fill tube to 50 ml of DI water. Add 2 drops of concentrated HNO_3 and let sample sit in the tube for 1 hour
- ☐ Decant, rinse the sample in DI water, and triple-rinse centrifuge tube
- ☐ Dry sample in the oven at 60°C overnight

Dissolution:

Use an Erlenmeyer flask for dissolution of the speleothem samples. The narrow neck prevents splatter, but allows gas to escape.

- ☐ **Mass empty flask** (a 125ml flask works well for 1-5g calcite samples)
- ☐ **Mass flask + calcite**
- ☐ Add 10ml of DI water to the sample
- ☐ Slowly add 1.25ml of concentrated HNO_3 for every 1g of calcite. This will be roughly a stoichiometric 2:1 ratio of NO_3^- to Ca^{2+}. DON'T add all at once.
- ☐ After the reaction slows down, add extra HNO_3 gradually until all the calcite is dissolved.

Filtration:

- ☐ Label a centrifuge filter tube (with 0.22µm filter) with the sample name
- ☐ Label a 50ml centrifuge tube "SAMPLE Filtered"
- ☐ Label a 50ml centrifuge tube "SAMPLE archive"

- ☐ **Record the mass of the empty centrifuge filter tube**
- ☐ **Record the mass of the empty "SAMPLE filtered" tube**
- ☐ Transfer dissolved speleothem into ***centrifuge tube filter*** with a few DI washes
- ☐ Centrifuge at 1000 RPM for 5 minutes
- ☐ Decant into ***"SAMPLE Filtered"*** centrifuge tube
- ☐ Rinse centrifuge filter
- ☐ Centrifuge at 1000 RPM for 5 minutes
- ☐ Decant into ***"SAMPLE Filtered"*** centrifuge tube

- ☐ **Record the mass of the empty "SAMPLE archive" tube**

- ☐ Use a transfer pipette to transfer 1-5ml of solution from the "Filtered" tube into the "archive" tube. This archival aliquot can be used of trace element analysis later.
- ☐ **Record the mass of the "SAMPLE archive" tube with solution**
- ☐ **Record the mass of the "SAMPLE Filtered" tube** after the archival aliquot has been taken
- ☐ Record the approximate volume left in the "SAMPLE Filtered tube. You will need this for a calculation in the next section.

- ☐ Dry the centrifuge filter in the oven overnight. **Record the mass once dry**

Solvent Extraction to Separate Be from Ca:

Required Solutions:

- ☐ Concentrated HNO_3
- ☐ Glacial acetic acid
- ☐ Bromothymol blue
- ☐ NH_4OH (stock solution concentration)
- ☐ Acetylacetone (stock solution concentration)
- ☐ Chloroform (stock solution concentration)
- ☐ 0.5M Na_2-EDTA with NaOH at pH 8
- ☐ 50% HCl
- ☐ Aluminum standard (1000 µg/ml)

Preparing the pH8 0.5M Na_2EDTA solution:

- Mass out 186.1g of Na_2-EDTA powder
- Add Na_2-EDTA to 800ml of H_2O in a 1 liter bottle
- Add NaOH pellets or NaOH solution until pH = 8 (~18-20g of pellets)
- Dilute to 1 liter

Ca & Be separation (Funnel A):

- ☐ Label a centrifuge “SAMPLE chloroform waste”
- ☐ Label a separatory funnel “SAMPLE Funnel A” (a 250ml funnel works well)
- ☐ Label a separatory funnel “SAMPLE Funnel B” (a 125ml funnel works well)
- ☐ Label a savillex vial “SAMPLE clean”

- ☐ Pour sample from “FILTERED” tube into separatory ***funnel A***
- ☐ Add 1ml of glacial acetic acid
- ☐ Add ~10 drops of bromothymol blue
- ☐ Add pH8 0.5M Na_2EDTA solution: **25ml of solution per g of calcite**
- ☐ Add acetylacetone (stock solution concentration) **volume = 0.01 x solution volume (including calculated EDTA volume)**
- ☐ Add NH_4OH until pH = 7 (lime green color)
- ☐ Shake for 15 minutes

- ☐ Add 20ml of chloroform (stock solution concentration)
- ☐ Shake for 5 minutes. **Remember to vent! Gas builds up. Don’t let it explode! You can vent the separatory funnel by holding it upside-down and opening the valve. Do this slowly so liquid doesn’t shoot out from pressure buildup. Point it away from your face/body while doing this.**
- ☐ Set funnel on ring stand and let the chloroform settle to the bottom
- ☐ Remove the stopper
- ☐ Open the valve and pour chloroform into ***funnel B***

- ☐ Add 10ml of chloroform (stock solution concentration) to ***funnel A***
- ☐ Shake for 2 minutes. **Remember to vent!**
- ☐ Set funnel on ring stand and let the chloroform settle to the bottom
- ☐ Remove the stopper

☐ Open the valve and pour chloroform into ***funnel B***

☐ Add 10ml of chloroform (stock solution concentration) to ***funnel A***

☐ Shake for 2 minutes. **Remember to vent!**

☐ Set funnel on ring stand and let the chloroform settle to the bottom

☐ Remove the stopper

☐ Open the valve and pour chloroform into ***funnel B***

Ca & Be separation (Funnel B):

☐ Add 20ml of 50% HCL to ***funnel B***

☐ Shake for 5 minutes

☐ Set funnel on ring stand and let the chloroform settle to the bottom

☐ Remove the stopper

☐ Open the valve and pour chloroform into ***chloroform waste centrifuge tube***

☐ Open the valve and Pour HCl into the ***savillex vial***

☐ Pour the chloroform out of the ***chloroform waste centrifuge tube*** and back into ***funnel B***

☐ Wash the ***chloroform centrifuge tube*** with 10ml of 50% HCl back into ***funnel B***

☐ Shake ***funnel B*** for 2 minutes

☐ Set funnel on ring stand and let the chloroform settle to the bottom

☐ Remove the stopper

☐ Open the valve and pour chloroform into ***chloroform waste centrifuge tube***

☐ Open the valve and Pour HCl into the ***savillex vial***

☐ Pour the chloroform out of the ***chloroform waste centrifuge tube*** and back into ***funnel B***

☐ Wash the ***chloroform waste centrifuge tube*** with 10ml of 50% HCl back into ***funnel B***

☐ Shake ***funnel B*** for 2 minutes

☐ Set funnel on ring stand and let the chloroform settle to the bottom

☐ Remove the stopper

☐ Open the valve and pour chloroform into ***chloroform waste centrifuge tube***

☐ Open the valve and Pour HCl into the ***savillex vial***

Dry Down:

☐ Add 1 ml of 1000 µg/ml aluminum solution to the ***savillex vial***

☐ Add 10 ml of concentrated HNO_3 to make aqua regia

☐ Let sample sit on griddle until dried down

ICP Prep:

☐ Label a 50ml centrifuge tube "SAMPLE AMS"

☐ Label a 15ml centrifuge tube "SAMPLE native"

☐ **Record the mass of the "SAMPLE AMS" tube**

☐ Dissolve the dried sample in the savillex vial with ~3ml of 5% HNO_3

☐ Use a transfer pipette to transfer the solution into the ***"SAMPLE AMS"*** tube

☐ Double-rinse the savillex with 5% HNO_3 once again using the transfer pipette to transfer to the ***"SAMPLE AMS"*** tube

☐ Dilute the ***"SAMPLE AMS"*** tube with 5% HNO_3. The final volume should be ~5 times the mass of calcite that went into the solvent extraction. This will yield 0.2g of calcite per ml of solution.

☐ **Record the mass of the "SAMPLE AMS" tube with sample**

☐ Vortex the "SAMPLE AMS" tube to homogenize the solution

☐ **Record the mass of the empty "SAMPLE native" tube**

☐ Use a transfer pipette to transfer 5ml of solution from the "AMS" tube into the "native" tube

☐ **Record the mass of the "SAMPLE native" tube with solution**

The "native" tube goes to the ICP for ^{9}Be measurement.

---

^{10}Be chemistry with the "AMS" tube fraction:

Required Solutions:

- ☐ Beryllium carrier solution
- ☐ Bromothymol blue
- ☐ NH_4OH (stock solution concentration)
- ☐ 6M (50%) HCl
- ☐ 4.41M (15%) NaOH
- ☐ 0.4M clean oxalic acid
- ☐ 8N HNO_3
- ☐ Ammoniated water
- ☐ 10% Na_2-EDTA solution

Preparing ammoniated water (pH = 7)

- Fill a solution bottle up to 1L
- Add 1 drop of NH_4OH (stock solution concentration)

Spike each sample with Be carrier:

- ☐ Place a clean weigh-boat on the balance and tare
- ☐ Use pipette to add ~250µg of Be (~0.25g of carrier solution with ~1,000 ppm Be). Make sure to record the exact beryllium concentration of the carrier solution!
- ☐ Record the mass of Be carrier added
- ☐ Pour the carrier solution into the "AMS" tube
- ☐ Rinse the weigh boat with some DI water and pour into the "AMS" tube
- ☐ Repeat

pH steps to remove extra calcium:

- ☐ Label a small bottle “SAMPLE Supernatant”
- ☐ Adjust the pH to 8 in the “AMS” tube using NH_4OH with 3 drops of bromothymol blue
- ☐ Vortex and let the solution sit for ~30 minutes to ensure precipitation of beryllium
- ☐ Centrifuge at 3600 RPM for 5 minutes. The precipitate may have difficulty staying together, if this is the case, centrifuge again at a higher RPM and/or for a longer time
- ☐ Decant the supernatant into the “SAMPLE Supernatant” bottle
- ☐ Add a small amount of ammoniated water to the gel. Vortex to break up the gel. Repeat centrifugation and decant.
- ☐ Add 10ml of 6M (50%) HCl to the precipitate in the “AMS” tube
- ☐ Vortex and ensure that the precipitate is completely dissolved
- ☐ Add 21.5ml of 4.41M (15%) NaOH to the “AMS” tube
- ☐ Dilute up to the 35ml mark with deionized water. The solution should now be at pH = 14
- ☐ Vortex: any remaining calcium should precipitate and the beryllium should be in solution
- ☐ Centrifuge the “AMS” tube
- ☐ Label a 50ml centrifuge tube “SAMPLE Be Dirty”
- ☐ Decant the solution from the “SAMPLE AMS” tube into the “SAMPLE Be Dirty” tube
- ☐ Add 2 drops of bromothymol blue and 12 ml of 6M (50%) HCl to the “SAMPLE Be Dirty” tube
- ☐ Adjust the pH back to 8 with drops of NH_4OH
- ☐ Vortex and Be should precipitate
- ☐ Centrifuge at 3600 RPM for 5 minutes
- ☐ Decant the supernatant into the “SAMPLE Supernatant” bottle
- ☐ Rinse the precipitate with 5ml of ammoniated water
- ☐ Vortex
- ☐ Centrifuge at 3600 RPM for 5 minutes
- ☐ Decant the supernatant into the “SAMPLE Supernatant” bottle
- ☐ Rinse the precipitate with 5ml of ammoniated water
- ☐ Vortex
- ☐ Centrifuge at 3600 RPM for 5 minutes
- ☐ Decant the supernatant into the “SAMPLE Supernatant” bottle

- ☐ Add 4ml of 0.4M clean oxalic acid to the “SAMPLE Be Dirty” tube
- ☐ Vortex for 30 seconds to ensure that the Be gel dissolves fully. Wait at least 2 hours after this step before starting column chemistry to ensure that all Be is dissolved

Condition Columns:

- ☐ Pre-wet the empty column with a small amount of ethanol or isopropanol
- ☐ Use a transfer pipette to load the cation exchange resin into the empty column up to the 1ml mark
- ☐ Add 10ml of 6N HCl and let the column drain
- ☐ Add 10ml of 6N HCl and let the column drain
- ☐ Add 6ml of deionized water and let the column drain
- ☐ Add 1ml of clean 0.4M oxalic acid and let the column drain

Column Chemistry:

- ☐ Label a small bottle “SAMPLE Oxalic”
- ☐ Label a 15ml centrifuge tube “SAMPLE Be”
- ☐ Line up the open “SAMPLE Oxalic” bottle with the cation column drip-point
- ☐ Use a transfer pipette to transfer the sample from the “SAMPLE Be Dirty” 50ml tube into to column: the sample should be sitting in oxalic acid from the previous step
- ☐ Let the sample drain
- ☐ Add 2ml of 0.4M clean oxalic acid and let the column drain
- ☐ Add 10ml of 0.4M clean oxalic acid and let the column drain
- ☐ Add 10ml of deionized water and let the column drain
- ☐ Replace the oxalic bottle with the “SAMPLE Be” 15ml tube
- ☐ Add 2ml of 4N HNO_3 and let the column drain to elute the beryllium
- ☐ Repeat 4 more times

Precipitate the Be:

- ☐ Add 1 drop of 10% Na_2-EDTA solution to the “SAMPLE Be” 15ml tube

- ☐ Adjust the pH to 9 with NH_4OH to precipitate the beryllium. Use pH paper to check the pH this time, NOT bromothymol blue
- ☐ Vortex
- ☐ Centrifuge at 3600 RPM for 5 minutes
- ☐ Decant the supernatant into the "SAMPLE Supernatant" bottle
- ☐ Rinse with 5ml of ammoniated water
- ☐ Centrifuge at 3600 RPM for 5 minutes
- ☐ Decant the supernatant into the "SAMPLE Supernatant" bottle
- ☐ Rinse with 5ml of ammoniated water
- ☐ Centrifuge at 3600 RPM for 5 minutes
- ☐ Decant the supernatant into the "SAMPLE Supernatant" bottle

Dry-down:

- ☐ In your lab notebook make a map of a heating block (with wells for quartz vials): Samples will not be labeled on the vials, so ensure that you can identify each one based on your map
- ☐ Add 4 drops of 8N HNO_3 to the Be gel in the "SAMPLE Be" tube
- ☐ Add a clean quartz vial into the heating block
- ☐ Use a 1ml pipette to transfer the HNO_3 into the quartz vial
- ☐ Add 4 more drops of 8N HNO_3 to the "SAMPLE Be" tube
- ☐ Use the 1ml pipette to transfer the HNO_3 into the quartz vial
- ☐ Once all your samples are done, place the heating block on the hotplate for several hours on low heat (<100ºC to ensure that samples do not boil and splatter)

Oxidize the Be:

- ☐ Once the quartz vial in the heating block is completely dry take it off the heat and allow it to cool
- ☐ Clean a pair of tongs with acetone

- ☐ Pick up the quartz vial with the tongs and place it into the nichrome wire sample holder, which is suspended over the ring on the laboratory stand. The setup should be in a fume hood
- ☐ Light a torch and lightly heat the sample from a distance until a brown/red gas evolves and all visible moisture dissipates
- ☐ Align the torch and sample such that the quartz vial is in the flame
- ☐ Allow the sample to oxidize for 2 minutes in the flame: this converts the sample to BeO
- ☐ Place the sample back into the heating block in its original well to cool

Prepare samples for cathodes: **Be careful when working with beryllium oxide! Always wear an N-95 mask. Follow all laboratory disposal protocols. Label all waste.**

- ☐ Place a Kimwipe on top of the loading block. Use tweezers to push your quartz vial down into the well of the loading block so the vial stands upright on its own
- ☐ Add 2 scoops of niobium powder to the quartz vial using the #1 Meyhoefer curette. The Nb:BeO rato by mass should be ~3:1
- ☐ Use silicon carbide sandpaper and a couple drops of alcohol to sand down the surfaces of a loading rod. This ensures that the rod's surface is clean
- ☐ Dry the loading rod with a Kimwipe
- ☐ Add 2 drops of acetone to the quartz vial
- ☐ Hold the vial with your fingers. Grind the sample with the loading rod.
- ☐ When finished, place the vial back in the loading block. Leave the loading rod in the vial
- ☐ Once you've repeated this process for all your samples, and the acetone has dried, you can continue with the loading process

Load the samples into cathodes:

- ☐ Place a Kimwipe on top of the loading block.
- ☐ Take a fresh stainless steel cathode from the box. Record the cathode number on your datasheet and ensure that you write down which sample will be associated with the cathode number
- ☐ Press the cathode down into the loading block well

- ☐ Take the sample's quartz vial and run it under the anti-static head
- ☐ Pour ground sample from vial into the cathode. Tapping the vial with the loading rod helps to free the powder
- ☐ Use the loading rod to scrape all the powder into the cathode well
- ☐ Tamp down the powder in the cathode well with the rod: place the rod in the well, and hit it with the hammer
- ☐ Take the cathode out of the loading block. Turn it upside-down, and hit it on a piece of weigh paper. If you compacted the sample correctly, it should stay inside the cathode
- ☐ Put the cathode into its vial face-down, and cap
- ☐ Dispose of quartz vial, Kimwipes, and gloves in a labeled beryllium waste bag. DO NOT dispose with normal trash
- ☐ Place loading rod into a 'used loading rods' container or dispose with beryllium waste

APPENDIX 5: DATA FROM SOREQ CAVE

Here I present the chemistry data for the eighteen samples from Soreq Cave speleothems. Detailed step-by-step chemistry methods are described in appendix 4.

^{9}Be measurements were made using ICP-OES. I measured beryllium from the intensity of the 234.861nm line. The calibration curve for each ICP run consisted of a 0 ppb standard and a 19.91 ppb standard. Several runs of a 2.42 ppb standard and a blank were interspersed between the speleothem samples during each run. The average beryllium concentration in the ^{9}Be aliquots was 2.91 ppb (for Soreq Cave) and 3.33 ppb (for Buffalo Cave). The Soreq Cave aliquot beryllium concentrations ranged from 1.23-5.84ppb, while the Buffalo Cave aliquot concentrations ranged from 0.99-11.45ppb. Since these concentrations are low, drift during the ICP-OES runs was of major concern. For the runs where I observed drift in the standards and/or blanks, I applied appropriate drift corrections.

Table A5.1: Laboratory chemistry data for Soreq Cave speleothem samples.

Column 'B' is the total mass of calcite dissolved. Column 'C' is the mass of calcite equivalent that went through solvent extractions. The difference between columns 'B' and 'C' represents an aliquot kept for elemental analysis (see appendix 6). Column 'D' is the mass of solution aliquoted from the solution in column 'C' for ^{9}Be measurement.

Sample	Calcite Mass (g)	Calcite Mass Equivalent to Solvent Extraction (g)	Mass of Total Solution After Solvent Extraction (g)	Mass of ^{9}Be Aliquot (g)	^{9}Be Concentration in Aliquot (ppb)	ngBe/g calcite	Be Abs Uncertainty	Age (ka)
2-3-1' (outer)	4.963	4.421	21.481	4.78274	5.84	28.375	1.419	1.7
2-20-E	2.796	2.772	27.518	4.89313	2.67	26.502	1.325	5.3
2-20-R	4.9	4.418	21.737	5.05858	4.39	21.598	1.080	9.6
2-N-H	3.902	3.827	39.099	4.69744	2.06	21.045	1.052	15.0
12-Z-C	6.623	6.062	30.500	4.98395	1.726	8.684	0.434	20.0
1-4-J	3.276	3.239	32.770	4.62231	1.23	12.443	0.622	32.0
1-4-L	6.078	5.500	28.273	4.8528	2.241	11.520	0.576	35.0
SQ9-25-D2	1.538	1.521	11.412	4.19291	3.5	26.254	1.313	54.4
11-27-A	5.278	5.170	26.243	4.96618	2.77	14.061	0.703	67.6
11-27-H+G	2.834	2.780	30.889	4.88481	1.78	19.780	0.989	80.3
11-27-S+T	3.874	3.799	25.030	4.5285	2.13	14.034	0.702	89.4
11-27-U+V	4.175	4.092	20.686	4.69903	4.62	23.355	1.168	103.7
SQ-15 Light	5.013	4.550	22.567	4.95224	1.614	8.004	0.400	127.5
2-22-A	4.619	4.541	23.562	5.1111	4.95	25.686	1.284	134.5
2-22-D1	4.794	4.706	22.464	4.90186	2.69	12.841	0.642	155.0
2-22-E	3.856	3.787	26.443	4.97481	3.1	21.646	1.082	160.0
2-22-G	4.761	4.679	29.154	4.90121	3.07	19.130	0.956	165.0
2-22-I2	4.36	4.266	29.382	4.93519	2.06	14.189	0.709	168.0

Table A5.2: Additional laboratory chemistry data for Soreq Cave speleothem samples. Column 'D' represents the aliquot of the total solution that went through preparation for AMS ^{10}Be measurement. This solution was aliquoted from the solution in column 'C.' The equivalent mass of calcite that went through solvent extractions is in column 'C' of the previous table (table A5.1). Column 'K' has been corrected for ^{10}Be decay using the speleothem age from the previous table. The Be concentration in the carrier for all samples was 1046 ppm.

Sample	Mass of Carrier (g)	Mass of Total Solution After Solvent Extraction (g)	Mass of Solution to AMS	^{10}Be/^{9}Be from AMS	Unc. (%)	Atoms ^{10}Be/g calcite	±	^{10}Be/^{9}Be native	±	Decay Corrected Native ^{10}Be/^{9}Be	±
2-3-1' (outer)	0.283	21.48148	16.68227	3.21579E-12	1.220	19303534.7	235422.5	1.01808E-08	5.23966E-10	1.01895E-08	5.24411E-10
2-20-E	0.28162	27.51792	22.60094	1.96788E-12	1.381	17042338.4	235276.5	9.62357E-09	4.99183E-10	9.64909E-09	5.00507E-10
2-20-R	0.28047	21.73705	16.66303	2.59655E-12	1.089	15528079.7	169134.1	1.07592E-08	5.50574E-10	1.08109E-08	5.53222E-10
2-N-H	0.28137	39.09905	34.37987	2.74606E-12	1.001	16143026.6	161610.7	1.14793E-08	5.85358E-10	1.15657E-08	5.89762E-10
12-Z-C	0.28214	30.49966	25.49454	7.72871E-13	1.751	3075577.5	53847.5	5.2999E-09	2.80771E-10	5.35314E-09	2.83592E-10
1-4-J	0.27997	32.77016	28.12506	1.11092E-12	1.481	7842041.5	116124.9	9.43159E-09	4.91826E-10	9.58363E-09	4.99755E-10
1-4-L	0.28101	28.27337	23.3203	1.68715E-12	1.337	7514786.5	100466.0	9.76229E-09	5.05262E-10	9.93455E-09	5.14177E-10

SQ9-25-D2	0.28253	11.41196	7.17939	6.87151E-13	1.723	14231604.8	245208.3	8.11204E-09	4.29009E-10	8.33561E-09	4.40832E-10
11-27-A	0.28177	26.24258	21.25438	1.65291E-12	1.928	7821815.3	150767.7	8.32479E-09	4.46098E-10	8.61083E-09	4.61426E-10
11-27-H+G	0.28497	30.88887	25.98807	7.93622E-13	1.785	6795117.8	121284.7	5.14093E-09	2.72933E-10	5.35142E-09	2.84109E-10
11-27-S+T	0.28033	25.02954	20.48301	8.70594E-13	1.633	5515738.8	90068.2	5.88174E-09	3.09373E-10	6.15048E-09	3.23509E-10
11-27-U+V	0.28184	20.6864	15.97311	1.57996E-12	1.314	9905099.8	130168.8	6.34689E-09	3.28123E-10	6.68448E-09	3.45575E-10
SQ-15 Light	0.28185	22.56694	17.598	3.16534E-13	2.453	1805176.8	44272.4	3.37505E-09	1.8796E-10	3.5971E-09	2.00326E-10
2-22-A	0.2815	23.5616	18.43829	2.04729E-12	1.634	11389536.6	186108.8	6.63577E-09	3.49057E-10	7.09713E-09	3.73326E-10
2-22-D1	0.28094	22.46425	17.54387	1.18799E-12	1.371	6379507.9	87454.2	7.43464E-09	3.8545E-10	8.03342E-09	4.16494E-10
2-22-E	0.27944	26.44287	21.4537	1.60183E-12	1.451	10233650.4	148475.3	7.07524E-09	3.68354E-10	7.6642E-09	3.99017E-10
2-22-G	0.2748	29.15417	24.13623	1.85423E-12	1.141	9238354.7	105381.9	7.22715E-09	3.70642E-10	7.84835E-09	4.025E-10
2-22-I2	0.28211	29.38211	24.43333	1.55037E-12	1.191	8681789.1	103407.4	9.15674E-09	4.70648E-10	9.95871E-09	5.11869E-10

Table A5.3: AMS blanks for Soreq Cave samples. BLK-CHM is the only blank that went through the full solvent extraction and column chemistry. SQ BLK 1 and SQ BLK 2 only went through the ^{10}Be column chemistry

AMS Blank Name	**^{10}Be/^{9}Be from AMS**	**Abs Unc.**
SQ BLK 1	3.21211E-16	3.07566E-16
SQ BLK 2	5.47693E-16	4.30144E-16
BLK-CHM	6.63676E-16	3.31881E-16

APPENDIX 6: TRACE METAL CONCENTRATIONS FROM SOREQ CAVE SPELEOTHEMS

After dissolving and filtering the speleothems, I took an aliquot for measurement of trace element concentrations before proceeding with the solvent extraction. Here I present the trace-element data for the Soreq Cave speleothems. The elements I measured were Al (167.018 nm), P (177.433 nm), Ni (221.65 nm), Fe (238.207 nm), Mn (260.575 nm), Ti (334.941 nm), Sr (407.771 nm), and Ba (493.408 nm).

All samples and standards were prepared in 5% HNO_3 for analysis. I measured the concentrations during two ICP-OES runs. For both runs I used 277.56 ppb and 0 ppb multi-element standards for the calibration curve. During the first run, most of the phosphorus concentrations were higher than the maximum standard. Titanium concentrations were mostly too low for measurement, and most strontium concentrations were too high, thus saturating the detector. Therefore I aliquoted and diluted the samples and re-measured to improve the data for the high-concentration elements. Between the two ICP-OES runs, I chose the appropriate data to use on a case-by-case basis.

The relationships between all measured elements are plotted below. I also include trace element concentrations plotted temporally.

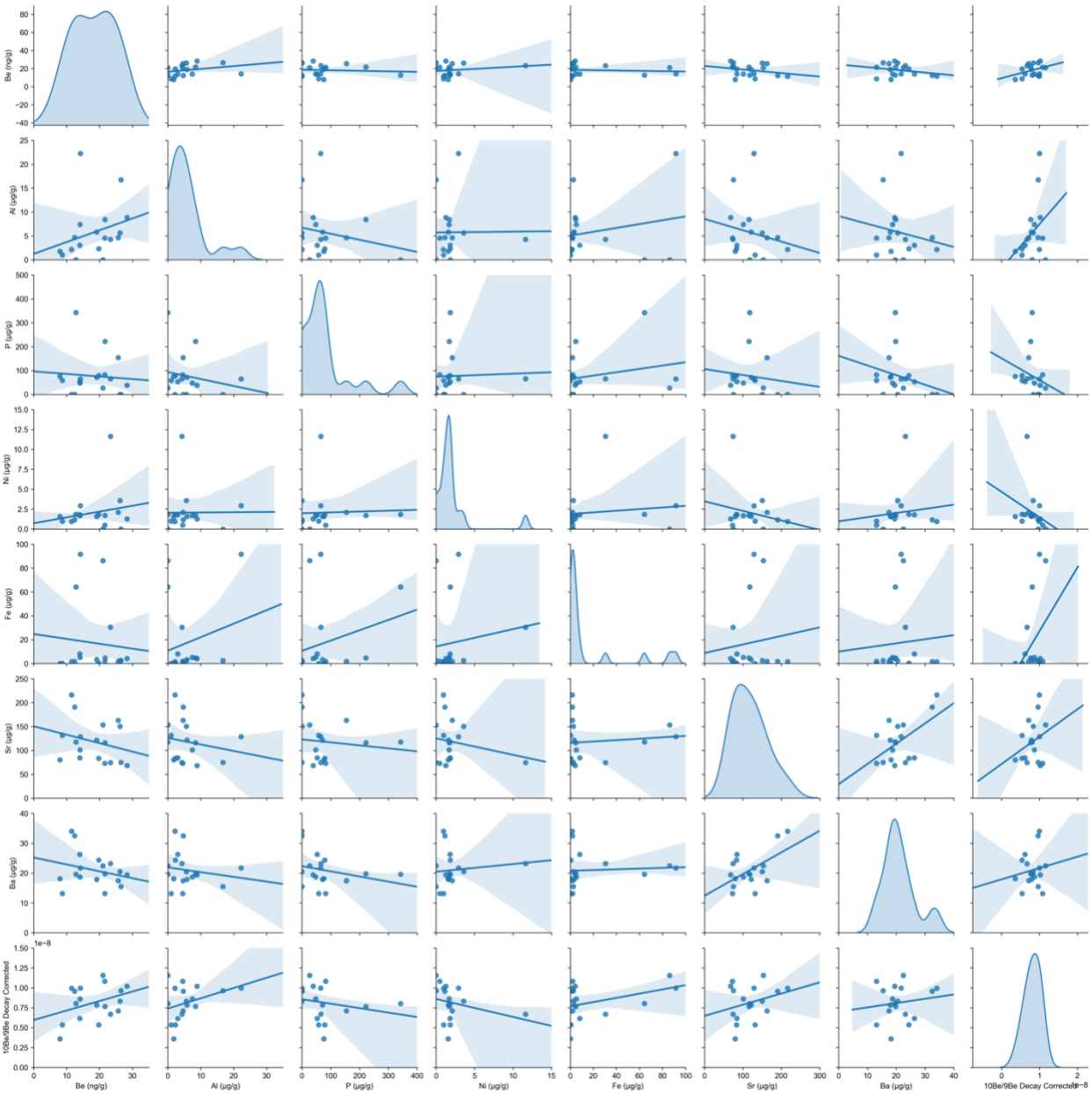

Figure A6.1: Trace elements from Soreq Cave

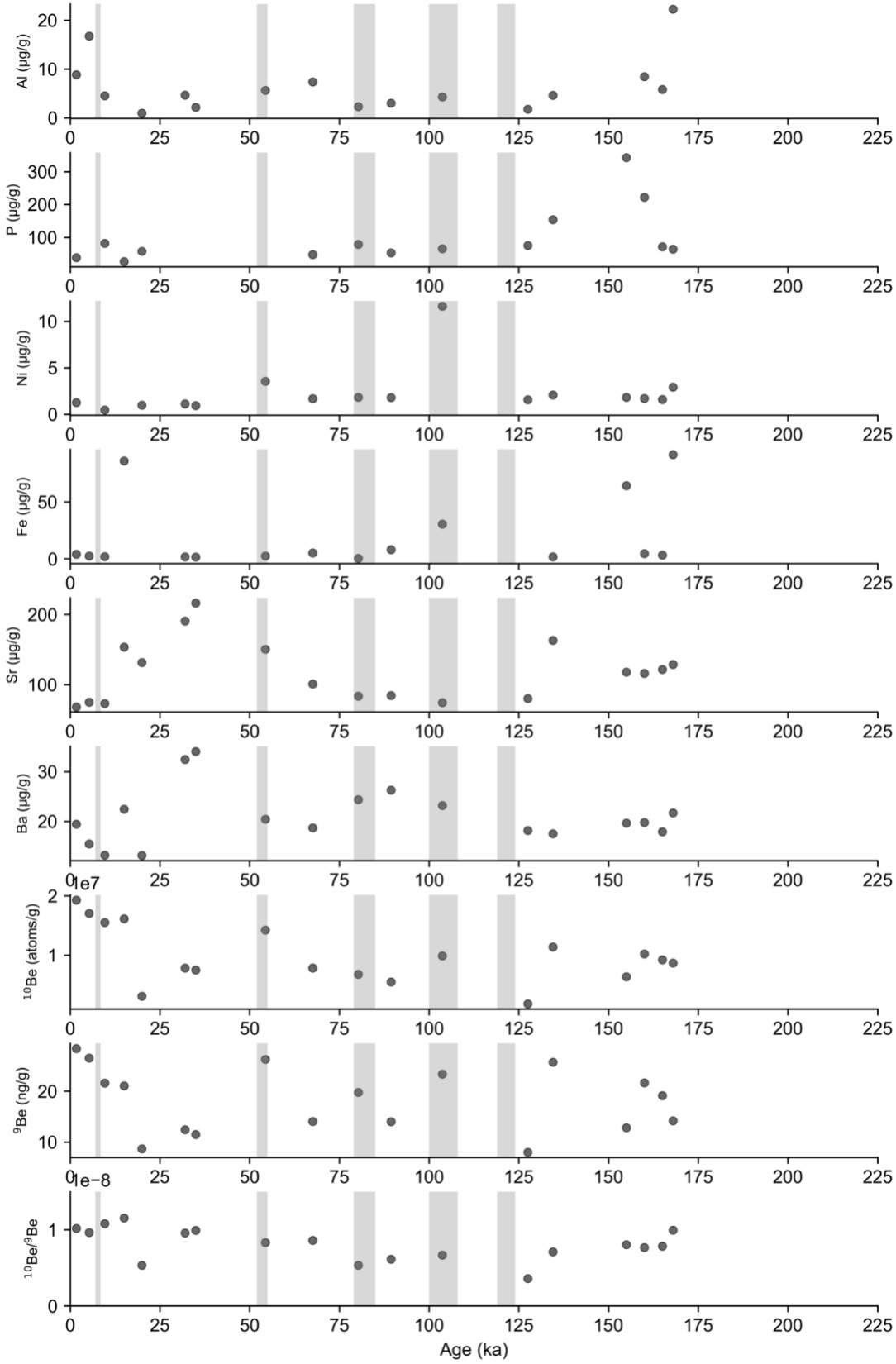

Figure A6.2: Soreq Cave trace elements plotted temporally

APPENDIX 7: DERIVATION OF EQUATION TO ESTIMATE W_P FROM FELDSPAR/QUARTZ RATIOS AT SOREQ CAVE

Here I derive the equation I use in section 6c of chapter 2 to estimate the modern feldspar chemical weathering rate at Soreq Cave based on feldspar and quartz concentrations in the dust and soil, as well as a modern dust flux.

The equation that comes from Riebe et al. (2004) is in this form:

$$W_{p,Fs} = F^{dust}\left([Fs]_{dust} - [Fs]_{soil}\frac{[Qz]_{dust}}{[Qz]_{soil}}\right)$$

(Eq. A7.1)

(Eq. 3 from Riebe et al. 2004)

$W_{p,Fs}$ = W_p of feldspar

F^{dust} = Dust flux (g/m^2/yr)

$[Fs]_{dust}$ = Concentration of feldspar in the dust (g/g)

$[Fs]_{soil}$ = Concentration of feldspar in the soil (g/g)

$[Qz]_{dust}$ = Concentration of quartz in the dust (g/g)

$[Qz]_{soil}$ = Concentration of quartz in the soil (g/g)

The CDF-based weathering equation from Riebe et al. (2004) shows that we can estimate the W_p of feldspar if we know the relative concentrations of quartz and feldspar in the dust and soil, as well as the overall dust flux. In order to demonstrate how this equation works, we can model this system as a set of steady-state fluxes into and out of the soil, much like how I model beryllium fluxes earlier in chapter 2. Here I will demonstrate how this approach arrives at the same equation.

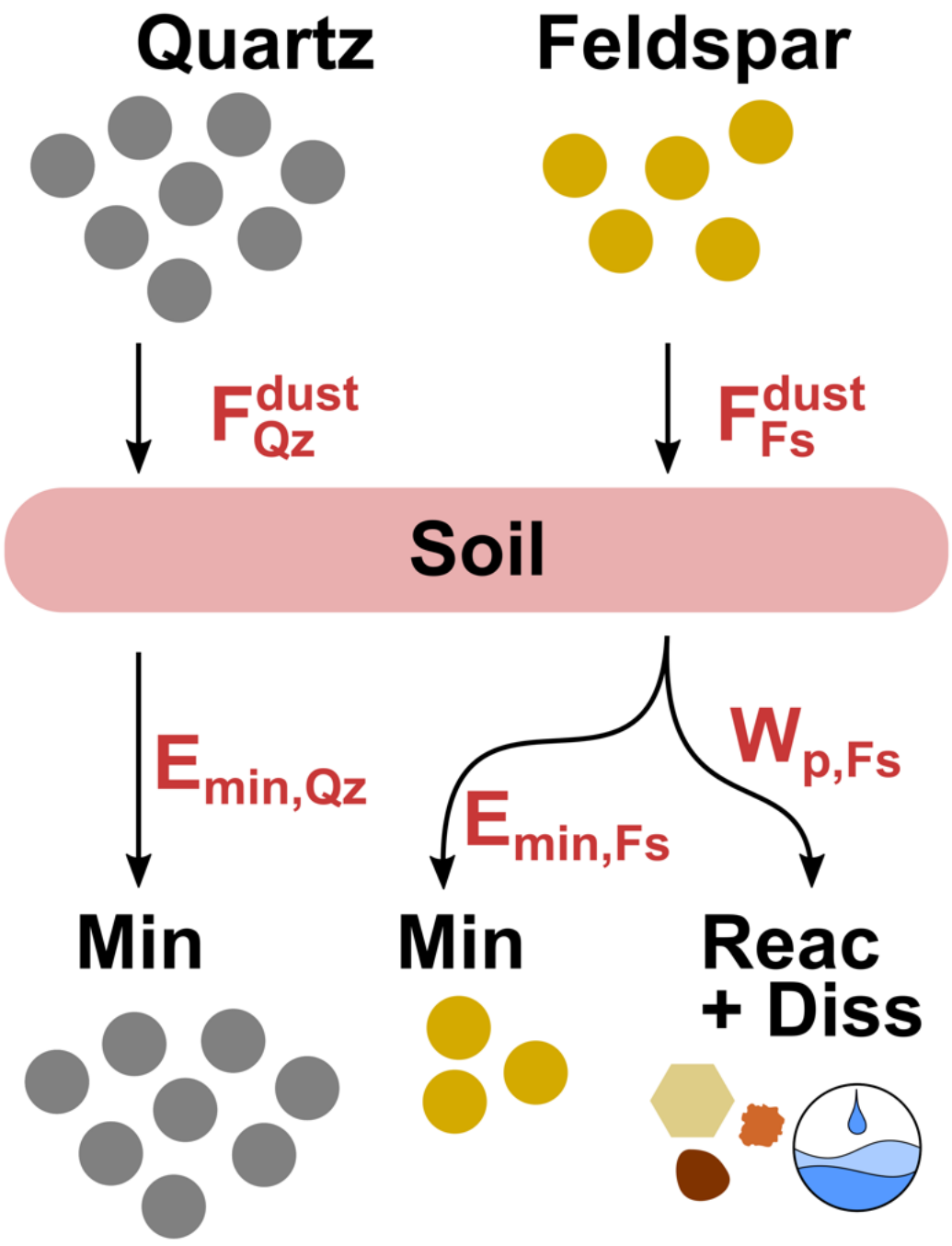

Figure A7.1: Weathering fluxes with quartz and feldspar

Quartz and feldspar enter the soil exclusively in the settling dust. Therefore, the flux of feldspar or quartz into the soil is equal to the total dust flux multiplied by the mineralogical concentration in the dust:

$$F_{Fs}^{dust} = F^{dust}[Fs]_{dust}$$
$$F_{Qz}^{dust} = F^{dust}[Qz]_{dust}$$

(Eq. A7.2 & A7.3)

Since we are assuming that the chemical weathering of quartz is negligible, quartz leaves exclusively via erosion. Therefore, the dust flux of quartz equals the erosion rate of quartz in the 'min'pool:

$$F^{dust}[Qz]_{dust} = E_{min,Qz}$$

(Eq. A7.4)

On the other hand, feldspar leaves the soil via erosion of the 'min' phase as well as chemical weathering. Therefore, the dust flux of feldspar equals the erosion rate of feldspar in the 'min' pool, plus chemical weathering $W_{p,Fs}$:

$$F^{dust}[Fs]_{dust} = E_{min,Fs} + W_{p,Fs}$$

(Eq. A7.5)

Recalling definitions earlier in this chapter, the soil can be broken into the 'min' and 'reac' pools, and each pool can be further broken down into their contribution from a particular phase:

$$1 = \gamma_{min} + \gamma_{reac}$$

(Eq. A7.6)

$$\gamma_{min} = \gamma_{min,Fs} + \gamma_{min,Qz}$$

$\gamma_{min,Fs}$ = Fraction of total soil or sediment (including reactive phases) that is feldspar

$\gamma_{min,Qz}$ = Fraction of total soil or sediment (including reactive phases) that is quartz

Therefore, the mineral-specific erosion terms can be broken down in the following manner:

$E_{min,Fs} = E\,\gamma_{min,Fs}$

$E_{min,Qz} = E\,\gamma_{min,Qz}$

(Eq. A7.7 & A7.8)

in which $\gamma_{min,Fs} = [Fs]_{soil}$ and $\gamma_{min,Qz} = [Qz]_{soil}$

Likewise, the concentration of quartz and feldspar the dust (which is the parent material) can be expressed in terms of fractions, as described earlier in the chapter:

$1 = \alpha_{Fs} + \alpha_{Qz} + \alpha_{Carbonate} + \alpha_x$ ...

(Eq. A7.9)

α_{Fs} = Fraction of the parent material that is feldspar

α_{Qz} = Fraction of the parent material that is quartz

$\alpha_{Carbonate}$ = Fraction of the parent material that is carbonate

α_x ... = Fraction of the parent material that is other phases

Therefore, the concentrations of feldspar and quartz in the dust can be re-written as:

$\alpha_{Fs} = [Fs]_{dust}$ and $\alpha_{Qz} = [Qz]_{dust}$

(Eq. A7.10)

With these definitions, we can re-write the earlier steady-state expressions as:

$F^{dust}\,\alpha_{Qz} = E\,\gamma_{min,Qz}$

And

$F^{dust}\,\alpha_{Fs} = E\,\gamma_{min,Fs} + W_{p,Fs}$

(Eq. A7.11 & A7.12)

By solving each equation for total erosion rate (E), the two expressions can be set equal to one another, and the equation simplifies to the original CDF-based equation from Riebe et al. (2004):

$$W_{p,Fs} = F^{dust}\left(\alpha_{Fs} - \gamma_{min,Fs}\frac{\alpha_{Qz}}{\gamma_{min,Qz}}\right)$$

(Eq. A7.13)

Appendix references

von Blanckenburg, F., Bouchez, J., and Wittmann, H., 2012, Earth surface erosion and weathering from the 10Be (meteoric)/9Be ratio: Earth and Planetary Science Letters, v. 351–352, p. 295–305, doi:10.1016/j.epsl.2012.07.022.

Caley, T. et al., 2018, A two-million-year-long hydroclimatic context for hominin evolution in southeastern Africa: Nature, v. 560, p. 76–79, doi:10.1038/s41586-018-0309-6.

Carmichael, S.K., Doctor, D.H., Wilson, C.G., Feierstein, J., and McAleer, R.J., 2017, New insight into the origin of manganese oxide ore deposits in the Appalachian Valley and Ridge of northeastern Tennessee and northern Virginia, USA: Geological Society of America Bulletin, p. B31682.1, doi:10.1130/B31682.1.

February, E.C., and Higgins, S.I., 2010, The distribution of tree and grass roots in savannas in relation to soil nitrogen and water: South African Journal of Botany, v. 76, p. 517–523, doi:10.1016/j.sajb.2010.04.001.

Herries, A.I.R., Reed, K.E., Kuykendall, K.L., and Latham, A.G., 2006, Speleology and magnetobiostratigraphic chronology of the Buffalo Cave fossil site, Makapansgat, South Africa: Quaternary Research, v. 66, p. 233–245, doi:10.1016/j.yqres.2006.03.006.

Hopley, P.J. et al., 2018, Orbital precession modulates interannual rainfall variability, as recorded in an Early Pleistocene speleothem: Geology, v. 46, p. 731–734, doi:10.1130/G45019.1.

Hopley, P.J., Weedon, G.P., Marshall, J.D., Herries, A.I.R., Latham, A.G., and Kuykendall, K.L., 2007, High- and low-latitude orbital forcing of early hominin habitats in South Africa: Earth and Planetary Science Letters, v. 256, p. 419–432, doi:10.1016/j.epsl.2007.01.031.

Moore, A.K., Granger, D.E., and Conyers, G., 2021, Beryllium cycling through deciduous trees and implications for meteoric 10Be systematics: Chemical Geology, v. 571, p. 120174, doi:10.1016/j.chemgeo.2021.120174.

Odom, W.E., 2020, DATING THE CENOZOIC INCISION HISTORY OF THE TENNESSEE AND SHENANDOAH RIVERS WITH COSMOGENIC NUCLIDES AND 40AR/39AR IN MANGANESE OXIDES: Purdue University.

Riebe, C.S., Kirchner, J.W., and Finkel, R.C., 2004, Erosional and climatic effects on long-term chemical weathering rates in granitic landscapes spanning diverse climate regimes: Earth and Planetary Science Letters, v. 224, p. 547–562, doi:10.1016/j.epsl.2004.05.019.